UNIVERSIDAD DE CHILE
FACULTAD DE CIENCIAS FÍSICAS Y MATEMÁTICAS
DEPARTAMENTO DE ASTRONOMÍA

ATMOSPHERES OF OBJECTS ON THE UPPER PLANETARY-MASS LIMIT AS A CLUE TO DISTINGUISH BETWEEN FORMATION MECHANISMS

TESIS PARA OPTAR AL GRADO DE
MAGÍSTER EN CIENCIAS, MENCIÓN ASTRONOMÍA

PAULINA PALMA BIFANI

PROFESOR GUÍA:
PATRICIO ROJO RÜBKE

PROFESOR CO-GUÍA:
GAËL CHAUVIN

MIEMBROS DE LA COMISIÓN:
MICKAËL BONNEFOY
PAULINA LIRA TEILLERY
LAURA PÉREZ MUÑOZ

SANTIAGO DE CHILE
2022

ATMÓSFERAS DE OBJETOS EN EL LÍMITE SUPERIOR DE MASA PLANETARIA PARA DISTINGUIR MECANISMOS DE FORMACIÓN

La difusa línea divisoria entre las enanas cafés y los exoplanetas gigantes ha despertado la curiosidad de astrónomos porque representan dos poblaciones de objetos astrofísicos, fundamentales para la comprensión de la física planetaria y estelar, ya que comparten propiedades físicas. Se han barajado definiciones basadas en su masa o capacidad de fusionar deuterio o en las vías de formación para diferenciarlos. Últimamente se ha propuesto distinguir sus procesos de formación a partir de su composición química. Las capas superiores de las estrellas y las enanas cafés contienen la composición de la nube molecular de la que se formaron. Sin embargo, los planetas se forman en un disco protoplanetario que rodea a la estrella, lo que hace que diferentes moléculas se condensen a diferentes radios, afectando directamente su composición. La relación entre el carbono y el oxígeno ($^C/_O$) se ha propuesto, por ejemplo, como trazador del lugar de formación.

Este proyecto pretende comprender el panorama de las teorías de formación junto a las actuales herramientas de modelamiento atmosférico. Proponemos explorar una muestra de objetos subestelares aislados y acompañantes para rastrear y comparar sus orígenes en función de su arquitectura. Comenzamos extrayendo los espectros de 24 objetos observados con SINFONI en la banda K, ideal para estimar el $^C/_O$ debido a las bandas del CO. Estos espectros son uno de nuestros principales resultados. Luego los comparamos con las predicciones de modelos atmosféricos de planetas gigantes y enanas cafés para derivar sus propiedades (masa, temperatura, luminosidad, radio) y composición en relación con sus procesos de formación.

De los 24 objetivos seleccionados, AB Pic b nos llamó la atención por su espectro de alta calidad y los extensos conjuntos de datos ya reportados en la literatura. Dado el especial interés que suscita el súper Júpiter AB Pic b, nos centramos luego en revisar sus características atmosféricas y orbitales para estudiar su origen y naturaleza. Obtuvimos la distribución de energía espectral de AB Pic b, desde el óptico hasta el infrarrojo térmico, basándonos en una extensa búsqueda y la nueva observación de SINFONI en banda K. Modelamos el espectro con el código ForMoSA, implementando dos grillas atmosféricas (Exo-REM y BT-Settl13). Obtuvimos una metalicidad ligeramente superestelar y un $^C/_O$ estelar, no reportados previamente. De los resultados, proponemos que las inestabilidades gravitacionales o la acreción de partículas a gran separación (más allá de la línea de nieve del CO) formaron AB Pic b. Sin embargo, no se pueden descartar otros escenarios. Actualmente, estamos a punto de publicar esta investigación, que es nuestro segundo producto principal.

ATMOSPHERES OF OBJECTS ON THE UPPER PLANETARY-MASS LIMIT AS A CLUE TO DISTINGUISH BETWEEN FORMATION MECHANISMS

The diffuse dividing line between brown dwarfs and giant exoplanets has aroused the curiosity of astronomers because they represent two populations of astrophysical objects, fundamental for the understanding of planetary and stellar physics, and share common physical properties. To differentiate them definitions have been considered based on their mass or ability to fuse deuterium or their formation pathways. Lately, it has been proposed that we may distinguish their formation depending on their atmospheric composition. The upper layers of stars and brown dwarfs reflect the molecular cloud composition from which they formed. However, when planets form, a protoplanetary disk surrounds the star, which causes different molecules to condensate at different radii, directly affecting the planet's atmospheric composition. The carbon to oxygen ratio ($^C/_O$) on atmospheres has been, for instance, proposed as a tracer for the location of formation.

This project aims to understand the latter planetary formation theories together with the current atmospheric modeling tools. We aim to explore a sample of substellar isolated objects and companions to understand whether a connection can be made between their present-day configuration and their atmospheric composition. We started by extracting the spectra of 24 targets observed with SINFONI on the K band, ideally suited for estimating the $^C/_O$ due to the observable CO bandheads. These spectra are one of our main results. We then compared them with the predictions of atmospheric models of giant planets and brown dwarfs to derive their bulk properties (mass, temperature, luminosity, radius) and their composition.

From the 24 selected targets, AB Pic b caught our attention because of its high-quality spectrum and the extensive datasets already reported in the literature. Given the particular interest in the massive super-Jupiter AB Pic b, we focused on revisiting its atmospheric and orbital characteristics to study its origin and nature. We obtained the most complete spectral energy distribution of AB Pic b, from optical, near- to thermal-infrared, based on an extensive archival search combined with a new reduced K band SINFONI observation. We modeled the spectrum with the forward-modeling code ForMoSA, following a multi-modeling approach for two atmospheric grids (Exo-REM and BT-Settl13). We derived a slightly super-stellar metallicity and a stellar $^C/_O$ not previously reported. Analyzing the results, we propose that either gravitational instabilities or core/pebble accretion at large separation (beyond the CO snowline) likely formed AB Pic b. However, other scenarios cannot be ruled out. Currently, we are close to publishing this research, which is the second main product of this M.Sc. project.

Gracias Pá y Má, por mostrarme las estrellas
y creer que puedo alcanzarlas.

Agradecimientos

Este proyecto de tesis no es solo el fruto de intenso trabajo sino también del apoyo de muchas personas, a quienes me gustaría agradecer. Primero que nada, gracias a las/os profesoras/es que me han enseñado desde pequeña hasta este momento. Especialmente gracias a Pato, Gaël, Mickaël, Laura y Myriam, muy talentosas/os astrónomas/os y maravillosas personas. Me han mostrado el estado del arte y la belleza de los exoplanetas y la formación planetaria y me han motivado a seguir adelante por el camino de la ciencia. Me siento muy afortunada por haberlos conocido e indiscutiblemente son un gran ejemplo para mi.

A continuación destacar el apoyo de mi pareja y mejor amigo me parece importante. Gracias Peri por todo el apañe, eres muy importante para mi. Juntos nos hemos esforzado muchísimo estos años y hemos disfrutado profundamente la universidad, estudiar, cocinar, conversar, viajar y muchas otras cosas. Aparte, pronto partiremos al extranjero a seguir persiguiendo nuestro sueño compartido de hacer ciencia y conocer el mundo, lo cual me emociona mucho.

Luego está el resto de mi familia. Gracias Pá por mostrarme la astronomía y por motivar mi interés científico. Gracias Má, Pame, Marce y Rolo por estar siempre presentes y preocupadas por el bienestar de los demás. Gracias también a mis abuelas (Lela, Moni y Tere), abuelos (Lolo, Valerio, Opa Nego y Don Jose), tías, tíos, primes, familiares, Ernesto, Pao y amigues de la familia. Me han acompañado desde pequeña a mirar el cielo; me han enseñado la importancia y la belleza de la perseverancia y del esfuerzo; han escuchado mis ideas y motivado a aprender con el corazón; y sobre todo, me han mostrado, a partir de sus propios caminos como ejemplo, a perseguir lo que deseo. En definitiva, gracias por el apoyo y amor incondicional.

Por último, aprender ha sido un proceso lleno de experiencias, con altos, con muy altos y con bajos también, por lo que me gustaría agradecer a todes les amiges que me han acompañado estando presentes estos años. Con quienes estudiamos, conversamos, nos divertimos, nos estresamos y seguimos aprendiendo. Gracias Sofi R, Maike, Anto y Pame Pi, amigas de toda la vida. Gracias Sofi P, Ben y Juanfe y a quienes he conocido por ahi. Gracias Jipix, Javi R, Tita, Vale, Sofi, Seba, Maca, Cata, Ojeda, Ivan, Javi V y Mandi, mis grandes amigues de plan común. Infinitas gracias Raza, Luquitas, Mau, Robert, Byron, Peri y Nico, y especialmente gracias Pola, amigues de la especialidad. Les admiro infinito y atesoro los incontables momentos compartidos que me han ayudado a ir encontrando mi camino y a mi misma. Por último, gracias Vines (senpai) y Simon, por ayudarme con los códigos e ideas difíciles. Esperando no haber dejado a nadie fuera de esta larga lista, les agradezco amigues, con todo el corazón, por apañar a todas las locuras y espero muchas más, ojalá en Francia.

Contents

List of Tables

List of Figures

Chapter 1

Introduction

The diversity of exoplanets detected over the past thirty years has wholly disrupted our knowledge of planetary physics, chemistry, formation, architecture and evolution. The field has benefited from the instruments, observational techniques, and data analysis methods that are continuously evolving, revolutionizing the knowledge in this research area. However, many questions remain to be solved. For example, how do the formation environment and the evolution history of planetary-mass companions impact their atmosphere and spectral signatures? The purpose of this chapter is to introduce the main ideas and approaches explored during this thesis project to understand better the most accepted formation theories and their connections to planetary atmospheric sciences. We will start by presenting the current state of the art, then the scientific question we aim to answer, and finally, the essential background topics regarding formation theories and their connection to atmospheric modeling techniques.

1.1   Today's Exoplanets Picture

Transit, direct imaging, and cross-dispersed spectroscopy, among other techniques, have successfully allowed astronomers to explore the diversity of exoplanets. Since the first characterization of HD 209458 b, a hot Jupiter (Charbonneau, 2002), exoplanets revealed a broad diversity of masses, radius, orbital properties, and physical processes at play. Today more than 4300 exoplanets with different characteristics have been discovered, which teaches us different properties of these objects. It can be observed from Figure 1.1 that some parts of the diagram show clustering of objects while others are nearly empty. This clustering is tied to the detection techniques used, which all have their proper bias (especially at large separations) and are also related to different formation mechanisms at short separations.

The upper right corner of Figure 1.1 shows the population of massive exoplanets at wide orbits, among them, emblematic systems such as HR 8799 (Marois et al., 2010), β Pictoris (Lagrange et al., 2019), HD 95086 (Rameau et al., 2013), HIP 65426 (Chauvin et al., 2017) or PDS 70 (Keppler et al., 2018) which offer a rich opportunity to investigate the architectures of young solar-system analogs, but also the atmospheres of young super-Jupiters sometimes still

accreting material (Haffert et al., 2019). Given these interesting characteristics, this project focuses on the study of these massive, direct imaged, young and wide orbit exoplanets.
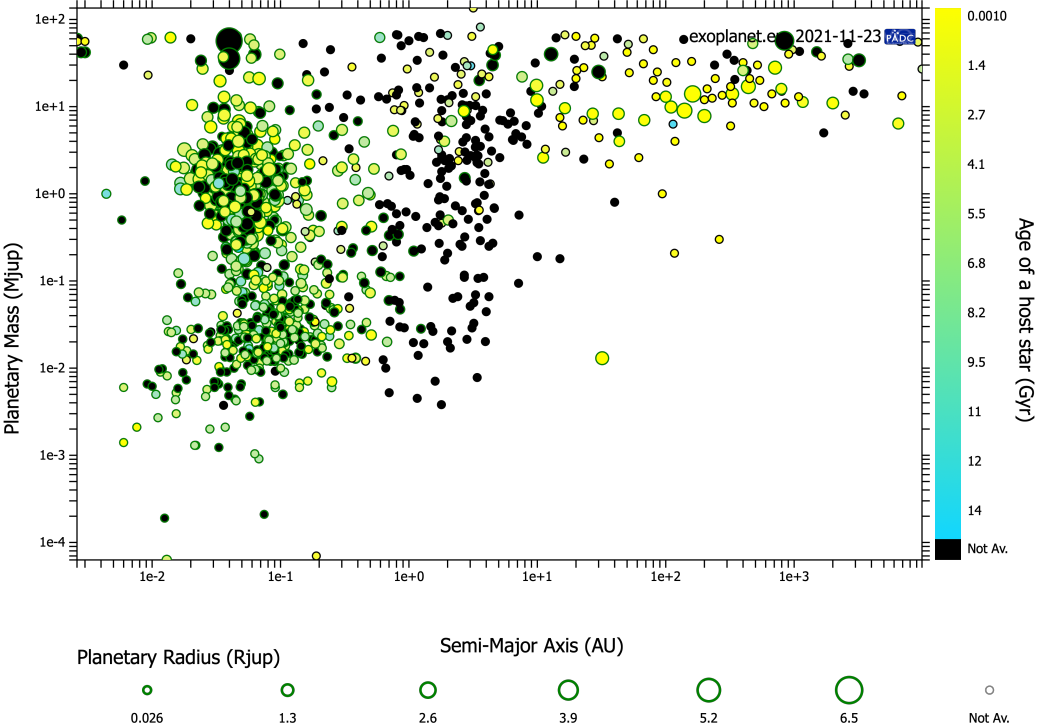
Figure 1.1: Exoplanet diversity as a function of semi-major axis, planetary mass, planetary radius, and system age. (Figure created from `http://exoplanet.eu/`)

1.2   Brown Dwarfs as Giant Planets Analogs

During the past decades, remarkable improvements in telescopes, instruments, and detectors, have been made, which allowed us to directly resolve the atmospheric chemical composition of cold, substellar objects of spectral types covering late-M, L, T to Y-dwarfs. These substellar objects have been found as planetary-mass companions to stars as mentioned above but isolated in space too. The observations have taught astronomers that there seems to be no known barrier that differentiates brown dwarfs (hereafter BD) from massive exoplanets. Definitions based on their physical properties, like mass or ability to fuse deuterium or their formation, have been considered. The current picture proposes to consider BD as failed stars, formed isolated or in multiple hierarchical systems in space and unable to burn hydrogen. Even if formed as a stellar binary companion, their atomic abundance ratio and bulk composition should not differ from the original molecular cloud values. The population of BD companions orbiting stars overlaps in separation and mass with giant gaseous planets formed at various locations in a protoplanetary disk but with potentially different chemical compositions, impacting the metallicity and chemical abundances on the atmospheres, as proposed by Mordasini et al. (2016).

Exploring the origin and the nature of BD and exoplanets can therefore be approached by peering into the atmospheres of young, substellar ($\leq 75 M_{jup}$) companions and isolated objects to track potential differences of composition related to different formation mechanisms. In this line, the exploration based on medium resolution spectra of young, BD, and exoplanets with atmospheric modeling techniques enables to retrieve key parameters like effective temperature, surface gravity, metallicity, and chemical abundances, including the carbon to oxygen ratio. This ratio was measured for the Solar System planets decades ago and has been used to discuss the Solar System formation. More recently, it has been proposed as a tracer of formation mechanisms for exoplanets, as described by Öberg et al. (2011).

1.3   Formation Theories

We present an overview of the most classical and currently accepted planet formation theories, which are Core Accretion (hereafter CA), Gravitational Instabilities (hereafter GI) and Gravoturbulent fragmentation of a molecular cloud (hereafter GtF), and newer adaptations known as Pebble Accretion (hereafter PA) and the Tidal Downsizing Hypothesis (hereafter TDH). Next, we present BD and star formation theories to explain the formation of substellar objects directly in molecular clouds. The variety of formation theories is a consequence of the observed variation in the exoplanet population. Depending on the circumstances of the environment, planets could form in several ways. We emphasize the formation processes of massive planets because we can resolve their spectrum, and we expect to model their physical and chemical properties. Finally, a review of different migration mechanisms can be found in the last parts of this section since dynamical interaction between minor bodies happens, which can dramatically modify the system's architecture. These interactions can happen while the system is still forming or after the protoplanetary disk is dispersed.

1.3.1   Companions Formed by a Bottom-Up Process

We will start by analyzing the bottom-up formation theories. The main idea is that on protoplanetary disks, grains can grow from μm interstellar medium (ISM) size into mm and even cm particles, called pebbles. Laboratory experiments, numerical simulations, and observations have proven that grains grow into pebble size particles, as mentioned in Testi et al. (2014). Nevertheless, growing those particles to form m and km size bodies, called planetesimals, is difficult because the fragmentation and drift barriers affect the pebbles, making them leave the disk or be accreted onto the host star. Currently, two leading theories are based on a bottom-up description: CA and PA.

Core Accretion (CA)

The steps to growing particles from m to km size bodies on the Core Accretion scenario, as described by Chabrier et al. (2014), are the following. First, the pebbles must stick and grow
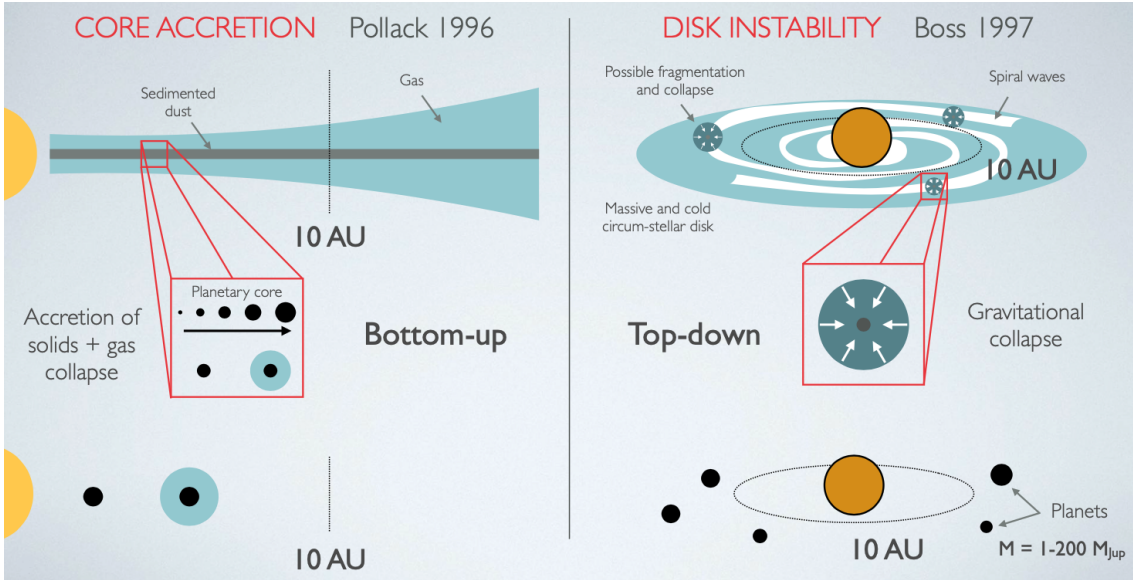
Figure 1.2: On the left panel, a schematic view of a classical CA model. On the left panel, a schematic view of the GI formation theory. We observe the formation processes at an early stage on the top while on the bottom at its final stage. (Priv. Comm. Simon Petrus).

to form a solid core. This process is highly inefficient due to the mentioned barriers, but if the objects are close to the host star due to the high amount of pebbles, the timescales are short enough to favor the formation of a solid planetary core. When the accretion of planetesimals allow the formation a solid core, the growing core attracts a gas envelope, but since the accretion of planetesimals not only increases the core mass but also releases energy to the envelope, the mass of the envelope grows up faster than the mass of the core, and it starts to dominate the gravitational potential. As a result, the envelope collapses and the core starts accreting more mass, transforming into a giant planet (Chabrier et al., 2014). A schematic general view of this process can be observed on the left panel of Figure 1.2. A detailed view of the accretion of planetesimals and the overcome of the meter barrier can be found in Figure 1.3. The meter barrier is a physical limit that implies that forming planetesimals is unlikely. The streaming instability is a possible solution to overcome the meter barrier where local dust over-density regions allows pebbles to grow into planetesimals and then into a planetary core. The accretion of material onto the star and the formation of giant exoplanets and rocky exoplanets are possible outcomes.

In order for the CA process to happen, the initial core must have a mass over a critical value which has been discussed in many works, but the radiative solution sets the critical mass at $\sim 10\ M_\oplus$ (Pollack et al., 1996). Apart the core must be located at a few AU from the host star. As enormous timescales are associated with the core growth and further envelope accretion, some other issues make this theory wobble. For instance, core formation beyond 5 AU is impossible within typical lifetimes of protoplanetary disks. From the discussion given on these ideas by Chabrier et al. (2014), it is clear that to explain the formation of a giant planet beyond 5 AU, another mechanism must be involved. The reported values are valid for the original CA theory but different studies may derive other results, as Rafikov (2006). This could be migration or a mechanism that reduces the formation timescales considerably but is not fast enough to slow down the gas envelope accretion (for example, PA).
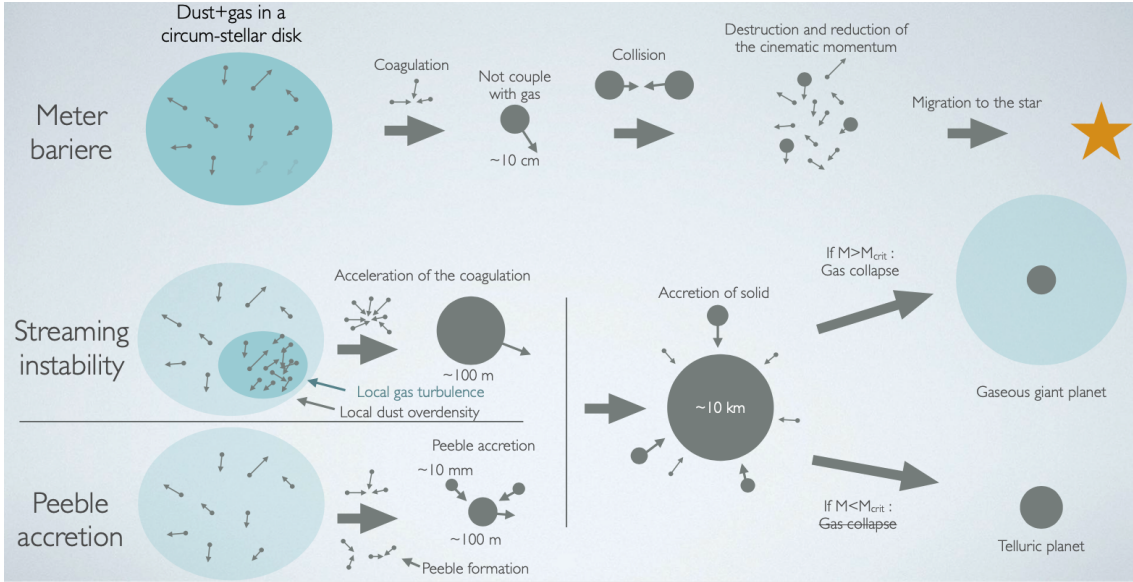
Figure 1.3: A detailed schematic view of the CA theory emphasizes the barriers that need to be overcome and how they are overcome. On the bottom left, the PA scenario is explained. (Priv. Comm. Simon Petrus).

Pebble Accretion (PA)

By revisiting the theory of planetesimal accretion onto the core, it has been observed that soon after a dominant core emerges in the same way as described for CA, the surrounding planetesimals tend to be destructed, and then those fragments are accreted more efficiently by the surviving core. They are accreted due to the gas drag, making pebbles surrounding the nascent core spiral toward it. In this scenario, giant planets can form at larger separations of around 50 AU or even 200 AU for massive disks. In any case, explaining the presence of giant planets at separations beyond 100 AU is still difficult for most cases. The main idea here is that instead of favoring the sticking between particles to grow on a bottom-up grown scenario where the bouncing barrier will be much more challenging to overcome, there will be a small number of massive cores that can statistically easily overcome this barrier (Chabrier et al., 2014). Due to small pebbles that can feed a growing core, the formation of planets at larger locations is favored. These ideas can be observed on the bottom left section of Figure 1.3.

The dynamics of pebbles close to growing cores are fundamentally different from planetesimals. Planetesimals can only be accreted from within a gravitational radius, but pebbles are pulled out of their Keplerian orbits resulting in dissipation of their kinetic energy by friction and subsequent accretion by the core. Growth rates in this regime are ~ 1000 times faster at ~ 5 AU and ~ 10000 times at ~ 50 AU (Chabrier et al., 2014). Pebble accretion is not an efficient mechanism after the cores reach a mass of $\sim 15 M_\oplus$ as showed by Paardekooper and Johansen (2018). In that mass regime, the forming planet tends to open a gap in the pebble distribution, causing them to stop being accreted. Blain, D. et al. (2021) suggested that this would open space to start the gravitational collapse of gas to the core, which will lead to the formation of giant planets. In this scenario, cores of $10 M_\oplus$ can form anywhere in the

disk, but from observations, it is rare to see giant planets beyond 25 AU. The reason behind this radial observable limit is that compact disks are more common than extended ones, or efficient migration mechanisms may bring the planets rapidly closer inside. However, planets can be scattered by dynamical interactions, and they can be found at larger separations, as the companions studied in this work.

1.3.2 Companions Formed by a Top-Down Process

Gravitational Instabilities (GI)

Another way of understanding the formation of substellar objects is a top-down process where a gravitational collapse explains these bodies' emergence. This process is also known as a hot start because the formed body has high temperatures. This mechanism could explain the emergence of both BD and giant exoplanets. Its called Gravitational instabilities (GI), but it is also known as Disk Instabilities. The main idea is that on massive disks around protostars, a fragmentation process can take place, and those fragments of over-densities could then cool down and become the cores of gaseous giant exoplanets or BD. In order to create this type of object, the disk must be highly massive, radially extended, and have appropriate cooling conditions (Boss, 1997). To determine if the system is stable or if a fragmentation process can occur, the Toomre's stability criterion proposed by Toomre (1964). This criterion is analogous to the Jeans stability criterion for stationary gas in molecular clouds but extended for disks, taking into account the rotation of the particles around the central star. The criterion (Q_{gas}) is described by Equation 1.1 where c_s is the sound speed, κ is the epicyclic frequency, G is Newton's constant and Σ the surface density. If $Q_{gas} > 1$, the disk will be stable, but if $Q_{gas} \leq 1$ gravitational instabilities occur.

$$Q_{gas} = \frac{c_s \kappa}{\pi G \Sigma} \tag{1.1}$$

As mentioned on Nayakshin (2017), the core must be created at large distances, and the initial process would be very similar to the stars' cores forming on molecular clouds. The formation of bigger bodies in the higher density fragments by the gravitational collapse of a young and massive protoplanetary disk will be triggering the formation of more massive objects. A schematic view can be found on Figure 1.2 on the right panel. After a dense clump forms, a process of runaway mass loss will take place until the core starts to dominate the mass of the planet. Since in this case, we have a hot start, initially the composition of the core is similar to the ISM, but the core migrates inward while it is being formed, and finally, we can expect that the outer layers of the envelope have a mix of materials made at low and at very high temperatures Paardekooper and Johansen (2018).

From observations, massive and extended disks appear to be rare at early stages. However, for this project, we are mainly interested in companions at large orbital distances ($> 50\,au$); therefore, we need to understand how these objects are formed. Apart, even if these massive disks exist and there is fragmentation going on, it is not clear that those fragments can cool down fast enough to survive. These arguments disfavoring the GI formation process
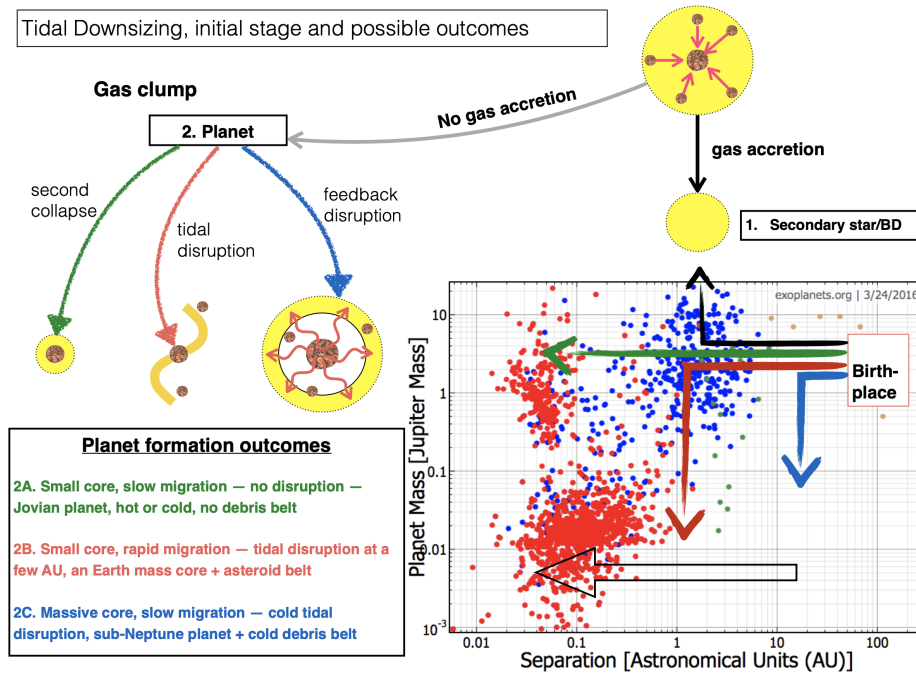
Figure 1.4: (Nayakshin (2017), figure 25) A schematic illustration of how TDH may explain the observed populations of low mass exoplanets, gaseous planets and low mass stars.

are valid for low-mass protostars. In any case, the exoplanet population is diverse, and we may observe exoplanets that can be explained through this mechanism, particularly true for planets observed at considerable distances from their host star where CA is unlikely due to the disk's lifetimes or to explain a third BD or exoplanet companion to a host binary. Apart, these mechanisms appear to be able to jump over many difficulties that appear on the CA model, as described by Paardekooper and Johansen (2018).

Tidal Downsizing Hypothesis (TDH)

In this same line, it has been proposed by Nayakshin (2010) that planets could be formed through a complex mechanism known as the tidal downsizing hypothesis. This theory is, in practice, an extension of the GI scenario but merges different ideas to explain the formation of BD, gaseous exoplanets at different locations, and rocky planets altogether, making it a very robust theory. First of all, a core is formed in regions of over-densities inside massive protoplanetary disks at large separations by the collapse of the material. This core can evolve in two different ways. A resume of the different involved mechanisms and outcomes can be observed in Figure 1.4 from Nayakshin (2017) and is explained below.

On one side, if no more gas is accreted, there are three possible outcomes. i/ A second collapse can make the surrounding gas to be accreted, and following this way, the formation of a hot or cold Jupiter-like planet is explained. ii/ If the core suffers from tidal disruption at a few astronomical units from the star, it can lower its initial mass, and the Earth-like planet's population and asteroids can be explained as outcomes of this disruption. iii/ If the migration is slow and the tidal disruption affects mainly the gaseous envelope, then the

7

population of sub-Neptune planets and debris belts are the outcomes. Conversely, if the core accretes more gas from the surroundings, a secondary star can be created, a massive one or a BD.

This theory is much newer than the other proposed ones, and therefore it still needs to be observationally tested and has been questioned by some works, for example, Forgan et al. (2017). In any case, this attempt to unify the theories is fascinating. However, some initial conditions may make this theory unlikely to explain the exoplanet population in general, as, for example, the requirement of a massive disk surrounding the star at early stages. In the coming years, it will be interesting to see how this theory is tested by comparing the location of formation of exoplanets and their physical and chemical properties to the predictions of this hypothesis.

1.3.3 Formation of Substellar Object in Molecular Clouds

Gravoturbulent Fragmentation (GtF)
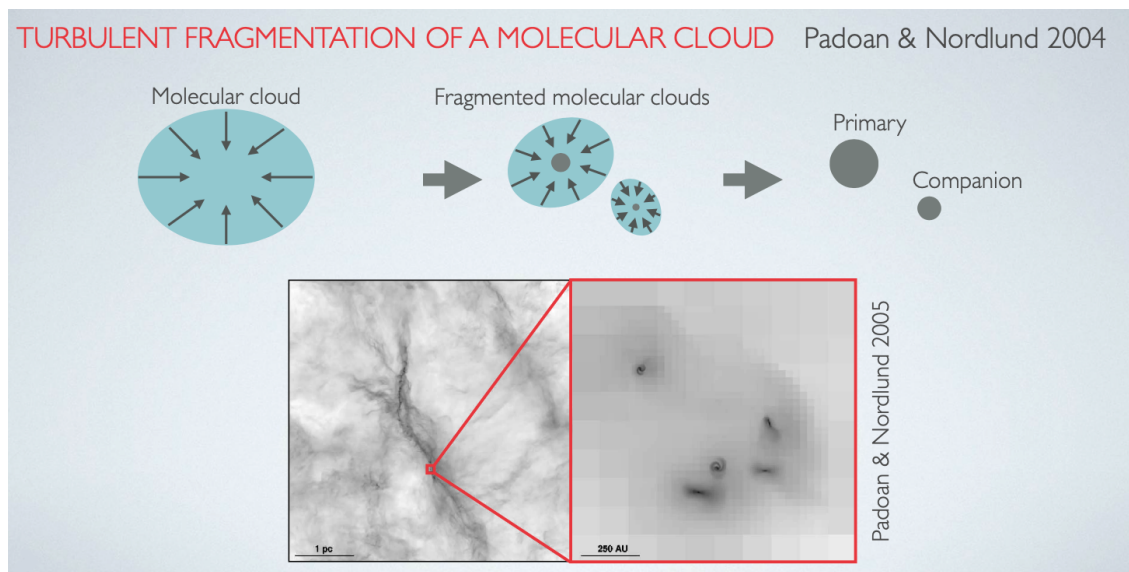
Figure 1.5: Variation in column density for a molecular cloud and a schematic view of the fragmentation of a molecular cloud leads to the formation of a star and a substellar companion. (Priv. Comm. Simon Petrus).

The third family of formation mechanisms that we will discuss is GtF. In molecular clouds, large-scale turbulence can be injected, which will cascade down to minor scales by shocks. In specific over-dense regions, gravity can overcome other sources that may support collapse, and cores may be created and isolate themselves from the surrounding material, which are less massive than $87\,M_{jup}$, the lower mass limit for star formation (Baraffe et al., 2015).

In Figure 1.5 we observe irregular variations in density in a molecular cloud and a schematic view of fragmentation of a molecular cloud which leads to the formation of a primary and a less massive companion. What is essential to understand from this scenario is that it is

inappropriate to use the average thermal Jeans mass as an estimate for characteristic mass for fragmentation in molecular clouds. Through turbulence, less massive cores could form isolated or emerging as companions, which we usually identify as brown dwarfs. This theory outcomes nicely match observations of stars and BD abundances, because the initial mass function (IMF) is already imprinted in the cloud conditions. One could think that due to turbulence, formed cores could fragment into many small objects, but other processes such as the presence of magnetic fields, can slow down the fragmentation process, and the outcomes appear to be consistent with observations (Luhman, 2012).

In summary, as mentioned in Luhman (2012), it seems relatively robust to affirm that young brown dwarfs and young stars: i/ exhibit similar radial velocity dispersion, ii/ have similar spatial distribution in young clusters, iii/ have mass distributions consistent with the same underlying IMF, iv/ have both wide binary companions v/ exhibit similar accretion and disk chemical signatures, vi/ have similar disk fractions, vii/ both exhibit outflows and viii/ have both been identified at the early pre-stellar/BD stage of core formation in isolated environments. It seems from all the above arguments that stars and BD formation seem to share many observational signatures, an argument favoring this mechanism of formation that points to a common origin to explain the populations of the two types of objects.

Stars

As a piece of complementary information for formation theories, a classical star formation process can be observed in Figure 1.6. Here a star is forming due to the gravitational collapse of dense regions within molecular clouds. Once the material collapse and pressure and temperature are high enough on the star's core, hydrogen atoms start to fuse to form helium releasing giant amounts of energy in the process. Since the stars formed directly from the molecular cloud by gravitational collapse, it's composition is expected to reflect the chemical composition of their initial environments.
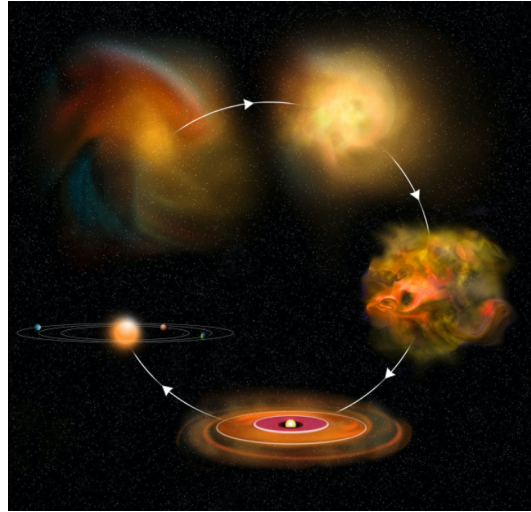
Figure 1.6: Classical star formation scheme.

Accretion-Ejection

Another proposed mechanism for BD formation is Accretion-Ejection, mentioned in Chabrier et al. (2014). In this case, we can think that $\sim 1~M_{jup}$ embryos form by accretion through efficient dynamical fragmentation of molecular clumps on clouds but then are ejected from

the surrounding gas reservoir. The simulation outcomes produce more stars and BD than the actual observed population rate, and this scenario does not explain the existence of BD in low-mass environments since dense molecular clouds are needed as an initial condition. Since observationally, BD's are created as efficiently in low mass environments as in denser ones, this formation process is probably viable in particular scenarios but not a fundamental star and BD formation mechanism, as described by Chabrier et al. (2014).

1.3.4 Migration Mechanisms

If there is no migration, for example, CA and PA based models predict that massive planets should exist at separations of around ($\sim\ 1-5\,\mathrm{au}$ for CA / $\sim\ 1-25\,\mathrm{au}$ for PA) to accrete enough gas, and Earth-like planets would form at closer distances. However, this was proven wrong by the existence of hot Jupiters and large orbit giant planets. We may ask ourselves if hot Jupiters form by other mechanisms that we did not explore, or do they migrate inwards? Migration happening in protoplanetary disks and later are pretty different in physics and expected outcomes which is why it has been classified by different types: usually from 0 to III. We will visit migration mechanisms theories in this subsection, and the expected outcomes since the formation analysis of exoplanets cannot be considered complete if we do not consider the possible interactions of forming planets with the protoplanetary disk and with other planets of the systems. The following subsections will be based on the results and the discussions about migration presented on Paardekooper and Johansen (2018) and on Marleau et al. (2019).

Type 0 Migration

Type 0 migration mainly describes the motion of dust and pebbles through the disk. We expect that dust drifts inwards over time due to higher pressure in inner regions. When the particles are approximately 1 cm in size, the inward drift becomes very efficient, and particles end up falling onto the central star. This drift occurs vertically too, also called settling, leading to bigger mid-plane particles than those located at higher scale heights. In summary, this will produce that the particles order themselves by size. Other processes, for example, turbulence, could difficult for them to settle and remix them (see Figure 1.7). These mechanisms, however, happen at short time scales and early stages. In this sense, it does not affect the already formed planets but drives the chemical composition differentiation with radial distance. The chemical differentiation is critical for later analysis of the formation location because it might be imprinted on the atmospheres of the forming planets.

Type I Migration

Type I migration, as described by Paardekooper and Johansen (2018) is an efficient mechanism for low mass planets ($M\ <\ 1\ M_{Neptune}$). Particles that fly close by to a planet feel their gravitational force and therefore suffer a change in their trajectory, and as a consequence, the planet feels a reacting force when it scatters the passing by particles that will push it to
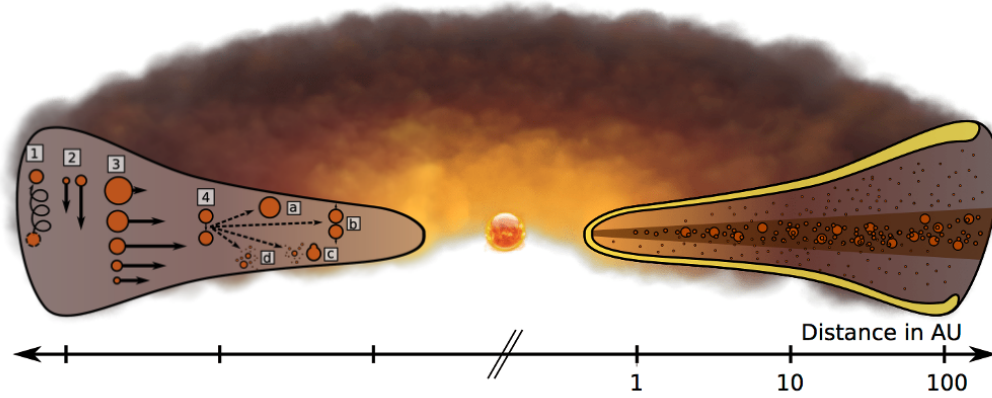
Figure 1.7: (Testi et al. (2014), figure 1) Schematic view on migration and growth of particles inside a protoplanetary disk

migrate. Since this study is focused on giant gaseous planets, we will not deepen the analysis of this migration mechanism. However, for general knowledge, the left panel of Figure 1.9 shows a simulation of a low mass planet undergoing type I migration (Armitage).

Other works have proposed that this type of migration could be responsible for the migration of forming bodies in the GI scenario. The formation time scales, in this case, are much shorter than the gap opening time scales, and planets could migrate in this fast Type I regime as a result of interaction with the gas and dust in the disk. Therefore, planets formed by GI could end up at close separations from the host star, less than $20\,au$. This migration mechanism is a possible explanation for the population of hot Jupiter's as described by Nayakshin (2017) and Jupiter analogs. In Figure 1.8 we observe the separation as function of time for these forming cores in the GI formation scenario when following type I migration.
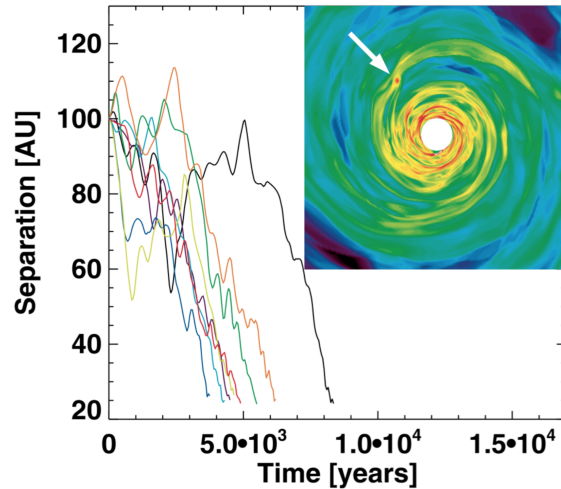
Figure 1.8: Separation vs time due to type I migration for GI cores. (Figure from Nayakshin (2017))

Type II Migration

Type II is the migration mechanism that happens after a massive planet opens a gap in the gas and dust distribution of the protoplanetary disk. In the right panel of Figure 1.9 a
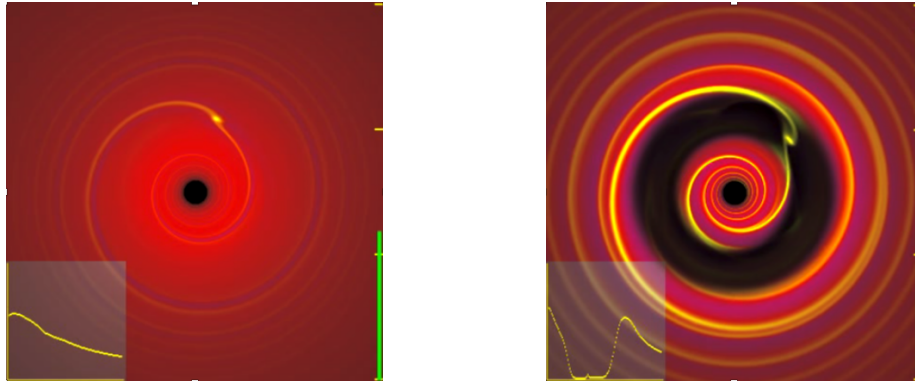
Figure 1.9: A simulation where on the left side the planet is migrating on type I regime while on the right the planet has a higher mass and is migrating on a type II regime. The images show cuts from a simulation done by Armitage. On the lower left corners of each panel, a radial profile of the disk is observable. On the type II migration regime, a clear gap appears on the disk.

simulation showing a massive planet that opened a gap is shown. When the gap appears, the interaction between the planet and the surrounding disk changes. If the gap is wide enough, the interaction between planet and disk stops. In this scenario, if the planet migrates a small amount inwards, the disk's inner edge will push the planet through a wave torque back to its original location, and the opposite situation occurs on the outer edge.

If we study the global disk evolution as a function of time, we would observe that the host star is slowly accreting the entire disk. For this process, the planet behaves just like another particle since it is locked inside the gap. Therefore, the gap will be approaching the host star during its evolution. This process is called type II migration. To explain how the host star stops accreting material, no universal agreement has been reached yet.

Type III Migration or Planet-Planet Scattering

After the planets are formed, they can still interact since these systems are chaotic. Marleau et al. (2019) tested the likelihood that HIP 65426, a wide orbit exoplanet (semi-major axis ~ 100 AU), could have been formed by CA closer inside and have migrated later to its current location by interactions with other bodies. The outcomes of one of their simulations can be observed in Figure 1.10. The location of the planets drastically changes over time due to close encounters while the disk was still present. The violet planets enter a phase of Runaway Accretion followed by an interaction with another of the planets to later evolve in type II migration to its final position. The mass of the planet increases until just before the disk disperses, and the position has remained unchanged since then for this specific simulation.

In general, the work done by Marleau et al. (2019) summarize pretty well the diverse possibilities for interactions and outcomes in planetary systems. Simulations have proved that a planet formed by CA can end up through migration mechanisms at large orbits (around 100 AU). An interesting observation is that planets can be expelled from the system through these scattering events, thrown onto the central star, collide, and end up at wide orbits still
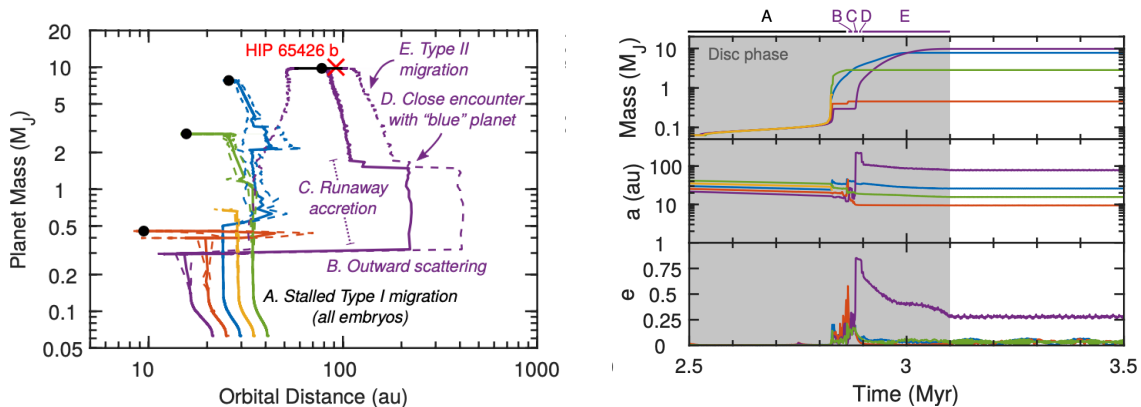
Figure 1.10: (Marleau et al. (2019), Figure 4) Planet-planet scattering interactions simulated to explain the current location of HIP 65426 b if formed closer in by CA. The orbital distance evolution for all planets in the system as a planetary mass function is shown on the left panel. On the right panel, we observe the mass, semi-major axis, and eccentricity as function of time. The shaded gray area represents the time where the disk was still present in the system. On the left, solid lines show the planets' semi-major axes, while dashed lines show the planets' pericentres and apocenters. Filled black circles represent final masses and semi-major axes for surviving planets. Black horizontal lines show the extent of the planets' final orbits from pericentre to apocentre. The red cross indicates the expected mass and projected orbital distance of HIP 65426 b.

gravitationally bound to the host star. In this last case we observe that highly eccentric orbits are highly probably outcomes, and therefore studying the orbital properties of exoplanets at large separations can tell us some insights into their formation and evolutionary history.

1.4 Direct Imaging Spectroscopy

Direct imaging studies have mainly focused on young, self-luminous giant gaseous planets, not strongly irradiated and orbiting their host star at relatively large separations, usually $\geq 100\,\mathrm{mas}$ in projected separation for current instruments. For example, $\beta\,\mathrm{Pic}\,\mathrm{b}$, one of the closes direct imaged exoplanets, has a projected separation of $\sim 400\,mas$ (Chauvin et al., 2012), equivalent to $\sim 9\,au$ given its distance of $63.4\,pc$ to the sun. The targets we are studying in this project meet these characteristics and they offer a very complementary view between transit and cross-dispersed studies of Hot Jupiters and the classical spectroscopic characterization of young isolated BDs (Jameson et al., 2008; Allers and Liu, 2013). For example, the transiting exoplanet discovered further away from its host is EPIC 248847494 b, with a semi major axis of $4.5\,au$ and located at $\sim 550\,pc$ (NASA Exoplanet Archive[1]). SPHERE at VLT (Beuzit et al., 2019), GPI at Gemini (Macintosh et al., 2006) or SCExAO/ CHARIS (Groff et al., 2015; Jovanovic et al., 2015), have yielded low-resolution ($R_\lambda \sim 50$) emission spectra and photometry of tens of exoplanets exhibiting broad unresolved molecular bands (H_2O, CH_4, VO, FeH, CO) in the near-infrared ($0.95 - 2.45\,\mu m$). Those observations can be compared to predictions of atmospheric models to infer first-order information on

---

[1]https://exoplanetarchive.ipac.caltech.edu

the physical properties, mainly effective temperature (T_{eff}) and luminosity ($log(L/L_\odot)$). However, they are lacking crucial information at higher resolution ($R_\lambda > 1000$) to resolve atomic and molecular lines and enable a detailed atmospheric exploration of fundamental parameters as metallicity ($[M/H]$), carbon to oxygen ratio ($^C/_O$) and isotopologues ratios (e.g. D/H, $^{13}CO/^{12}CO$, $^{13}N/^{14}N$), believed to be tracers of formation (Nowak et al., 2020; Molliere and Snellen, 2019).

An exploration of exoplanets' rotational and radial velocities, connected to their spin and three-dimensional orbital properties becomes feasible with higher resolutions, when specific absorptions lines start to be resolved (Snellen et al., 2014). Currently, a minimal number of exoplanets have been characterized at high spectral resolution ($R_\lambda > 10000$), among them, β Pictoris b (Snellen et al., 2014), GQ Lupi b (Schwarz et al., 2016b), HR 8799 planets (Wang et al., 2021), and HD 106906 b (Bryan et al., 2021). Young giant exoplanets at wide orbits offer unique laboratories to explore the spectral diversity together with formation and evolution scenarios through the understanding of their atmospheres, their properties, and the system dynamics and stability in connection with the stellar host properties. Therefore, these targets are ideally suited for being observed with the upcoming telescopes, such as the James Webb Space Telescope ($JWST^2$, first light 2022, GTO target), and the Extremely Large Telescope (ELT^3, first light 2027), allowing a broad wavelength range coverage, as observable in Figure 1.11.

Currently, a set of instruments observe at medium resolution and can partly isolate a rich set of molecular absorptions contained in a spectrum over broad wavelength ranges allowing reasonable estimations for many physical properties. For example, adaptive-optics-fed integral-field spectrographs (IFS) operating at a spectral resolving power of $R_\lambda = 2000 - 5000$ in the near-infrared, such as SINFONI at VLT, perform this type of observations allowing us to test further our current understanding of atmospheres. SINFONI slices the incoming light into 32 slitlets from which a datacube can be reconstructed. From the datacube, a spectrum can be extracted, which may look similar to the examples shown in Figure 1.11, but for narrower windows.
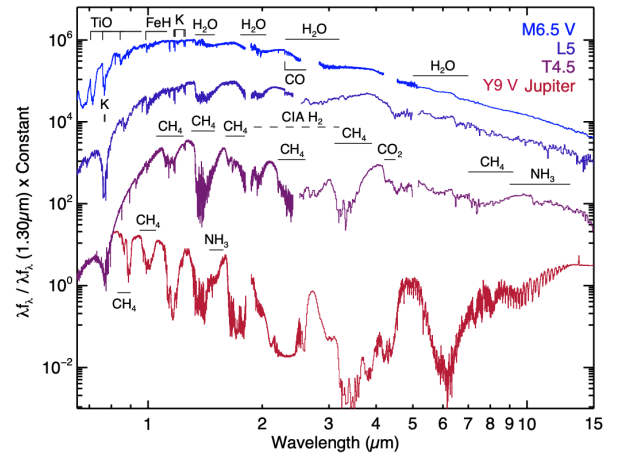
Figure 1.11: (Figure 1 from Fortney (2018)) Example on transition in spectral features from M-type star to Jupiter's spectrum.

As mentioned, to study how these types of objects have formed, the signatures imprinted on their atmospheres are crucial pieces of information. Since direct imaging is a technique that allows observing a wide spectral range, in medium to high resolution, by dispersing the incoming light, it is ideally suited for these research topics.

---

[2] https://jwst-docs.stsci.edu
[3] https://elt2020.web.ox.ac.uk

1.5   Modeling the Atmospheres of Giant Exoplanets

The determination of the physical properties of giant planets and BDs from pre-computed models of atmospheres has been approached by astronomers during the last years mainly by two different techniques: Retrieval Methods (Lavie et al., 2017) and Forward Modelling (Petrus et al., 2019, 2021). As described by Madhusudhan (2018), exoplanetary atmospheric retrieval methods refers to the exploration of atmospheric properties of an exoplanet given its observed spectrum using an approach driven by the data themselves with simple atmospheric models completely parametrized. The properties include usually chemical composition, pressure-temperature profiles, cloud and hazes, and energy circulation. From these properties, key insights into the physical and chemical processes at atmospheres of exoplanets can be derived, as well as their formation mechanisms.

For this project, we follow a more classical, forward modeling approach that, as inputs, receives a previously computed atmospheric model in the form of a parameterized grid which is compared to the observations through a Bayesian approach. In this case, the physics and the realistic description of the planetary and BD atmospheres completely drive the development of the models, and the main computation lies within the computation of the final spectral grid/predictions. The main advantages of this approach over free retrieval methods are the computation time and the inclusion of more physics, in particular concerning cloud modeling. Different atmospheric grids are currently available computed by different research groups, such as BT-SETTL13 (Allard et al., 2013), Exo-REM (Charnay et al., 2021), among others, following different physical principles to model the atmosphere of giant planets and BDs. This section will describe how atmospheric models are pre-computed and how forward modeling performs explorations.

1.5.1   Pre-Computed Atmospheric Models

The pre-computed atmospheric models are based on a radiative transfer description, including opacity sources of the molecules expected to be present on the atmospheres of these objects and their abundances, which can be observed in Figure 1.12. Attempts to include clouds, hazes, winds, disequilibrium chemistry, and thermal inversions, to mention some examples, have been carried out to reproduce the rich set of emission and absorption lines observables in their spectra, processes which are listed in the center of Figure 1.12. Clouds, hazes, and winds are directly included in the computation of the models and cannot be modified afterward since they are included in the radiative transfer description of atmospheres and are not a free parameter. Today the models are succeeding in fitting the atmospheric chemical signatures, but given the complexity of these systems, attempts to develop 3D models are being carried out nowadays, assuring to revolutionize the topic in the following years (Fortney et al., 2021). For this project, we implemented two atmospheric grids, BT-SETTL 13 and Exo-REM, for which the available parameter ranges are listed on the Table 1.1. ForMoSA interpolates and extrapolates the parameters to have broad coverage and the possibility of a refined grid. The dimension for each parameter and each grid is observable in Table 1.1, on the right side of the range. A description of the basis of the models is given below for both implemented grids.
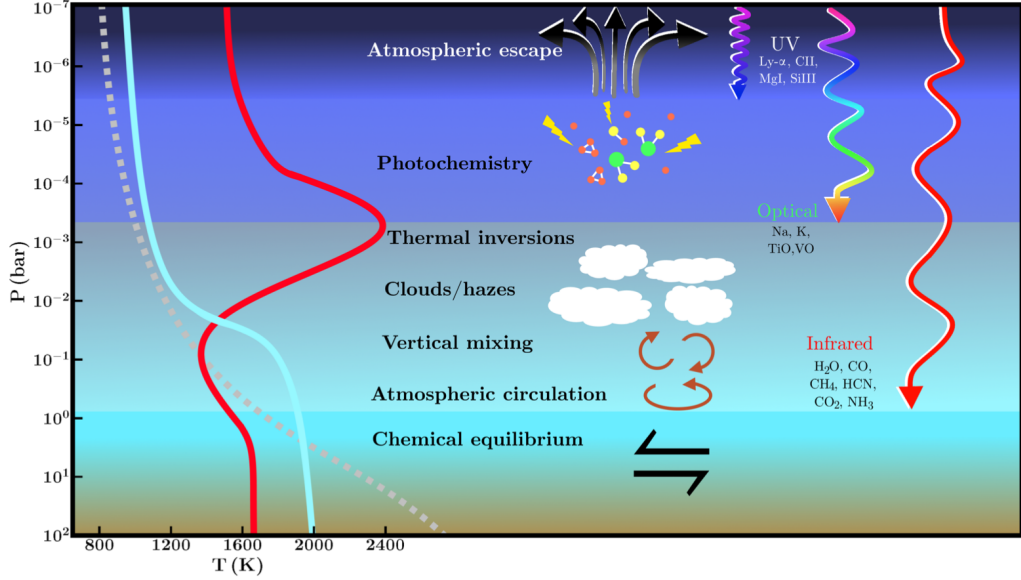
Figure 1.12: (Figure 1 from Madhusudhan (2019)) Active processes in exoplanetary atmospheres and how different parts of the electromagnetic spectrum probe them. These processes occur in different regions of the atmosphere and are labeled at the appropriate location. The penetration depths of UV, optical and infrared are shown on the right indicating the chemical species whose signatures can be detected. On the left three types of temperature profiles are shown: a highly-irradiated planet with a thermal inversion (red), an irradiated planet without a thermal inversion (cyan), and a poorly irradiated planet (grey, dashed).

Table 1.1: Parameter spaces explored by the implemented atmospheric models and other characteristics as their wavelength ranges and the inclusion of clouds into the models. The dimension of each parameter is listed together with the minimum and maximum value.

Parameter	BT-SETTL 13 width	dim	Exo-REM width	dim
wavelength (μm)	$0.3 - 15$	1087001	$0.667 - 251.6$	29922
T_{eff} (K)	$1400 - 2200$	9	$400 - 2000$	33
$log(g)$ (dex)	$3.5 - 5$	4	$3 - 5$	5
$[M/H]$	0.0	1	$-0.5 - 1$	4
C/O	$0.275 - 1.096$	3	$0.1 - 0.8.$	15
clouds	*included*		*included*	

BT-SETTL 2013

BT-SETTL13 is part of a family of atmospheric models by Allard et al. (2013) that include a 1D cloud model where the abundance and size distribution of 55 types of grain is determined by comparing the timescale of condensation, coalescence, gravitational settling, and mixing of solids that are supposed spherical. The details of each solid and chemical element are described in Rajpurohit et al. (2018). The opacities are calculated for each line, and the radiative transfer is carried on by PHOENIX (Hauschildt et al., 1997; Allard et al., 2001). The convection is handled following the mixing-length theory and works at hydro-static and

chemical equilibrium. The model also accounts for non-equilibrium chemistry between CO, CH_4, CO_2, N_2, and NH_3. This grid we used provides spectra fitting for three free parameters and a constant solar metallicity ($[M/H] = 0.0$) as listed in Table 1.1.

Exo-REM 2021

Exo-REM is an atmospheric radiative-convective equilibrium model presented in Charnay et al. (2021); Blain, D. et al. (2021) including a cloud description well suited for reproducing spectra where dust dominates, especially at the L-T transition. Like the BT-SETTL13 models, the atmosphere is cut into pressure levels where the flux is calculated iteratively using a constrained linear inversion method for radiative-convective equilibrium. The initial abundances of each element are first established using the values tabulated in Lodders (2010). The model includes the collision-induced absorption of $H_2 - H_2$ and $H_2 - He$, ro-vibrational bands from nine molecules (H_2O, CH_4, CO, CO_2, NH_3, PH_3, TiO, VO, and FeH), and resonant lines from Na and K. As BT-SETTL13, Exo-REM accounts for non-equilibrium chemistry between CO, CH_4, CO_2, and NH_3 due to vertical mixing. The abundances of the other species are computed at thermochemical equilibrium. The vertical mixing is parametrized by an eddy mixing coefficient from cloud-free simulations. The cloud model includes iron, silicate, Na_2S, KCl, and water clouds. This grid is parametrized by four free parameters, which are T_{eff}, $log(g)$, $[M/H]$ and $^C/_O$, modeled for the values intervals listed in Table 1.1. The spectra can be recovered on the wavelength ranges listed in Table 1.1.

1.5.2   Forward Modeling: The Tool ForMoSA
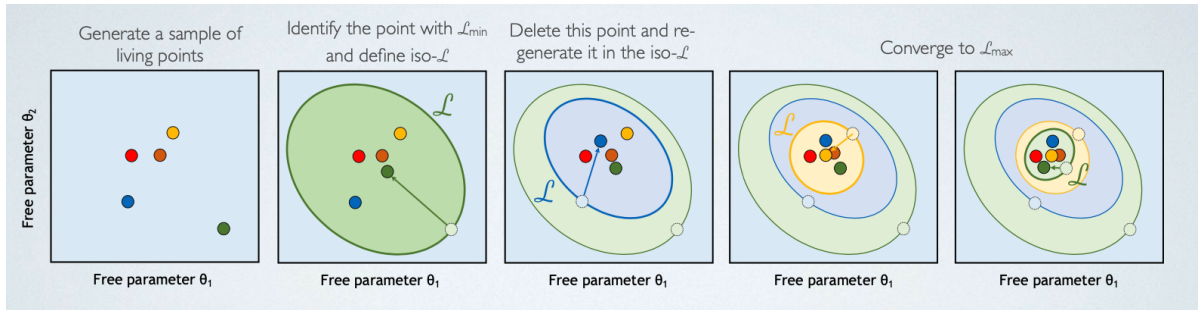
Figure 1.13: Visual explanation of the Nested Sampling algorithm. It restricts areas of equal likelihood at each iteration, from which the posteriors are a by-product. (Priv. Comm. Simon Petrus).

ForMoSA (Forward Modeling tool for Spectral Analysis), presented and detailed in Petrus et al. (2021), is a tool based on a forward-modeling approach that compares observations to grids of pre-computed synthetic atmospheric models using Bayesian methods. It relies on a Nested Sampling algorithm, described by Skilling (2006), to determine the posterior distribution function (PDF) of a set of free parameters, explained visually in Figure 1.13. This method performs a global exploration to look for local likelihoods maxima following an iterative method that isolates a progressively restrained area of same likelihood while converging toward the maximum values (see Figure 1.13). It avoids missing local maxima

of likelihood since it evaluates the Bayesian evidence used for performing model selection (Trotta, 2008). The errors given by ForMoSA are statistical and are determined for each parameter as the range which encompasses one sigma assuming Gaussian distributions, and they do not include possible systematic errors in the models (Petrus et al., 2021). Whenever the posterior distribution does not show a maximum, the user can define upper limits on the given parameter.

ForMoSA allows the user to fit for the fundamental parameters that describe an atmosphere, which are currently less than five. The basic ones are T_{eff} and $log(g)$, and depending on the model $[M/H]$ and $^C/_O$ ratio may be included, among other variations. Spectra can be affected by other physical processes like the Doppler shift due to the orbital movement and the broadening of the lines due to the planet's spin. Therefore, ForMoSA allows fitting for i/ the radius of the planet (R) to account for the flux normalization of the models given a known distance; ii/ the extinction coefficient (A_v) to consider extra reddening of the source due to dust or gas in the ISM or surrounding the object; iii/ the radial velocity (RV) to estimate the Doppler shift induced to the lines given the orbital motion of the target; iv/ the projected rotational velocity ($vsin(i)$) to explore possible broadening of the lines due to rotational effects; and v/ the limb-darkening necessary for the estimation of the lines broadening in the fitting of $vsin(i)$. By including these five parameters, the models are modified before being compared to the observations.

1.6   Tracers of Formation

In this section we review the general physical properties that characterize substellar objects connected to their formation processes. We start by analyzing the expected $[M/H]$ compared to the host star, the surface gravity and the orbital properties. Then we move to analyze the expected $^C/_O$ ratio for objects formed by the different mechanisms previously explained. Finally, we will analyze other proposed formation history tracers in literature, especially the $^{12}CO/^{13}CO$ ratio.

1.6.1   Physical & Chemical Properties

Observations have taught astronomers that the chemical composition of stars reflects pretty well the primordial conditions of the interstellar medium. Therefore, we can classify stars by population (1, 2, and 3) depending on their metallicity, which relates to their age and formation environments. When planets form, a protoplanetary disk surrounds the star, which organizes the disk by particle size and temperature, causing those different molecules to condense at different radii. Therefore, the formation mechanisms will impact the chemical elemental abundances on the atmospheres. The $[M/H]$ is interesting to analyze in this context, as shown in Table 1.2, but an enhancement of this value can come from core erosion and mixing into the envelope or late bombardment by planetesimals during and post runaway accretion.

Together with the previous idea, exoplanets usually have surface gravity values 100 to

1000 times smaller than BD, which affects the vertical mixing and gravitational settling of condensates in their atmospheres, leading to thicker cloud layers, upper atmosphere sub-micron hazes, and cloud opacities remaining down to T_{eff} of 600 K at early ages (Madhusudhan et al., 2011).

As previously mentioned, exoplanets can migrate. In this sense, constraining the orbital properties when studying wide orbit, young, direct imaged exoplanets, is fundamental. If the eccentricity of the orbit is low (~ 0), in situ formation mechanisms are favored. However, if the eccentricity is high, the companion probably suffered a planet-planet scattering event from which its orbit got elongated (Marleau et al., 2019). All these different proposed tracers can be studied when modeling the atmospheres and interpreting the posteriors compared to the expected characteristics of different formation scenarios.

Table 1.2: The expected metallicity $[M/H]$ relation between the host star and the companion depending on different formation mechanisms.

Formation Theories	Host vs Companion
GtF & Binaries	$[M/H]_{Host} = [M/H]_{Comp.}$
GI & TDH	$[M/H]_{Host} \leq [M/H]_{Comp.}$
CA & PA	$[M/H]_{Host} < [M/H]_{Comp..}$

1.6.2 The $^{C}/_{O}$ Ratio
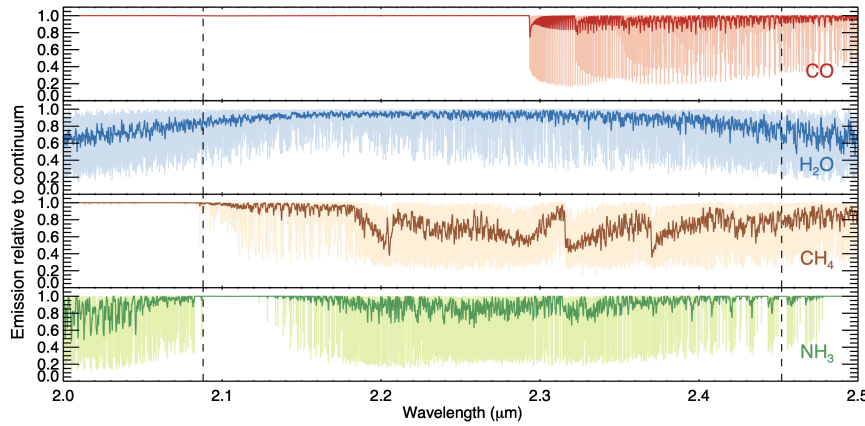
Figure 1.14: (Hoeijmakers et al. (2018), Figure 5) Model templates of CO, H_2O, CH_4 and NH_3 at high ($R \sim 106$) spectral resolution (light colour) and convolved to a spectral resolution of $R = 5000$ (dark colour). The vertical dashed lines indicate the wavelength range of the K band SINFONI data.

Connecting the $^{C}/_{O}$ ratio to theory can be done because it is a parameter that we can estimate. The atmospheric models are computed, as mentioned, by taking into account different physical mechanisms and the opacities of different elements, among them, CO, H_2O, and CH_4. As example, the K band model templates for CO, H_2O, CH_4 and NH_3

are observable in Figure 1.14, as reported by Hoeijmakers et al. (2018). These molecules have distinguishable features on this band, which is why we choose K band SINFONI data to perform this project. The $^C/_O$ ratio dependence on atmospheric mole fractions (N) is given in Equation 1.2, taken from Wilcomb et al. (2020) and is one way of measuring the $^C/_O$ from atmospheric models but does not mean that it is the only method. We do not use this definition for atmospheric modeling purposes, but it is interesting to observe. After this brief introduction on the $^C/_O$ measurements, we can study its expected values for different formation mechanisms.

$$\frac{C}{O} = \frac{N(CH_4) + N(CO)}{N(H_2O) + N(CO)} \tag{1.2}$$

$^C/_O$ Ratio for Stars
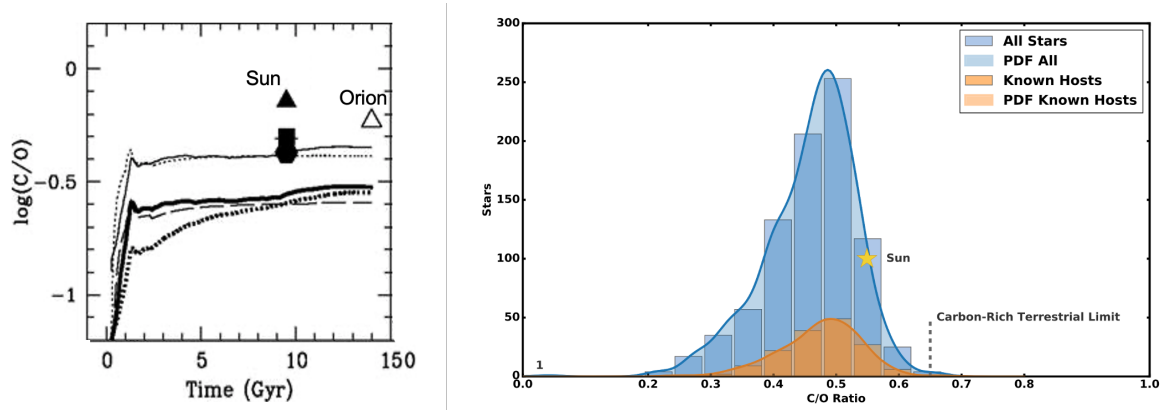
Figure 1.15: Left panel: (Chiappini et al. (2003), Figure 3, adapted) Time evolution of $^C/_O$ and $^N/_O$ in the solar vicinity for different models. Right panel: (Brewer and Fischer (2016), Figure 1) Distribution of $^C/_O$ ratio for a sample of 849 high S/N, slowly rotating dwarf stars from the catalog of Brewer and Fischer (2016) with $6100 > T_{eff} > 4800$. The orange portions of the bars indicate known planet hosts. Probability density functions (PDF) calculated using a Gaussian kernel density estimator and scaled to the area of the histograms are also presented. The gold star marks the position of the Sun in this sample ($^C/_{O_\odot} = 0.55$) and the dashed line marks the $^C/_O$ ratio at which it may be possible to form carbon-rich terrestrial planets.

As mentioned, the elemental composition of stars reflects pretty well the primordial conditions of the interstellar medium (ISM) from which it formed, a valid assumption for BD too if formed in the molecular cloud by any of the described theories. Therefore we can expect that these objects have an ISM $^C/_O$ ratio as well. We observe that the ISM has not had a constant metallicity during the evolution of the universe, and therefore the time of formation of a star will have a significant impact on its $^C/_O$ ratio (Chiappini et al., 2003) (see left panel of Figure 1.15) The different lines represent different models, but the crutial constraint is that for all models, the $^C/_O$ ratio of young systems is expected to be higher than for older ones. In this same line, Brewer and Fischer (2016) measured the $^C/_O$ ratio distribution for

stars which is observable on the right panel of Figure 1.15. We see the sun's position, and we expect that newly formed systems have values slightly higher, around 0.6 to 0.7.

$C/_O$ Ratio for Companions Formed by a Top-Down Process

A companion formed by GI or GtF should have an ISM $C/_O$ ratio on its atmosphere. These mechanisms are different since GtF happens directly inside the molecular cloud, but GI is a process that occurs at the early stages on an already formed protoplanetary disk. The reason why both these mechanisms are expected to have the same $C/_O$ ratio is because GI formation mixes solids and gas and happens at large separations, usually beyond the CO snow line; therefore, no variation in $C/_O$ compared to the ISM is expected.

However, the formation analysis must consider migration mechanisms and accretion of solid at final formation stages to account for the evolution and dynamics of the systems. If a BD is found to have an unexpected $C/_O$ ratio, a further analysis on the mechanisms that change this ratio, as done by Madhusudhan et al. (2016) can be performed. They studied the atmospheric composition of three brown dwarfs and found out that predominantly those targets have $C/_O > 0.7$ and sub-solar C and O abundances. Those results could indicate that the objects studied are from an early generation of stars or formed, for example, by a CA or GI process with further accretion of solids.

$C/_O$ Ratio for Companions Formed by a Bottom-Up Process
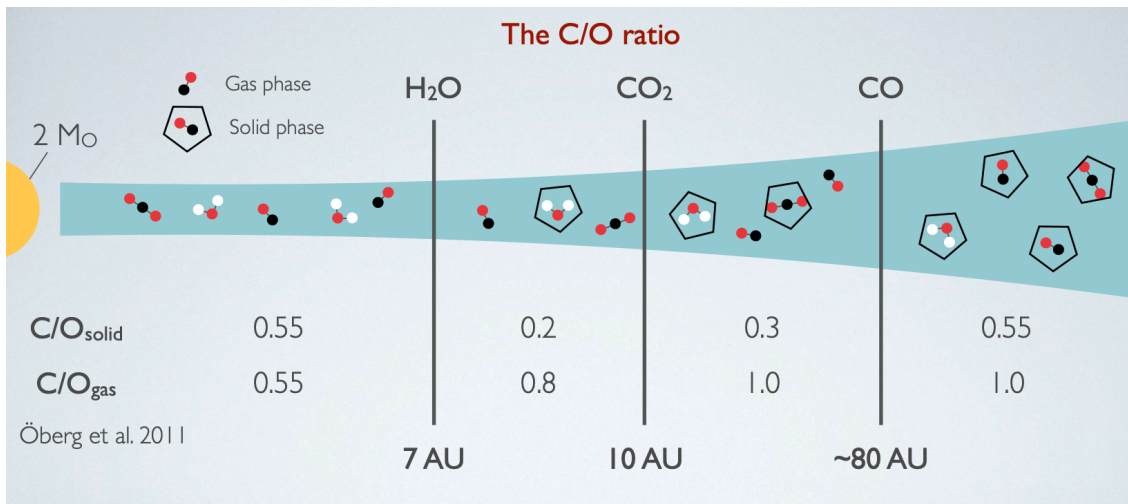
Figure 1.16: Variation of the $C/_O$ ratio of the gas and solids in a disc due to the CO, CO_2, and H_2O snow lines. The expected ratio between the snow lines is given in the bottom part of the figures for the solid and gas component. (Priv. Comm. Simon Petrus).

Carbon and oxygen are typical atoms, together with hydrogen, present in multiple molecules with different freezing temperatures. Therefore it has been proposed that the $C/_O$ ratio on the atmosphere of a young giant gaseous exoplanet could contain information about its location and history of formation. The $C/_O$ ratio vary for different radial locations for gas

and solids on the protoplanetary disk around the host star, as showed in Figure 1.16. The radial variation is triggered by the snow lines, for example, from H_2O, CO_2, and CO (Öberg et al., 2011). Massive planets formed by CA or PA accrete their gaseous envelopes at the final formation stages. Therefore the $^C/_O$ ratio of the planet's atmosphere will have the same value as the gas value at the location at which the exoplanet accreted its envelope (Madhusudhan, 2019).

The following key and less instinctive points are crucial for the understanding of these ideas:

- The giant planet's atmospheric composition depends on the relative amounts of gas and solids accreted from different locations in the disk relative to the snow lines. For example, the $^C/_O$ of an atmosphere can be lowered if the planet accretes solids at large separations since the solids have lower $^C/_O$ (see Figure 1.16).

- An early study on the $^C/_O$ was presented by Öberg et al. (2011) where they analyzed known host stars and studied how their $^C/_O$ varied as a function of radius and spectral type. One of their results is a direct radial dependency of the $^C/_O$ and a strong dependency on the host star spectral type. Expected, since less massive stars are less luminous, thus less hot and irradiate less their protoplanetary disk. The disk will be colder, and the snow lines closer in, resulting in an increase of the $^C/_O$ at shorter radius for colder stars.

- Stars change their temperature over time, producing a change in temperature for the protoplanetary disk over time. These temperature changes are strongly dependent on the star mass, observed in detail in the publication by Miley et al. (2021). For example, low-mass stars cool down with time, but more massive stars cool down during the first million years of their evolution to later increase their temperature again, which means that the snow lines will be changing their location over time. Thus, the proper understanding of the time of formation of giant exoplanets and the host stars' properties is crucial to relate later their $^C/_O$ ratio with their location of formation.

- Schneider and Bitsch (2021) shows the dependency of the $^C/_O$ ratio with the distance to the host star and found out that the $^C/_O$ ratio increases for the atmosphere of giant planets with increasing distance, but this variation does not depend just on the radius. They introduce the analysis of a second parameter simultaneously, which is the planetary mass, and found a correlation between mass and $^C/_O$ ratio.

- The migration of planets due to the interaction with the disk or other planets can significantly impact the atmospheric composition if the planet accretes solid bodies while changing its orbit, impacting, therefore, the $^C/_O$ ratio. However, tracing such a process is very difficult since many outcomes are possible for N-body interactions in a system.

In conclusion, to have a deep understanding of the location of formation of a planet formed through bottom-up mechanisms, the $^C/_O$ ratio will constitute a crucial piece of information. However, it is not sufficient since it can be affected by many external factors, and those degeneracies are challenging to overcome.

1.6.3 $^{12}CO/^{13}CO$ Isotopologues Ratio

Recently more tracers of formation location in protoplanetary disks have been proposed. Among them, an exciting tracer that could apply to these types of objects is the $^{12}CO/^{13}CO$ isotopologues ratio, proposed by Zhang et al. (2021) and by Molliere and Snellen (2019). In this line, Zhang et al. (2021); Zhang and Snellen (2021) measured that a young isolated BD has a roughly ISM $^{12}CO/^{13}CO = 97^{+25}_{-18}$ while TYC 8998, a wide orbit (150au) companion has a $^{12}CO/^{13}CO = 31^{+17}_{-10}$ probably due to a significant accretion of ^{13}C enriched ice at its final formation process, respectively. In Figure 1.17 a schematic representation of how the $^{12}CO/^{13}CO$ ratio may vary for exoplanets formed far outside in protoplanetary disks can be observed. This idea promises, together with the $^C/_O$ measurement, to have reliable constraints on the location of formation of giant planets at wide orbits.
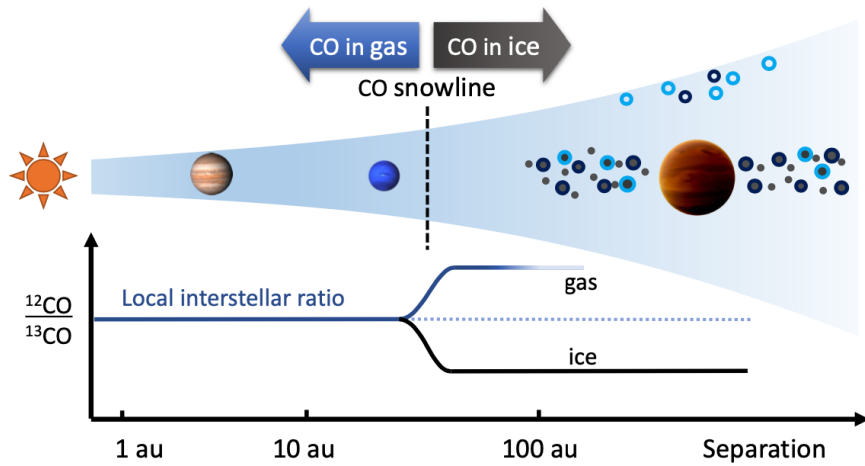
Figure 1.17: (Zhang et al. (2021), Figure 3) Cartoon of the birth environments of planets in a proto-planetary disk. Beyond the CO snow line carbon is expected to have been locked up in CO-ice and formed the main reservoir of carbon in the planet. Far outside the CO snowline, the ice is ^{13}CO or ^{13}C rich through carbon fractionation.

1.6.4 Other Proposed Tracers: $\mathbb{S}$, N, Noble Gases

The measurements of $[M/H]$, eccentricity, $^C/_O$, and $^{12}CO/^{13}CO$ of exoplanets atmospheres promise to unveil the formation history of these targets. However, this is a very young field, and many other tracers can be found that may contain valuable information for studying the formation and evolution history of these targets. For example, Marley et al. (2007) suggested that young giant planets formed by CA in a protoplanetary disk should have a much lower entropy content ($\mathbb{S}$) at young ages than objects of the same mass and age formed by GI. Another possible approach has been proposed by Öberg and Wordsworth (2019) where they trace the nitrogen (N) abundance and use the N_2 and NH_3 snow lines together with noble gases snow lines of Xe, Kr and Ar and the usual H_2O, CO_2 and CO snow lines to trace back the location of formation of Jupiter. If we can observe the emission or absorption lines of those molecules (not the noble gases) by direct imaging techniques, the measurement of

those abundances will be excellent to trace back the location using other elements.

The mentioned ideas are just some examples of other proposed formation tracers that, together with the $^C/_O$ ratio, could significantly improve the current constraints, mainly regarding the formation location and mechanisms of giant exoplanets and BD. Potentially, we could even differentiate between the populations of BDs and giant exoplanets that currently share many observational characteristics that make them impossible to split. This topic has driven this research; therefore, we are excited to see where these ideas are taking us with the upcoming generation of telescopes and models.

1.7   The Contributions of This Work

The atmospheric characterization of young isolated objects at wide orbits with the scope of understanding the formation and evolution history of the targets is a relatively new research topic. Currently, planets are being discovered, models are being developed, and theories are being adapted. This master project is located in this big evolving topic as previously described but has a clear objective in mind.

Our purposes are to understand the potential differences between exoplanets and BD, mainly regarding their formation process, for which we selected a sample of 24 targets observed with SINFONI at the K-band. This sample and the reduction process are described in Chapter 2. In that chapter we present the final extracted and corrected spectra for each one of the targets, which are detailed individually in the Appendix A. These reduced spectra are one of the contributions of this work, since they compose an important library for a wide study of these type of objects. The complete exploration and publication of the atmospheric properties of the SINFONI library, described in Chapter 2, will start in the coming weeks.

Given the particular interest in the massive super-Jupiter AB Pic b, we decided first to revisit its atmospheric properties, nature, and origin. We present this part of the project in Chapter 3. The main results are a deep analysis of AB Pic b's physical and orbital properties and a proposed formation history based on the outcomes. The crucial parameter we report, which has not been measured before and we will publish soon, is the $^C/_O$ ratio of 0.6 ± 0.1. As a spoiler, we proposed that AB Pic b was formed in the protoplanetary disk, more likely through GI or CA/PA at large separation, beyond the CO snow line. However, given the current knowledge of the system, other scenarios like GtF cannot be ruled out. A summary and the conclusions are presented in Section 4.

Chapter 2

The SINFONI Library

We started this project with the primary objective of understanding the connections between atmospheres and formation theories, for which we selected a set of similar, in mass and age, substellar companions and isolated objects. Twenty-four targets were chosen for which archival SINFONI K band observations were available. The first step was to characterize the targets, then to reduce their observations and extract a spectrum for each one. Finally, we analyzed their characteristics by comparing them to evolutionary models predictions and their architectures.

2.1 The Data

2.1.1 Observations

Our sample consists of 24 young (from 1 to 30 Myr) planetary-mass objects within $150\,\mathrm{pc}$ from the solar system. They are members of the following associations: AB Doradus, β Pic, Carina, Taurus, Tucana, and Upper Scorpius; and are found in different architectures: 13 are isolated objects 11 are companions orbiting a star at significant separation. The spectral types of the sample are between M5 and L5, with T_{eff} from 1500 to 2500 K, and masses ranging from 5 to 70 M_{jup}. All this information is summarized in Tables 2.1 and 2.2.

As mentioned, the targets were observed with SINFONI at the VLT on different dates as part of different programs (see Table 2.3). SINFONI was composed of a custom adaptive optics module (MACAO) and an IFS (SPIFFI). SPIFFI cuts the field-of-view into 32 horizontal slices (slitlets), which are re-aligned to form a pseudo-slit, and dispersed by a grating on a Hawaii 2RG ($2k \times 2k$) detector (Eisenhauer et al., 2003; Bonnet et al., 2004). The instrument was operated with pre-optics and a grating sampling rectangular spaxels sizes listed on Table 2.3, from 1.928 - 2.471 μm, at a spectral resolution of $R_\lambda = \frac{\lambda}{\Delta\lambda} = 4490/5090/5950$ for Platescales of 0.25/0.1/0.025 arcseconds respectively, which are listed on Table 2.3. MACAO was used during some of the observations with a natural guide star (NGS) reference for the wave-front sensing. The number of exposures per sequence, integration times, and frames (ndit) for each target and observation day is reported on Table 2.3. All observations were

centered on the expected position of the planet.
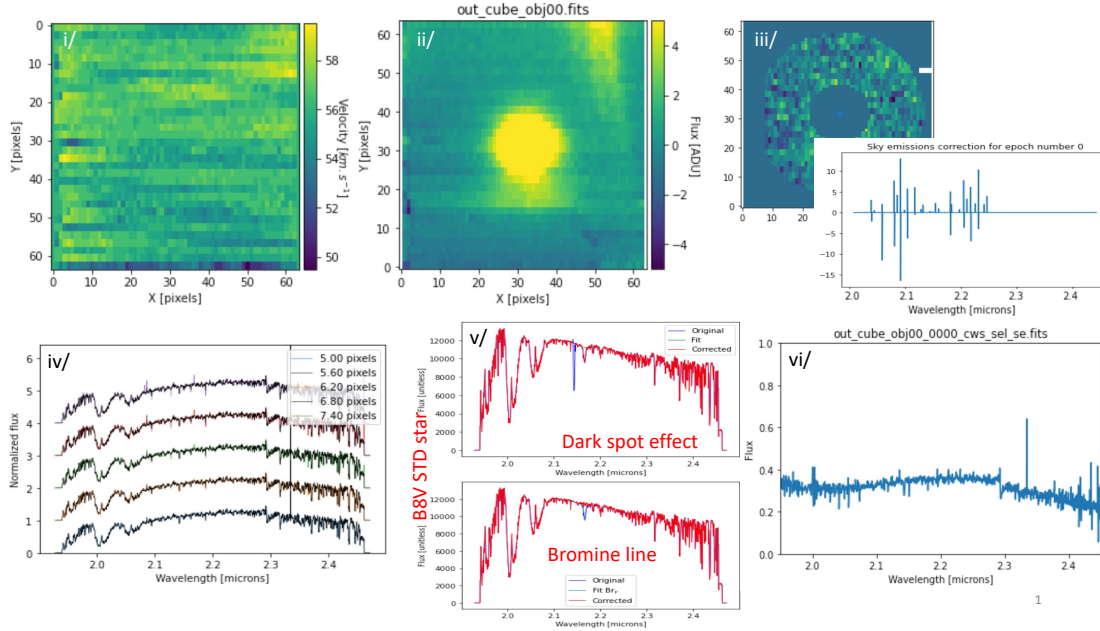
Figure 2.1: A schematic view of the reductions steps using AB Pic b as example. The same procedure was repeated for each of the targets. On panel i/, a view of the wavelength shifts; on panel ii/ a preliminary view on the companion to identify possible contamination sources; on panel iii/, the masked cube and the extracted sky emission lines; on panel iv/, a test of different aperture radius where the companion spectrum is observable and at short wavelengths we identify the earth's atmospheric water bands; on panel v/, the STD corrections and its preliminary spectrum from which we aim to extract the atmospheric transmission spectrum; on panel vi/, one of the cubes final spectrum, before median combine to extract the final result.

2.1.2 Reduction & Corrections

We initially reduced the data with the ESO SINFONI data handling pipeline[1] v3.0.0 through the EsoReflex[2] environment. The pipeline use calibration frames to perform basic adjustments to the raw science frames and correct them from distortion. The slitlets position on the frames at each wavelength is identified before building a datacube for each exposure. Further corrections on top of the ESO reduction steps were performed, based on the *Toolkit for Exoplanet deTection and chaRacterization with IfS* (hereafter TExTRIS) on its seventh beta version (Petrus et al. 2021; Bonnefoy et al. in prep) and customized Python routines.

A schematic view of the steps can be found in Figure 2.1 using AB Pic b as example and a detailed explanation of these methods is given below:

---

[1]https://www.eso.org/sci/software/pipelines/sinfoni
[2]www.eso.org/sci/software/esoreflex

i. As implemented by Petrus et al. (2021), the method identifies a constant wavelength shift using the telluric absorption lines. We corrected both, the companions and the telluric standard stars (STD), from spaxels-to-spaxels wavelength shifts. The implemented method does not have the possibility of reporting uncertainties, but it is currently being developed. By comparing the calibrations of the same source but observed in two different nights, it has been observed a discrepancy in the wavelength recalibration of $\sim 15km/s$; therefore, we expect the uncertainties to be around that value. From pixel to pixel, the uncertainties are expected to be insignificant.

ii. We checked that the light from the target was not contaminated by other emission sources, as the host star, and evaluated the target's position and the telluric standard star (STD) in each respective cube. This process is done by an eye inspection and one example cube can be observe in panel ii/ of Figure 2.1. For two of the targets, GSC 06214 B and RXJ 1609 B, the light of the companion was contaminated by the primary. In order to decontaminate the spectrum of the targets we tested a spectral deconvolution routine, which is still being developed.

iii. To further correct for sky emission lines we adjusted an order 0 or 1 polynomial to masked image of the sky, as shown in top image of panel iii/ in Figure 2.1. Subtracting the fitted polynomial from the masked image we computed the emission contributions of the sky. An example of these contributions is observable on the bottom image of panel iii/ of Figure 2.1, which we then subtracted to each original cube.

iv. We measured the motion of a point source affected by atmospheric refraction and reported the estimated source coordinates fitting a polynomial function in each cube slice and played by adjusting the polynomial degree and the initial guess for the expected position of the target. For the STD frames, we binned the cubes in wavelengths to reduce computation time.

v. Different extraction radius centered at the source position were evaluated to find the optimal aperture to extract the spectrum of each cube (see Figure 2.1, panel 1v/ for an example). We found that the spectral slope, in general, does not change for increasing apertures, and the S/N seems higher for smaller apertures; thus, we set the aperture radius to 5 pixels. The angular size of the SINFONI slices on the sky can be 0.25, 0.1, or 0.025 arc-seconds (platescale parameter on Table 2.3), leading to a field of view on the sky of 8x8, 3x3, or 0.8x0.8 arc-seconds. Then, an aperture of radius 5 pixel corresponds to 1.25, 0.5, or 0.125 arc-seconds, respectively. The FWHM of the targets emission, if we consider that their flux distributes like a Gaussian on the FoV, is around 8.86 pixels for PZ TEL B, which is a very faint target, and around 5.03 pixels for AB Pic b which is a bright target. The FWHM for the other targets lay between these values; thus, our aperture radius is set to > 1 FWHM for the brightest targets and to ~ 2 FWHM for the faintest ones.

vi. The contamination by water bands of the earth atmosphere is recognizable in this preliminary extracted spectrum in panel iv/ of Figure 2.1, which is why a STD was observed for each target. To correct for the H_2O bands, we needed to compute a spectrum of the atmospheric transmission for each night. We corrected the STD and target spectrum of each night from the dark spot effect of the detector known to affect the K-band data by fitting a one-dimensional polynomial from $2.14 - 2.15 \mu m$. Next,

we corrected the NIR Hydrogen (H) lines from the STD spectrum by fitting a Voigt profile. The function corrects for specific Paschen (Pa_β) and Brackett (Br_{16}, Br_{14}, Br_{12}, Br_{11}, Br_{10}, and Br_γ) series lines that may be observable on the NIR. We then visually inspected these corrections, and using the spectral type of the STD star, we estimated its expected T_{eff} and computed the corresponding theoretical black-body (bb) spectra. We corrected each STD spectrum by dividing to it the computed bb. The result of this process is the atmospheric transmission signatures for each night. Finally, each spectrum of the targets were corrected by dividing the atmospheric transmission spectrum to it. One of the spectrum, as example, can be observable in panel vi/ of Figure 2.1.

vii. We selected all high-quality spectra by making a visual inspection and mean-combined them, ending with a final spectrum for each target with the corresponding errors, that were computed by mean-combining the errors of each spectrum and dividing it by the root of the number of datacubes considered. Before merging, we applied a Doppler shift and the Barycentric correction to each frame to correct for the earth's motion.

We calibrated the extracted normalized spectra in flux units using the K-band magnitude values reported in Table 2.1 and 2.2 from literature and online sources. The extracted spectra for each target are observable in Figure 2.2 together with the errors in grey.

2.1.3   Final Extracted Spectra

In Figure 2.2 the final extracted K-band SINFONI spectrum for each of the targets of the sample are observable. The quality of the observations depends on the platescale, AO mode and the specific atmospheric conditions of the night. All this information can be found in Table 2.3. A detailed explanation of each target spectrum is given in Appendix A. As mentioned, the spectrum extracted for GSC 06214 B and RXJ 1609 B cannot be trusted since their light is contaminated by the host star.

2.2   Evolutionary Models & Architectures

For now, we have not performed a detailed atmospheric model exploration for all the targets of the sample, but we study the behavior of the sample in connection to the predictions from evolutionary models. From this approach we have an approximate idea of the expected outcomes of the models. For instance, we study two approaches for comparing our library to evolutionary models. First, the relation between luminosity, age, and spectral type, which can be observed in Figure 2.3 where the 24 selected targets are placed on their pre-main-sequence evolutionary tracks based on the models from Baraffe et al. (2015).

In Figure 2.3 we see the luminosity, age and spectral type distribution of the sample placed over curves with constant mass values. As labeled on the figure, the colors for the curve represent the cut for object with masses under $13M_{jup}$ and above it, up to $73M_{jup}$. The limit of $13M_{jup}$ is important, since under this value the deuterium cannot be burned-out. The
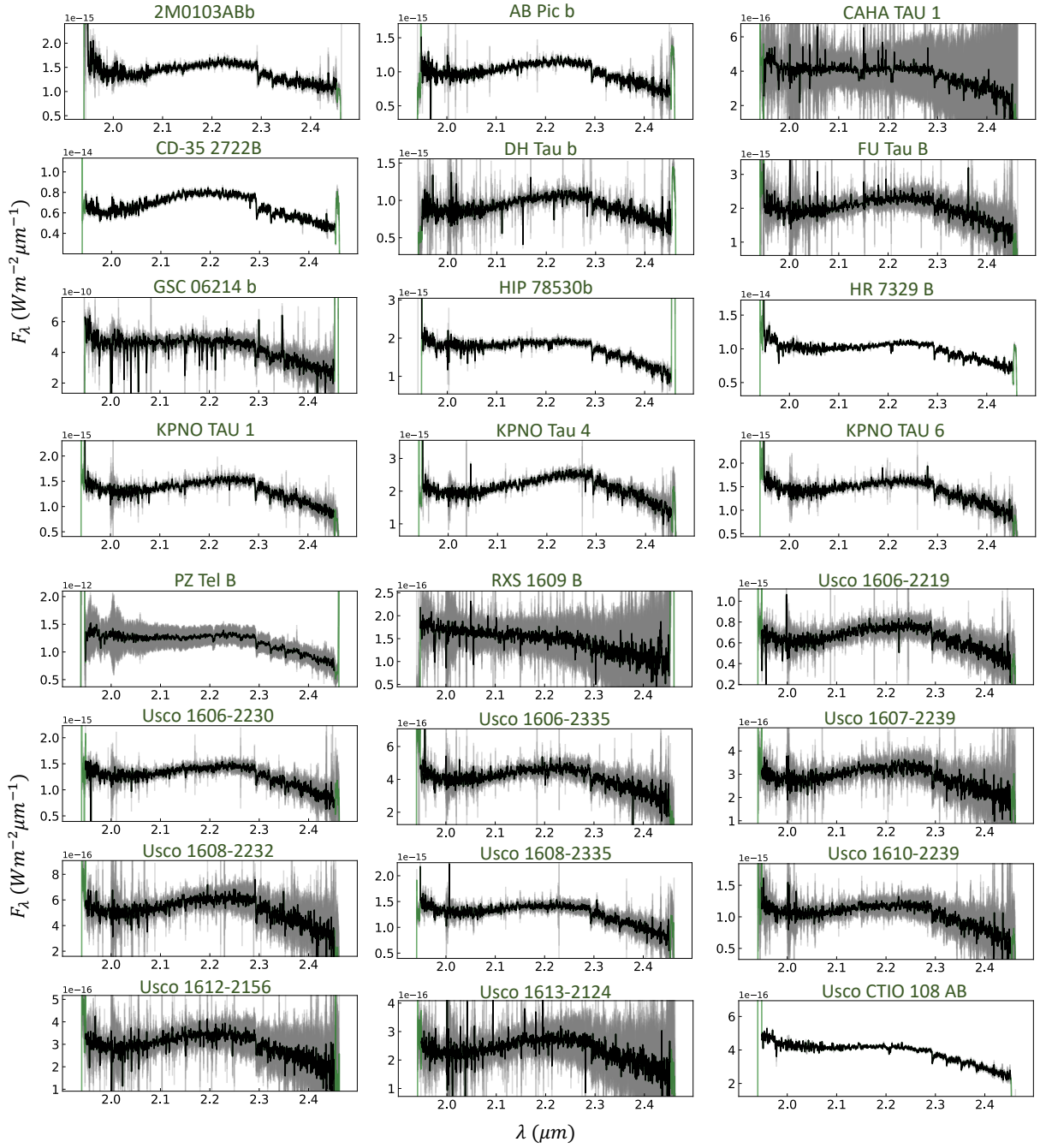
Figure 2.2: Final spectrum extracted for each of the 24 targets. The size of the error bars (gray) strongly depends on factors such as the plate-scale, integration time, and the availability of the AO system. See Appendix A for a detail analysis on each extracted spectrum.
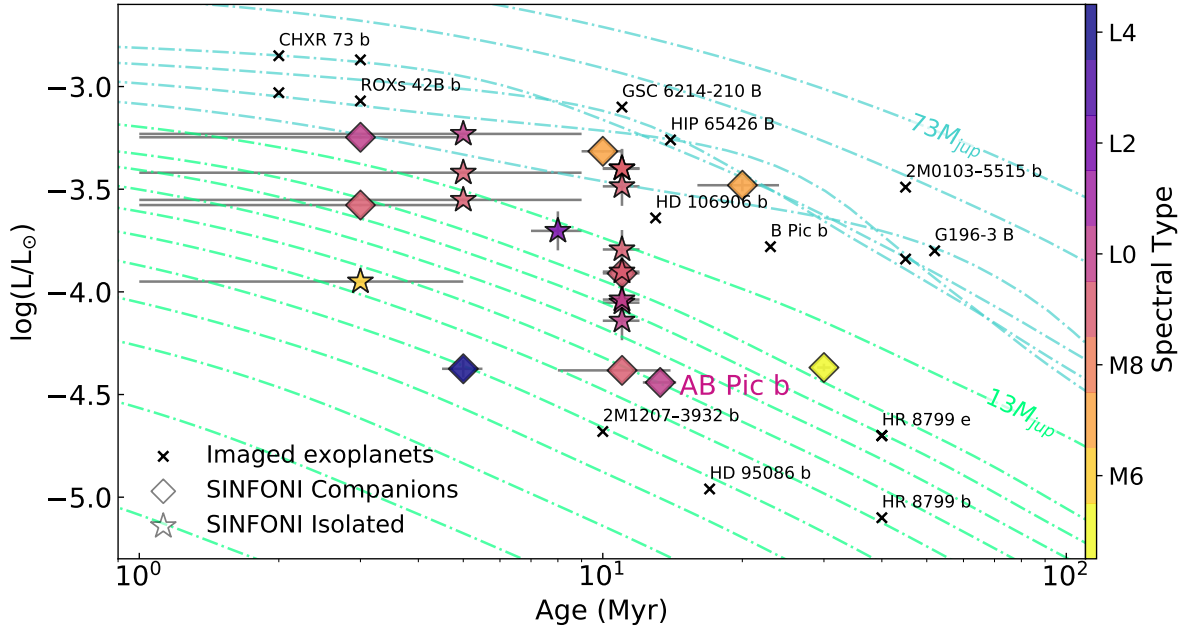
Figure 2.3: Pre-main-sequence evolutionary tracks. A relation between the luminosity, age, mass, and architecture of the targets can be seen. Different symbols refer to the system architecture; the ones marked with star symbols are isolated, while those marked with a circle are companions. For all targets, the errors in luminosity and age are marked with gray bars. The sample marked with an x symbol represents literature data from directly imaged companions.

limit of $73M_{jup}$ is interesting as well, since above this value, cores are hot enough to start Hydrogen fusion. This is actually the lower mass limit for stars (Baraffe et al., 2015).

From Figure 2.3 it can be observed that there is no clear trend which separates the isolated targets from the companions, which is expected given the arguments previously exposed. BD and companions share many observables and from their luminosity and spectral type, in connection to their age, we are not able to differentiate the two populations.

Following with the evolutionary models, we tested next the BEX Hottest cond03 evolutionary models (Marleau et al., 2019). The relationship between radius, surface gravity, mass and temperature can be observed in Figure 2.4. From the models we observe isotemperature tracks as function of the surface gravity and the radius and the age of the system colored above.

For calculating the positions on the diagram for each target we used the K band magnitudes that we report on Table 2.2, which we converted to absolute magnitude using the previously reported distances of the systems, observable on Table 2.1. With the absolute K band magnitude we explored the tabulated BEX Hottest cond03 evolutionary models and extracted the corresponding radius and surface gravity. The errors were propagated accordingly and are reported with gray bars in the figure for each target. For comparison, we colored each target by its spectral type as done in Figure 2.3.
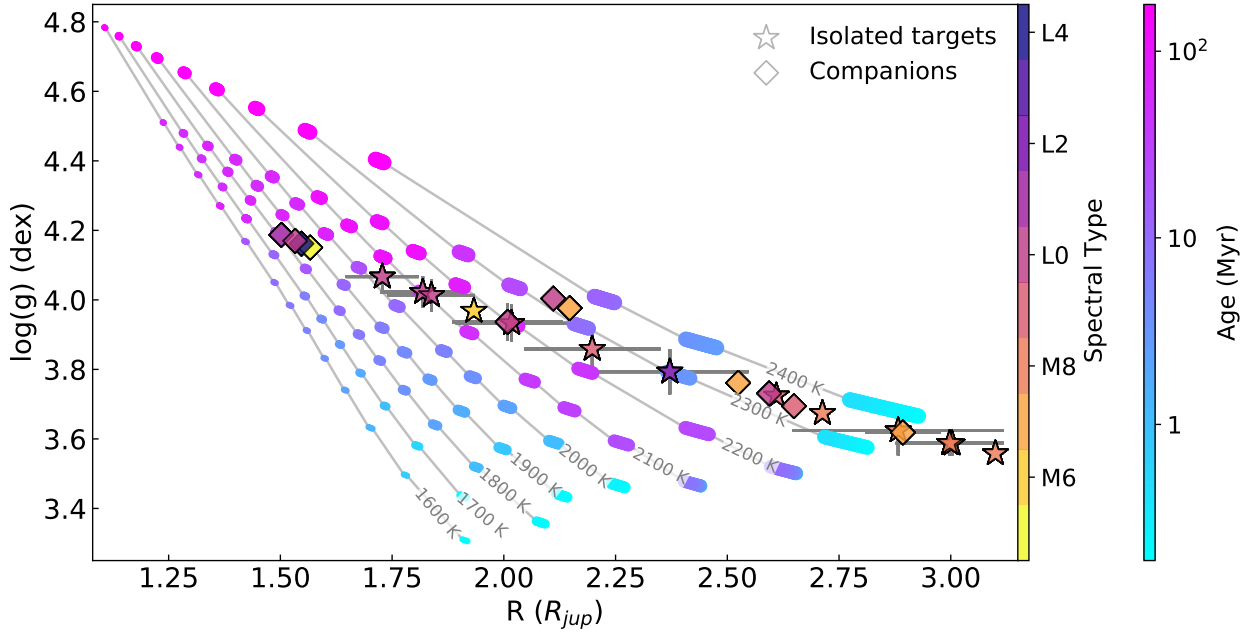
Figure 2.4: Pre-main-sequence evolutionary tracks from hottest BEX cond03 models. A relation between the radius, surface gravity ($log(g)$), age, and T_{eff}. Different symbols refer to the system architecture; the ones marked with star symbols are isolated, while those marked with a circle are companions. For all targets, the errors in luminosity and age are marked with gray bars.

2.3 Discussions & Perspectives

As future perspectives of this work, we are looking forward to publishing an updated library of NIR spectra for young planetary-mass companions and isolated objects and their most relevant physical and chemical properties. To distinguish between BD and massive planets, we will analyze the parameter space looking for patterns describing likely and unlikely scenarios given their characteristics, primarily we aim to study the $^C/_O$ ratio and how it distributes concerning the architecture of the systems. Even though the sample is not extensive enough to make statistical constraints, we expect to see a tendency favoring different formation processes for the different architectures.

Due to the time extension of the Ms.C. program, the complete atmospheric characterization of the sample was too ambitious. Therefore, we decided to do a careful and deep analysis on one of the sources of the presented sample, which has a rich set of literature data available. Therefore we stop this section at this point, with many future perspectives in mind, and change in the next chapter to talk about AB Pic b exclusively.

Name	RA	Dec	D_{sun} (pc)	Asociation	Age (Myr)
2M0103ABB	01 03 35.75	-55 15 55.5	47.2 ± 1	Tucana-Horologium	30 ± 1
AB Pic b	06 19 12.91	-58 03 15.52	50.14 ± 0.04	Carina	13.3 ± 1.1
CAHA TAU 1	04 36 09	24 08 22.3	140 ± 15	Taurus	3 ± 2
CD-35 2722B	06 09 19.20	-35 49 31.06	21 ± 1	AB Doradus	5 ± 0.5
DH TAU B	04 29 42.0	26 32 58	134.85 ± 1.5	Taurus	3 ± 2
FU TAU B	04 23 35.0	25 03 03	131.2 ± 2.5	Taurus	3 ± 2
GSC06214B	16 21 54.4	-20 43 15.5	145 ± 15	Upper Sco OB	7.5 ± 1
HIP78530B	16 01 55.91	-21 58 52.9	137 ± 1	Upper Sco	10 ± 1
HR 7329 B	19 22 51.26	-54 25 30.7	47.67 ± 1.6	β Pic	20 ± 4
KPNO TAU 1	04 15 14.53	28 00 23.2	140 ± 1	Taurus	5 ± 4
KPNO TAU 4	04 27 27.74	26 12 05.8	140 ± 1	Taurus	5 ± 4
KPNO TAU 6	04 30 07.2	26 08 20.6	116 ± 1	Taurus Auriga	5 ± 4
PZ TEL B	18 53 05.87	-50 10 50.0	51.5 ± 2.6	β Pic	23 ± 3
RXS1609B	16 09 30.37	-21 04 57.4	139.14 ± 1.3	Upper Sco	11 ± 3
USCO1606-2219	16 06 03.84	-22 19 34	145 ± 15	Upper Sco	8 ± 1
USCO1606-2230	16 06 48.32	-22 30 43.7	145 ± 15	Upper Sco	11 ± 1
USCO1606-2335	16 06 06.46	-23 35 17.4	145 ± 15	Upper Sco	11 ± 1
USCO1607-2239	16 07 27.56	-22 39 08	145 ± 15	Upper Sco	11 ± 1
USCO1608-2232	16 08 18.59	-22 32 28.7	145 ± 15	Upper Sco	11 ± 1
USCO1608-2335	16 08 30.19	-23 35 14.8	145 ± 15	Upper Sco	11 ± 1
USCO1610-2239	16 10 46.88	-22 39 53.4	145 ± 15	Upper Sco	11 ± 1
USCO1612-2156	16 12 27.79	-21 56 44.6	145 ± 15	Upper Sco	11 ± 1
USCO1613-2124	16 13 02.45	-21 24 32.9	145 ± 15	Upper Sco	11 ± 1
USCOCTIO108AB	16 05 53.87	-18 18 48	145 ± 15	Upper Sco	11 ± 1

Table 2.1: In this table, the first part of the general information for the SINFONI Library, regarding its positions on the sky and ages, is observable. The right ascension (RA) and declination (Dec) are in ICRS J2000 format. The corresponding references are to be found on the final column in Table 2.2.

Name	Sp.T.	K mag	D_{host} (AU)	Host Sp.T.	Ref.
2M0103ABB	$M5.1 \pm 0.6$	9.237 ± 0.022	84 ± 1	$M6$	1,2,3,4
AB Pic b	$L0.5 \pm 0.5$	14.090 ± 0.08	273 ± 1	$K2$	1,4,5,6ab,7,8,9,10
CAHA TAU 1	$M6 \pm 5$	15.110 ± 0.09	$-$	$-$	1,11,12
CD-35 2722B	$L4.5 \pm 5$	10.37 ± 0.16	67 ± 1	$M1$	1,4,13
DH TAU B	$M9.25 \pm 0.25$	14.19 ± 0.02	330 ± 5	$M0.5$	1,6b,8,14
FU TAU B	$L0.25 \pm 0.25$	13.329 ± 0.098	800 ± 10	$M7.25$	1,11,14
GSC06214B	$L0 \pm 1$	14.92 ± 0.03	320 ± 10	$K0$	1,3,16,17,18
HIP78530B	$M7 \pm 1$	13.491 ± 0.003	623 ± 8	$B9$	1,17,19
HR 7329 B	$M7 \pm 1$	11.6	136 ± 10	$A0$	1,6b,20
KPNO TAU 1	$M8.5 \pm 0.5$	13.772 ± 0.035	$-$	$-$	1,21
KPNO TAU 4	$M9.5 \pm 0.5$	13.28 ± 0.03	$-$	$-$	1,6b,11,21
KPNO TAU 6	$M8.5 \pm 0.5$	13.689 ± 0.037	$-$	$-$	1,21,22
PZ TEL B	$M7 \pm 1$	6.366 ± 0.024	25 ± 4	$G6.5$	1,23,24
RXS1609B	$M9.5 \pm 0.5$	16.170	330 ± 10	$M0$	1,8,14,17,18,25
USCO1606-2219	$L2 \pm 1$	14.550 ± 0.086	$-$	$-$	1,26
USCO1606-2230	$M8 \pm 0.5$	13.806 ± 0.042	$-$	$-$	1,26
USCO1606-2335	$M9 \pm 0.5$	15.052 ± 0.161	$-$	$-$	1,19,26
USCO1607-2239	$L0 \pm 0.5$	15.436 ± 0.019	$-$	$-$	1,26
USCO1608-2232	$M9 \pm 0.5$	14.775 ± 0.113	$-$	$-$	1,19,26
USCO1608-2335	$M8.5 \pm 0.5$	13.814 ± 0.054	$-$	$-$	1,26
USCO1610-2239	$M8.5 \pm 0.5$	14.025 ± 0.058	$-$	$-$	1,19,26
USCO1612-2156	$L0 \pm 1$	15.395 ± 0.166	$-$	$-$	1,26
USCO1613-2124	$L0 \pm 1$	15.652 ± 0.022	$-$	$-$	1,26
USCOCTIO108AB	$M9.5 \pm 0.5$	15.067 ± 0.012	667 ± 10	$M7$	1,6b

Table 2.2: In this table, the second part of the general information for the SINFONI Library, regarding its spectral type (Sp.T), K band magnitude, and host star properties (when they are companions), can be observable. The corresponding references are found on the right column and are detailed below.

References: (1) Wenger et al. 2000, (2) Liu et al. 2013, (3) Kraus et al. 2014, (4) Stone et al. 2016, (5) Chauvin et al. 2005, (6 a,b) Bonnefoy et al. 2010, 2014, (7) Patience et al. 2012, (8) Martinez and Kraus 2021, (9) Booth et al. 2021, (10) Gaia Collaboration et al. 2021, (11) Quanz et al. 2010, (12) Luhman and Mamajek 2010, (13) Wahhaj et al. 2011, (14) Wu et al. 2020, (15) Cheetham et al. 2015, (16) Bowler et al. 2011, (17) Lachapelle et al. 2015, (18) Ireland et al. 2011, (19) Petrus et al. 2019, (20) Lowrance et al. 2000, (21) Briceno et al. 2002, (22) Akeson et al. 2019, (23) Maire et al. 2016, (24) Stolker et al. 2020, (25) Lafrenière et al. 2008, (26) Lodieu et al. 2011.

PI & Program	Name	Date	Mode	Platescale (arcsec)	Exposure (s)	ndit	nexp	Airmass	Seeing (FWHM)
Kopytova	CD-35 2722B	26-11-2013	NGS	0.1	150	4	8	1.055 - 1.354	1.04 - 1.66
092.C-0803(A)	2M0103ABB	18-07-2014	NGS	0.1	70	8	9	1.159 - 1.183	-1 - 1.53
093.C-0829(A&B)		11-08-2014	NGS	0.1	70	16	9	1.126 - 1.186	-1 - 1.32
		15-08-2014	NGS	0.1	70	8	9	1.145 - 1.202	1.02 - 1.74
	HR 7329 B	05-06-2014	NGS	0.025	60	8	9	1.155 - 1.182	-1 - 1.19
		25-04-2014	NGS	0.025	60	8	9	1.152 - 1.170	-1 - 2.14
		11-07-2014	NGS	0.025	60	8	9	1.152 - 1.175	1.31 - 1.87
	PZ TEL B	20-04-2014	NGS	0.025	60	8	9	1.125 - 1.161	0.7 - 0.85
		04-05-2015	NGS	0.025	60	5	10	1.108 - 1.264	0.69 - 0.87
		28-07-2015	NGS	0.025	10	9	10	1.115 - 1.151	-1 - 1.73
Radigan	USCO1606-2219	18-05-2014	NOAO	0.25	300	4	4	1.016 - 1.030	0.81 - 1.08
093.C-0502(A)	USCO1606-2230	02-06-2014	NOAO	0.25	150	4	4	1.261 - 1.299	0.82 - 0.90
	USCO1606-2335	21-05-2014	NOAO	0.25	600	3	3	1.006 - 1.019	0.86 - 0.98
	USCO1607-2239	21-05-2014	NOAO	0.25	600	6	2	1.005 - 1.108	0.74 - 0.99
		28-05-2014	NOAO	0.25	600	2	2	1.005 - 1.01	0.74 - 0.99
	USCO1608-2232	21-05-2014	NOAO	0.25	300	4	4	1.188 - 1.244	0.99 - 1.56
	USCO1608-2335	19-05-2014	NOAO	0.25	150	4	4	1.057 - 1.071	1.21 - 1.38
	USCO1610-2239	27-04-2014	NOAO	0.25	150	4	4	1.366 - 1.414	1.36 - 1.79
	USCO1612-2156	18-05-2014	NOAO	0.25	600	4	4	1.059 - 1.117	0.74 - 1.91
		18-05-2014	NOAO	0.25	600	3	3	1.219 - 1.299	1.31 - 1.37
	USCO1613-2124	19-05-2014	NOAO	0.25	600	4	4	1.008 - 1.032	1.20 - 1.55
		20-05-2014	NOAO	0.25	600	3	3	1.179 - 1.248	-1
	USCOCTIO108AB	17-06-2014	NOAO	0.25	300	5	5	1.010 - 1.023	-1 - 1
	HIP78530B	28-05-2014	NGS	0.25	600	4	4	1.049 - 1.102	-1 - 1.09
		28-05-2014	NGS	0.25	600	4	4	1.112 - 1.194	1.03 - 1.22
	GSC06214B	07-07-2014	NGS	0.25	600	4	4	1.303 - 1.469	0.65 - 1.04
	RXS1609B	27-05-2014	NGS	0.25	600	7	4	1.017 - 1.176	-1 - 1.27
		08-07-2014	NGS	0.25	600	3	3	1.002 - 1.008	0.88 - 0.95
092.C-0535(A)	CAHA TAU 1	10-10-2013	NOAO	0.25	600	3	5	1.516 - 1.556	0.68 - 0.88
		11-10-2013	NOAO	0.25	60.	4	5	1.581 - 1.677	0.61 - 0.75
	DH TAU B	09-11-2013	NGS	0.025	900	2	3	1	1
		09-11-2013	NGS	0.025	900	2	3	1	0 - 1
		03-12-2013	NGS	0.025	900	2	3	1	1
	FU TAU B	09-10-2013	NOAO	0.25	100	6	9	1.645 - 1.770	-1 - 2.24
	KPNO TAU 1	07-10-2013	NOAO	0.25	300	6	9	1.646 - 1.663	0.94 - 1.24
	KPNO TAU 4	08-10-2013	NOAO	0.25	150	6	9	1.590 - 1.623	-1 - 0.63
	KPNO TAU 6	11-10-2013	NOAO	0.25	300	6	9	1.579 - 1.595	0.62 - 0.79
Patience	AB Pic b	01-12-2014	NGS	0.1	300	5	6	1.198 - 1.205	0.67 - 1.08
092.C-0809(A)		15-12-2013	NGS	0.1	300	5	6	1.245 - 1.283	0.66 - 1.02

Table 2.3: Observation log of the dataset that compose our SINFONI Library. All the information was taken from the headers of the datacubes.

Chapter 3

AB Pic b, a companion on the exoplanet/ brown dwarf boundary

AB Pic b is a companion that has been studied multiple times since its discovery by Chauvin et al. (2005). The central part of this master project was focused on a detailed characterization of the atmosphere of this companion. The scope was to unveil the formation and evolution history of AB Pic b through the signatures and imprints on its spectrum and other properties as the orbital constraints. All the work done for AB Pic b can be found in the publication in preparation which is attached on this chapter, in the following sections, with an adapted format to fit the requirements of the present document. This research will, hopefully, be published soon in Astronomy & Astrophysics. The publication is being written as a contribution of many authors, listed on the next page and it is essential to mention that the atmospheric modeling and general writing constitute the main results of this master thesis project under direct supervision of G. Chauvin, M. Bonnefoy and P. Rojo, but co-authors, specifically L. Rodet, G. Chauvin and M. Langlois performed the orbital models and the writing of sections 3.2.1 and 3.3. The other authors of the publication contributed in the computation of the different implemented models.

Unveiling the origins of AB Pic b through its orbit & atmosphere

P. Palma-Bifani[1,2], G. Chauvin[2,3], M. Bonnefoy[3], P. Rojo[1], S. Petrus[3], L. Rodet[4], M. Langlois[5], F. Allard[6], D. Homeier[6], B. Charnay[7] & C. Desgrange[3].

[1] Departamento de Astronomía, Universidad de Chile, Casilla 36-D, Santiago, Chile
[2] Unidad Mixta Internacional Franco-Chilena de Astronomía, CNRS/INSU UMI 3386 and Departamento de Astronomía, Universidad de Chile, Casilla 36-D, Santiago, Chile
[3] Univ. Grenoble Alpes, CNRS, IPAG, F-38000 Grenoble, France
[4] Cornell Center for Astrophysics and Planetary Science, Department of Astronomy, Cornell University, Ithaca, NY 14853, USA
[5] CRAL, UMR 5574, CNRS, Universit de Lyon, Ecole Normale Suprieure de Lyon, 46 Alle d'Italie, F-69364 Lyon Cedex 07, France
[6] Centre de Recherche Astrophysique de Lyon, UMR 5574: CNRS, Université de Lyon, École Normale Supérieure de Lyon, 46 allée d'Italie, 69364 Lyon Cedex 07, France
[7] LESIA, Observatoire de Paris, PSL Research University, CNRS, Sorbonne Universités, UPMC Univ. Paris 06, Univ. Paris Diderot, Sorbonne Paris Cité, 5 place Jules Janssen, 92195 Meudon, France

Abstract

Aims. We aim to investigate the formation pathway of the companion to AB Pic, one of the first companion ever imaged straggling the planet-brown-dwarf boundary.

Methods. We composed a spectrum merging an extensive observation set of: Archival medium-resolution ($R \sim 4000$) SINFONI data in the K-band (1.96 - 2.45 μm), which we reduced; literature J, H, and Lp bands spectra; and photometry points on visible and infrared wavelengths. We modeled the composed spectrum with ForMoSA, following a multi-modeling approach for two atmospheric grids (Exo-REM and BT-Settl13). In parallel, we modeled its orbit using literature NaCo photometric points from 2003 and 2004 and a new Sphere H band observation from 2015 with the OFTI tool.

Results. The orbital solutions confirm that the exoplanet AB Pic b is likely to be orbiting at a semi-major axis of 190^{+200}_{-50} au on a highly-inclined orbit but with a poorly constrained eccentricity. From the atmospheric modeling we derive a $T_{eff} = 1700 \pm 50$ K, $log(g) = 4.5 \pm 0.3$ dex, $[M/H] = 0.36 \pm 0.2$, $^C/_O = 0.58 \pm 0.08$, $1.7^{+0.8}_{-0.1}$ R_{jup} and $RV = 32.3 \pm 5$ km/s. These parameters depend on the wavelength interval used as input and the model's family and were derived using the Exo-REM models.

Conclusions. AB Pic b was most likely formed by Gravitational Instabilities or Gravoturbulent Fragmentation at early stages in a massive protoplanetary disk given its $^C/_O$ and current location. However, other scenarios like Core Accretion cannot be ruled out with our current system understanding. A measurement of the carbon isotopologues ratio, recently proposed as complementary formation tracers, and a high-resolution spectrum to constraint the eccentricity would be ideal to prove this story further.

3.1 Introduction

Transit, direct imaging, and cross-dispersed spectroscopy have successfully allowed us to describe the atmospheres of exoplanets. Since the first characterization of HD 209458 b, a hot Jupiter (Charbonneau, 2002), exoplanets revealed a broad diversity of physical processes at play. Direct imaging studies have mainly focused on young, self-luminous giant gaseous planets, not strongly irradiated and orbiting their host star at relatively large separations (> 1"), offering a very complementary view between transit and cross-dispersed studies of

Hot Jupiters and the classical spectroscopic characterization of young isolated planemos (or free-floating exoplanets) (Jameson et al., 2008; Allers and Liu, 2013). Emblematic systems such as HR 8799 (Marois et al., 2010), β Pictoris (Lagrange et al., 2019), HD 95086 (Rameau et al., 2013), HIP 65426 (Chauvin et al., 2017) or PDS 70 (Keppler et al., 2018) offer a rich opportunity to investigate the architectures of young solar-system analogs, but also the atmospheres of young super-Jupiters sometimes still accreting material (Haffert et al., 2019).

Today's planet imagers, such as SPHERE at VLT (Beuzit et al., 2019), GPI at Gemini (Macintosh et al., 2006) or SCExAO/CHARIS (Groff et al., 2015; Jovanovic et al., 2015), have yielded low-resolution ($R_\lambda = 30 - 90$) emission spectra and photometry of tens of exoplanets exhibiting broad unresolved molecular bands (H_2O, CH_4, VO, FeH, CO) in the near-infrared (NIR) ($0.95 - 2.45\,\mu m$). They can be compared to predictions of atmospheric models to infer first-order information on the physical properties, mainly effective temperature (T_{eff}), surface gravity ($log(g)$) and Luminosity ($log(L/L_\odot)$). However, they are lacking crucial information at higher resolution ($R_\lambda > 1000$) to enable a detailed exploration of fundamental parameters as metallicity ($[M/H]$), carbon to oxygen ratio ($^C/_O$) and the carbon isotopologues ratios ($^{12}C/^{13}C$). The present-day atmospheric composition might still be imprinted by the formation pathway, which is a novel way to classify the objects; therefore, the mentioned parameters are believed to be formation tracers (Nowak et al., 2020; Molliere and Snellen, 2019).

With high resolution, an exploration of exoplanets' rotational and radial velocities, connected to their spin and three-dimensional orbital properties (Snellen et al., 2014), becomes feasible. Currently, a minimal number of exoplanets have been characterized at high spectral resolution ($R_\lambda > 10000$), among them, β Pictoris b (Snellen et al., 2014), GQ Lupi b (Schwarz et al., 2016b), HR 8799 planets (Wang et al., 2021), and HD 106906 b (Bryan et al., 2021). The handful of young giant exoplanets at wide orbits offers unique benchmark laboratories to explore the spectral diversity together with formation and evolutionary scenarios by understanding their atmospheres, physical properties, and the system dynamics and stability in connection with the stellar host properties. Therefore, they are and will be prime targets for upcoming telescopes, such as the James Webb Space Telescope ($JWST$[1], first light 2021, GTO target), and the Extremely Large Telescope (ELT[2], first light 2027).

High and low-resolution observations offer very complementary constraints. In this line, medium resolution observations can partly isolate a rich set of molecular absorptions contained in a spectrum over usually a wide wavelength range allowing reasonable estimations for $log(g)$, $[M/H]$, $^C/_O$, and clouds. For example, adaptive-optics-fed integral-field spectrographs (IFS) operating at a spectral resolving power of $R_\lambda = 2000 - 5000$ in the NIR, such as SINFONI at VLT, NIFS at Gemini- North or OSIRIS at Keck, allowing to deepening the understanding of atmospheres. These observations are essential to prepare the models and theories for the upcoming generation of telescopes.

Regarding the prime targets, differentiating substellar objects known as brown dwarfs (BD) from massive Jupiter-like exoplanets is tricky since these populations overlap in observable properties. i/ If a substellar object ($< 30 M_{jup}$) is found isolated in space, it is identified as a BD (Nayakshin, 2017), and its chemical composition is not expected to differ from the

---

[1] https://jwst-docs.stsci.edu
[2] https://elt2020.web.ox.ac.uk

interstellar medium (ISM) (Chabrier et al., 2014). ii/ If the object is orbiting another star, we call it a companion, and it can either be an exoplanet or a BD binary. Currently, the most accepted formation theories for them are Gravoturbulent Fragmentation of molecular clouds (GtF) (Padoan and Nordlund, 2004), Core Accretion (CA) (Pollack et al., 1996), and Gravitational Instabilities (GI) (Boss, 1997). When these objects are young, their properties still relate to their formation environments, mainly to its location of formation and composition of the accreted material that leaves an imprint on the upper atmospheric layers (Madhusudhan, 2019).

Studying the atmospheres of young exoplanets and substellar companions is essential for unveiling their history, which is done by modeling their spectra. Atmospheric modeling can be approached from two techniques: Retrieval Methods (Lavie et al., 2017) and Forward Modelling (Petrus et al., 2019, 2021). For this project, we used Forward Modelling, an auto-consistent approach where pre-computed radiative transfer-based atmospheric models are compared to observations following stochastic methods. The models are parameterized by the key parameters that describe an atmosphere and are received as a grid. The main advantage of this approach is the significantly lower computational time. Different atmospheric grids are currently available, such as BT-SETTL13 (Allard et al., 2013) and Exo-REM (Charnay et al., 2021). The models' description is based on the opacity sources of the available molecules and their abundances. Apart, attempts to include clouds, hazes, winds, disequilibrium chemistry, and thermal inversions, among others, have been carried out to reproduce the rich set of emission and absorption lines observables. Today those models are succeeding in reproducing the atmospheric spectral features, but given the complexity of these systems, attempts to develop 3D models are being carried out nowadays, assuring to revolutionize the topic in the following years (Fortney et al., 2021).

In forward modeling, the models derive the fit from the fundamental atmospheric parameters, which currently are less than 5, being the classical ones the T_{eff}, $log(g)$, $[M/H]$ and $^C/_O$. The $^C/_O$ ratio is constant on the ISM, varying mainly due to the age of the universe (Chiappini et al., 2003) but it vary radially for gas and dust in protoplanetary disks triggered by the snow-lines (H_2O, CO_2 and CO) (Öberg et al., 2011). Massive planets formed by CA accrete their gaseous envelopes at the final formation stages, impacting the carbon and oxygen abundances (Madhusudhan, 2019), but a companion formed by GI or GtF is expected to have an ISM $^C/_O$ ratio. Therefore the $^C/_O$ ratio is proposed as a formation tracer. However, the formation analysis must consider migration mechanisms and accretion of solid at final formation stages, among others, to understand the evolution and dynamics of the systems.

Other complementary tracers have been proposed in the past years, for example, the ratio between the carbon monoxide isotopologues (Molliere and Snellen, 2019). In this line, on Zhang and Snellen (2021) they measured that a young isolated BD has a roughly ISM $^{12}CO/^{13}CO = 97^{+25}_{-18}$ while on Zhang et al. (2021) they studied TYC 8998, a wide orbit (150au) companion and report a $^{12}CO/^{13}CO = 31^{+17}_{-10}$ probably due to a significant accretion of ^{13}C enriched ice at its final formation stage. Together with the previous ideas, exoplanets usually have surface gravity values 100 to 1000 times smaller than BD, which affects the vertical mixing and gravitational settling of condensates in their atmospheres, probably leading to thicker cloud layers, upper atmosphere sub-micron hazes, and cloud opacities remaining down to T_{eff} of 600 K at early ages (Apai et al., 2013; Bonnefoy et al., 2014)

To land the presented ideas, we aim to investigate AB Pic b, a substellar companion to AB Pic, a young, ∼solar-type (K1V) star located at 50.14 ± 0.04 pc from the Sun, based on *Gaia* eDR3 (Gaia Collaboration et al., 2021). The star was recently re-classified as a part of the younger Carina association based on *Gaia* DR2 data by Booth et al. (2021) where an age of $13.3^{+1.1}_{-0.6}$ Myr was estimated. The 10 ± 1 M_{Jup} wide-orbit exoplanet located at 273 ± 2 au in projected separation was revealed by high-contrast coronographic images obtained with NaCo at VLT by Chauvin et al. (2005). Years ago, Bonnefoy et al. (2010, 2014) characterized the complete $1.1 - 2.5\,\mu m$ spectrum with medium spectral resolution SINFONI data at VLT. The presence of various atomic and molecular lines was identified, consistent with an L1±1 spectral type, $log(L/L_\odot) = -3.7 \pm 0.1$ dex, $T_{eff} = 1700 \pm 100$ K, and $log(g) = 4.0 \pm 0.5$ dex from atmospheric and evolutionary models.

This project's scope is to unveil the origins of AB Pic b to understand its BD/ exoplanet nature. The observations are described in Section 3.2 together with the data processing for the SPHERE 2015 photometric point and the reduction methods for the K-band spectrum. In Section 3.3 we present the orbital modeling performance, then in Section 3.4, the spectral analysis strategy and derive the best suited physical properties compared to evolutionary models. In Section 3.5 we analyze the performances and test formation scenarios, and the main conclusions are presented in Section 3.6.

3.2   Observations & Data Reduction

AB Pic b is a companion studied multiple times since its discovery by Chauvin et al. (2005). A rich set of literature observations are available on multiple wavelengths, among them: i/ photometry points on the visible $(0.53 - 0.92\,\mu m)$ taken by the Hubble Space Telescope HST/WFC3 (Bonnefoy et al., 2014), ii/ medium resolution SINFONI spectra $(R_\lambda = 1500 - 2000)$ on the J and H bands (Bonnefoy et al., 2014), iii/ Lp band spectrum $(R_\lambda \sim 300)$ from the Magellan-AO/CLIO2 telescope (Stone et al., 2016), and iv/ Spitzer IRAC photometry points at 3.6, 4.5, 5.8 and 8 μm published by Martinez and Kraus (2021). Mining into unpublished archived datasets, we found that medium resolution spectroscopic observations at K-band were obtained with SINFONI at VLT in December 2013 (program: 092.C-0809(A)) to complement the spectral information at J and H-bands described before. The system was also observed in 2015 with SPHERE at the VLT in the course of the SPHERE Guaranteed Time Observations (GTO program: 095.C-0298(H)) to explore the orbital properties of AB Pic b in combination with previous NaCo observations from 2003 and 2004 (Chauvin et al., 2005). Both new SINFONI and SPHERE observations are described below and drive this study.

3.2.1   SPHERE Observations & Data Processing

The AB Pic system was observed during the SpHere INfrared survey for Exoplanets (SHINE, Guaranteed Time Observations) on February 6th, 2015, using the VLT/SPHERE high-contrast instrument (Beuzit et al., 2019). The observations were obtained with the IRDIFS mode that combines the IRDIS (Dohlen et al., 2008) and IFS instruments (Claudi et al.,

2008) simultaneously. The IRDIFS-EXT model combines IRDIS in dual-band imaging (DBI Vigan et al., 2010) mode with the K1K2 filter doublet $\lambda_{K1} = 2.103 \pm 0.102$ μm, $\lambda_{K2} = 2.255 \pm 0.109$ μm, and IFS in the YJH (0.97–1.66 μm) setting. The IRDIFS mode combines IRDIS in DBI with H2H3 filters ($\lambda_{H2} = 1.593 \pm 0.055$ μm, $\lambda_{H3} = 1.667 \pm 0.056$ μm), and IFS in the YJ (0.95–1.35 μm) setting.

All IRDIS and IFS datasets were reduced using the SPHERE Data Reduction and Handling (DRH) automated pipeline (Pavlov et al., 2008) at the SPHERE Data Center (SPHERE-DC) to correct each datacube for bad pixels, dark current, flat field, and sky background. After combining all datacubes with an adequate calculation of the parallactic angle for each frame of the deep coronagraphic sequence, all frames are shifted at the position of the stellar centroid calculated from the initial star center position. To calibrate the IRDIS and IFS datasets for the sky emission, the astrometric field 47 Tuc was observed. The platescale and true north solution at each epoch is based on the long-term analysis of the GTO astrometric calibration described by (Maire et al., 2018). The rotation correction considered to align images to the

Figure 3.1: SPHERE-IRDIS coronagraphic image at H-band of AB Pic b relative to A reduced using SpeCal (Galicher et al., 2018).

detector vertical in pupil-tracking observations is -135.99 ± 0.11 deg. Anamorphism correction is obtained by stretching the image Y-direction with a factor of 1.0060 ± 0.0002. AB Pic b is only seen within the IRDIS field of view being located at more than 5.3 as (see Figure 3.1). Its relative position has been derived using the SpeCal pipeline (Galicher et al., 2018). The result is reported in Figure 3.3 together with the NaCo data points from (Chauvin et al., 2005). The astrometric measurements of AB Pic b used for the orbital fitting, relative to AB Pic A are reported on Table 3.1.
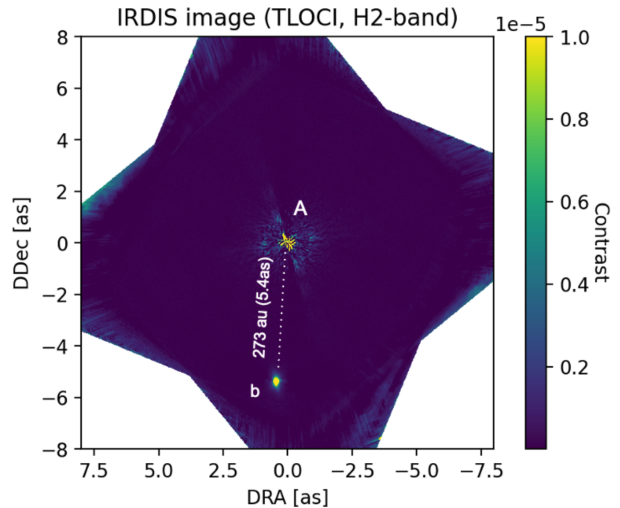
Table 3.1: Astrometric measurements of AB Pic b relative to AB Pic A

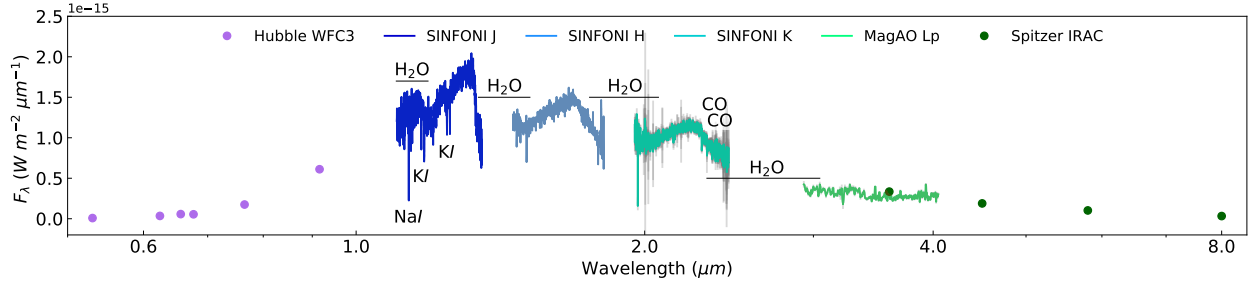| Telescope/Instrument	Epoch	Separation (mas)	P.A. (deg)
VLT/NaCo	2003.213	5460±14	175.33±0.18
VLT/NaCo	2004.180	5450±16	175.13±0.21
VLT/NaCo	2004.735	5450±14	175.30±0.20
VLT/SPHERE-IRDIS	2015.097	5398.7±4.5	175.26±0.13

Figure 3.2: In this figure, the complete available literature spectrum of AB Pic b is observable together with the reduced K-band spectrum from this work and the errors in grey. Distinctive atomic and molecular absorption lines are observable and we labeled the most relevant ones for this work.

3.2.2   SINFONI K-band Observations

AB Pic b was observed with SINFONI at the VLT on the 13 of December 2013 and the 1 of December 2014 (program $092.C - 0809$ (A); PI J. Patience). SINFONI was composed of a custom adaptive optics module (MACAO) and an IFS (SPIFFI). SPIFFI cuts the field-of-view into 32 horizontal slices (slitlets), which are re-aligned to form a pseudo-slit, and dispersed by a grating on a Hawaii 2RG ($2k \times 2k$) detector (Eisenhauer et al., 2003; Bonnet et al., 2004). The instrument was operated with pre-optics and a grating sampling of a 3" $\times$ 3" field of view with rectangular spaxels of 50×100 mas size, from 1.928 - 2.471 μm, at a spectral resolution $R_\lambda = \frac{\lambda}{\Delta \lambda} = 5090$ for this program. MACAO was used during the observations with a natural guide star (NGS) reference for the wave-front sensing. A sequence of 6 exposures of 300 s integration with five frames (ndit) each day, centered on the expected position of the planet, were performed.

3.2.3   SINFONI Cube Building & Spectral Extraction

We initially reduced the data with the ESO SINFONI data handling pipeline[3] v3.0.0 through the EsoReflex[4] environment. The pipeline use calibration frames to perform basic adjustments to the raw science frames and correct them from distortion. The slitlets position on the frames at each wavelength is identified before building a datacube for each exposure. Further corrections on top of the ESO reduction steps were performed, based on the *Toolkit for Exoplanet deTection and chaRacterization with IfS* (TExTRIS) (Petrus et al. 2021; Bonnefoy et al. in prep). A detailed explanation of these methods is given below.

i. As implemented by Petrus et al. (2021), the method identifies a constant wavelength shift using the telluric absorption lines. We corrected both, the companion and the telluric standard star (STD), from spaxels-to-spaxels wavelength shifts. The method does not include an uncertainty measurement on its current version, but our research

---

[3] https://www.eso.org/sci/software/pipelines/sinfoni
[4] www.eso.org/sci/software/esoreflex

group has observed discrepancies of $\sim 15km/s$ in the recalibration in wavelength for another target. From pixel to pixel, the uncertainties are expected to be insignificant.

ii. We checked that the light from AB Pic b was not contaminated by other emission sources, as the host star, and evaluated the position of AB Pic b and the STD in each respective cube. We measured the motion of a point source affected by atmospheric refraction and recovered the estimated source coordinates in each cube slice. We played by adjusting the polynomial fit degree and the initial guess for the expected position of the target. For the STD frames, we binned the cubes in wavelengths to reduce computation time. Different extraction radii centered at the source position were evaluated to find the optimal aperture. We found that the spectral slope, in general, does not change for increasing apertures, and the S/N seems higher for smaller apertures; thus, we set the aperture radius to 5 pixels. The error bars for each extracted spectrum are computed from the estimated one standard deviation level of the residuals around the circular aperture.

iii. The contamination by water bands of the earth atmosphere is recognizable in this preliminary spectrum, which is why a STD of spectral type B8V was observed together with AB Pic b. We got a spectrum of the atmospheric transmission for each night to correct this effect. We corrected the STD and target spectrum of each night from the dark spot effect of the detector known to affect the K-band data by fitting a one-dimensional polynomial from $2.14 - 2.15\mu m$. Next, we corrected the NIR Hydrogen (H) lines from the STD spectrum by fitting a Voigt profile. The function corrects for specific Paschen (Pa_β) and Brackett (Br_{16}, Br_{14}, Br_{12}, Br_{11}, Br_{10}, and Br_γ) series lines that may be observable on the NIR. We then visually inspected these corrections, and using the spectral type of the STD star, we computed its corresponding theoretical black-body spectrum. Each STD spectrum was corrected by dividing the computed black-body and recovering the atmospheric transmission spectrum of each night. Finally, each spectrum of AB Pic b was corrected by dividing the atmospheric transmission spectrum.

iv. We selected all high-quality spectra by making a visual inspection and mean-combined them, recovering a final spectrum for AB Pic b with the corresponding errors, that were computed by mean-combining the errors of each spectrum and dividing it by the root of the number of datacubes considered. Before merging, we applied a Doppler shift and Barycentric correction to account for the earth's motion.

We calibrated the extracted normalized spectrum in flux units for all bands individually, using the J, H, K, and Lp-band magnitude values reported in Table C.1. of Bonnefoy et al. (2014). The full spectral energy distribution (SED) for AB Pic b is observable in Figure 3.2 together with the errors in grey and the names of relevant absorption lines.

3.3 Orbital Properties

The combination of NaCo observations from March 2003, March 2004, September 2004 with SPHERE observations from February 2015 offers the time span to resolve the orbital motion of AB Pic b. The motion is mainly resolved in separation (nothing significant is observed in
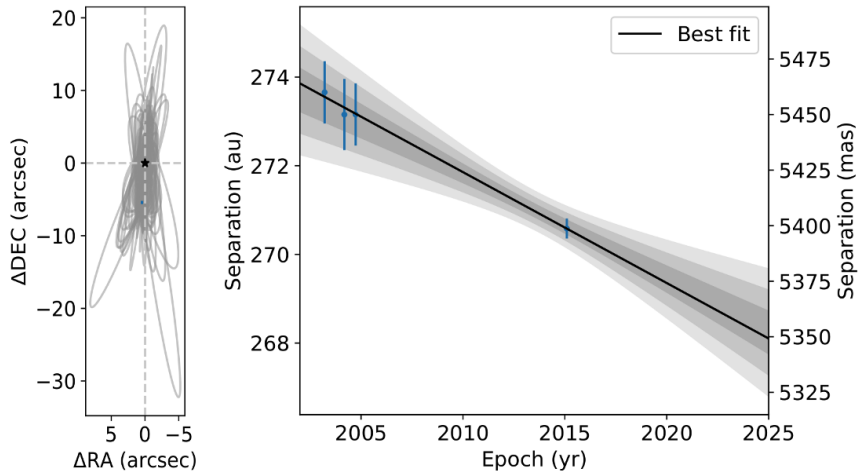
Figure 3.3: Orbital monitoring of AB Pic b combining NaCo and SPHERE observations. On the left panel, we observe that highly-inclined and moderate to highly-eccentric solutions are favored, and on the right panel, the main orbital variation is seen in separation for the relative positions between AB Pic b and the primary. The black represents the best orbital solution (lower χ^2).

position angle), which indicates a highly-inclined orbit for the planet. We used the *Orbits for the Impatient (OFTI)* tool, a Bayesian rejection sampling method for quickly fitting the orbits of long-period exoplanets (Blunt et al., 2017), to explore the orbital solutions of AB Pic b. We adopted the default priors detailed in the *orbitize!* python package (Blunt et al., 2020), with an upper bound of 1000 au for the semi-major axis. The orbital fitting results are directly compared to the observations in Figure 3.3 and detailed in Table 3.2. The corner plot of the orbital parameters is shown in Figure 3.4. The solutions confirm that the exoplanet AB Pic b is likely to be orbiting at a semi-major axis of 190^{+200}_{-50} au on a highly-inclined orbit ($i = 90 \pm 12$ deg), with a potentially moderate to high-eccentricity, although poorly constrained. As expected by the North-South orientation of the orbit, the longitude of ascending node (Ω) is close to 0 ± 180 deg.

Table 3.2: Orbital solutions of AB Pic b from OFTI and the NaCo and SPHERE relative astrometry.

Orbital parameter	MCMC solutions
a (au)	190^{+200}_{-50}
$inc.$ (°)	90 ± 12
Ω (°)	$-5 \pm 13 \ (\pm 180)$
t_p (yr AD)	2600^{+1700}_{-300}

The system configuration makes it very interesting for future high-precision radial velocity measurements as previously done with CRIRES for β Pic b, GQ Lupi b, and more recently with KPIC for HR 8799 bcde (Snellen et al., 2014; Schwarz et al., 2016a; Wang et al., 2021). In conjunction with NaCo and SPHERE relative astrometry, this would help to obtain the three-dimensional position and velocity of AB Pic b relative to A. Note that AB Pic A has a precise derived radial velocity (RV) of 22.65 ± 0.04 km/s (Soubiran et al., 2018).
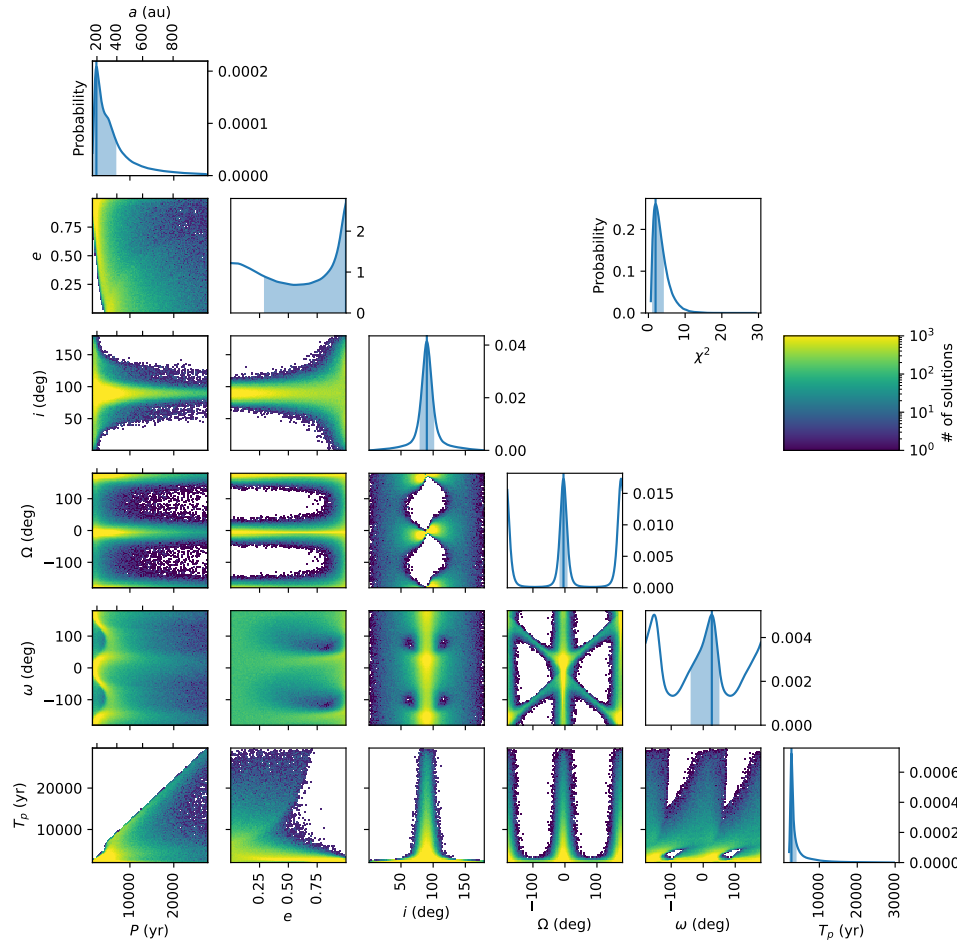
Figure 3.4: Corner plot representing the solutions of the orbital fit of AB Pic b combining NaCo and SPHERE observations. The blue vertical lines in the diagonal plots indicate the peak value, and the blue shaded areas indicate the shortest 68% confidence intervals.

3.4 Physical Properties

We followed two approaches to derive the atmospheric and related physical properties of AB Pic b. We first used ForMoSA, short for Forward Modeling tool for Spectral Analysis, presented and detailed in Petrus et al. (2019, 2021), for modeling the spectrum. For ForMoSA we implemented two different atmospheric models, the 2013 version of the BT-SETTL model grids exploring different $^C/_O$ ratio (Allard et al., 2013) and Exo-REM Charnay et al. (2021), to analyze their performance and limitations at deriving robust physical properties. Then we compared the derived physical properties with evolutionary models' predictions from BEX-Hottest-cond03 (Marleau et al., 2019) to check consistency for the derived parameters.
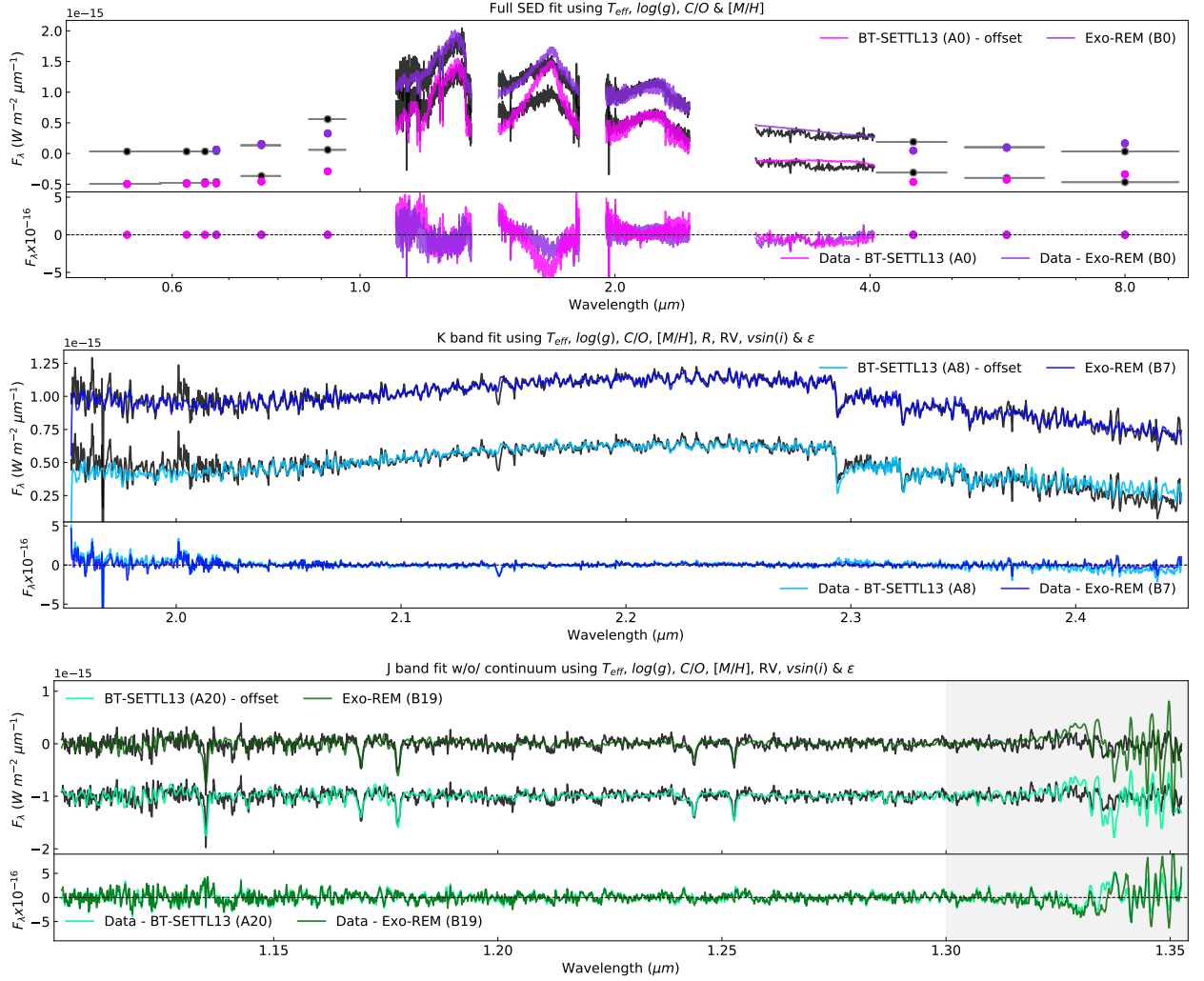
Figure 3.5: Top panel: The full SED fitting for both families of atmospheric models, with an offset applied to the BT-SETTL13 model and the residuals, computed as data - model. Middle panel: Same as the top panel but for the K band. Lower panel: Same as the top panel, but for the J band, the gray area starting at 1.3 μm stands for the spectral region excluded from the fit due to the H_2O noisy behavior. Each model is identified on the label with the numeration on Tables 3.4 and 3.5. The posteriors values for the reported models are observables on the corner-plots on Figures 3.6 and 3.7. The colors have consistency for each model shown in the spectrum figures, the corner plots, and the tables.

3.4.1 Atmospheric Models

ForMoSA is a tool based on a forward-modeling approach that compares observations with grids of pre-computed synthetic atmospheric models using Bayesian inference methods. It relies on a Nested Sampling algorithm (Skilling, 2006) to determine the posterior distribution function (PDF) of a set of free parameters. This method performs a global exploration to look for local maxima of likelihoods following an iterative method that isolates a progressively restrained area of the same likelihood while converging toward the maximum values. It avoids missing local maxima of likelihood since it evaluates the Bayesian evidence used for

performing model selection (Trotta, 2008). ForMoSA generates synthetic spectra at each step of the Nested Sampling using linear interpolation of the spectra from the original model grid. The errors given by ForMoSA are statistical and have been determined for each parameter as the range which encompasses one sigma assuming Gaussian distributions, and they do not include possible systematic errors in the models (Petrus et al., 2021).

ForMoSA allows the user to fit the atmospheric grid for, in general, T_{eff} and $log(g)$, and depending on the model $[M/H]$ and $^C/_O$ ratio may be included, among others. Spectra can be affected by other physical processes like the Doppler shift due to the orbital rotation and the broadening of the lines due to the planet's spin. Therefore, ForMoSA allows fitting the radius of the planet (R), the extinction coefficient (A_v), the radial velocity (RV), the rotational velocity ($vsin(i)$), and the limb-darkening (ε). By including these five parameters, the models are modified before being compared to the observations. The allowed ranges to explore solutions that we considered are listed in the first row of Table 3.4 for BT-SETTL13 and Table 3.5 for Exo-REM. We allow a limb-darkening parameter exploration in ForMoSA from 0.01 to 0.99 every time we included the $vsin(i)$ on the models but we exclude its posteriors from the Tables 3.4 and 3.5 due to its flat distributions, observables in the corner plots of Figures 3.6 and 3.7 labeled as ε.

BT-SETTL 2013

Since the BT-SETTL13 models were already described in the introduction of this document, here we will give only extra details. The grid we used provides spectra from 0.3 to 15 μm and considers T_{eff} from 1400 to 2200 K, $log(g)$ from 3.5 to 5.0 dex, $^C/_O$ ratio from 0.2754 to 1.096, and a constant solar metallicity ($[M/H] = 0.0$). The posteriors, obtained by using 500 living points, can be found in Table 3.4. We tested different setups, as described below:

i. Whole SED (J, H, K, and L bands with and without photometry points). This fit provides a reliable T_{eff} estimation since a broader spectrum range is fitted, making visible the bb behavior of the object.

ii. K band. A good fit of the CO bandheads observables in this band is expected to derive a good estimated value for the $^C/_O$ ratio. We tried fitting different extra parameters and subtracting the continuum by computing a low-resolution spectrum (R$\sim$ 100) and subtracting it from the observations and models.

iii. J band. This band has the KI lines that have great potential to derive a reliable $log(g)$ estimation as studied by Simon Petrus in his PhD project. Due to the H_2O bands from 1.3 to 1.55 μm, we restricted the wavelength range for the Nested Sampling up to 1.3 μm. As for the K band, we tried different fittings and subtracting the continuum.

iv. H and Lp bands. We modeled the spectrum with the continuum for these bands, but it was mainly an exploratory exercise, given the Lp band low resolution and the poor H band fitting from the full SED.

Three examples out of the multiple models we tested are observables on Figure 3.5 under the labels A0, A8, and A20, for the full SED, K band with continuum, and J band without
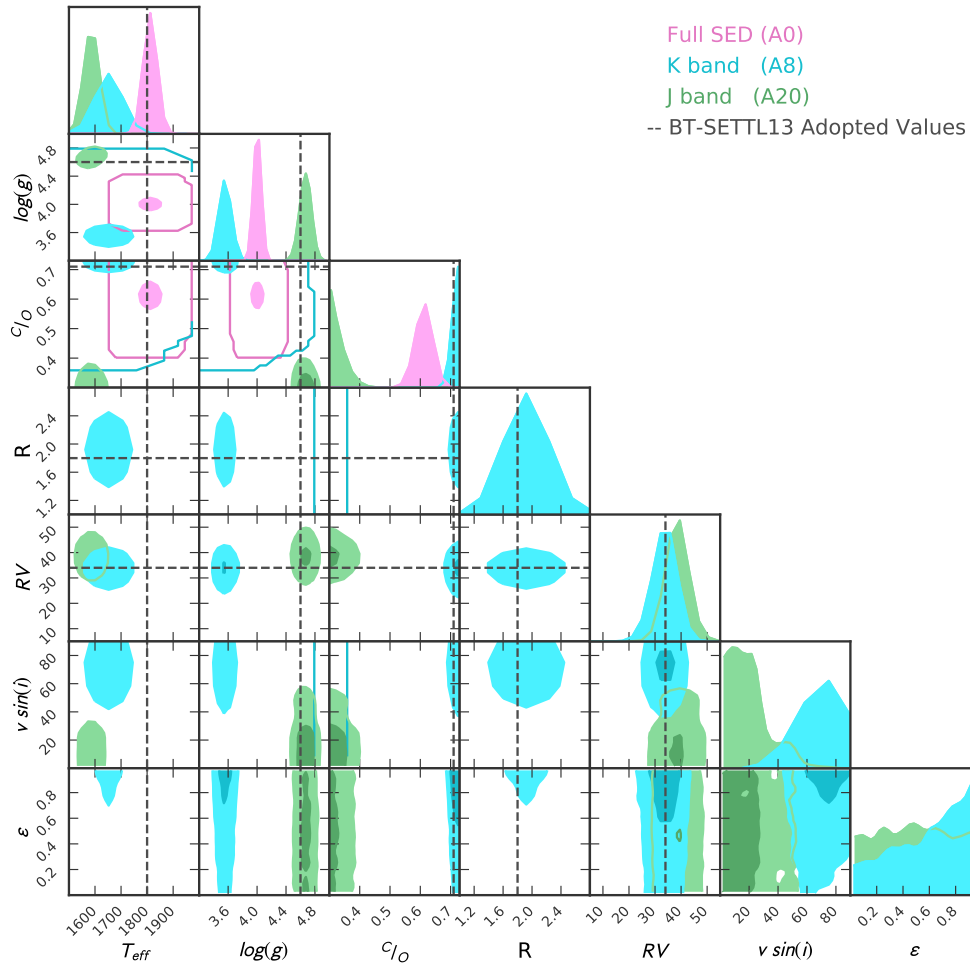
Figure 3.6: Corner plot comparing the models presented on Figure 3.5 for BT-SETTL13 with consistent colors. The black dashed lines show the adopted values from this work listed in the last row of Table 3.4.

continuum, respectively. The posteriors distributions of the selected models are observables on Figure 3.6 together with the adopted values as dashed black lines that were selected following the arguments described in the setup and are listed in the last row of Table 3.4.

Exo-REM 2021

Since the Exo-REM models were already described in the introduction of this document, here we will give only extra details. This grid provides spectra from 0.6667 to 251.6 μm and includes four free parameters: T_{eff} from 400 to 2000 K, $log(g)$ from 3.0 to 5.0 dex, $^C/_O$ ratio from 0.1 to 0.8, and $[M/H]$ from -0.5 to 1.0. For deriving the physical properties, we followed the same approach as for BT-SETTL13, and the posteriors and adopted values are reported in Table 3.5. Three examples from this atmospheric models are observables on Figure 3.5 under the labels B0, B7, and B19, for the full SED, K band with continuum, and J band without continuum, respectively. The posteriors distributions of the same three selected models are observables on Figure 3.7 together with the adopted values as dashed
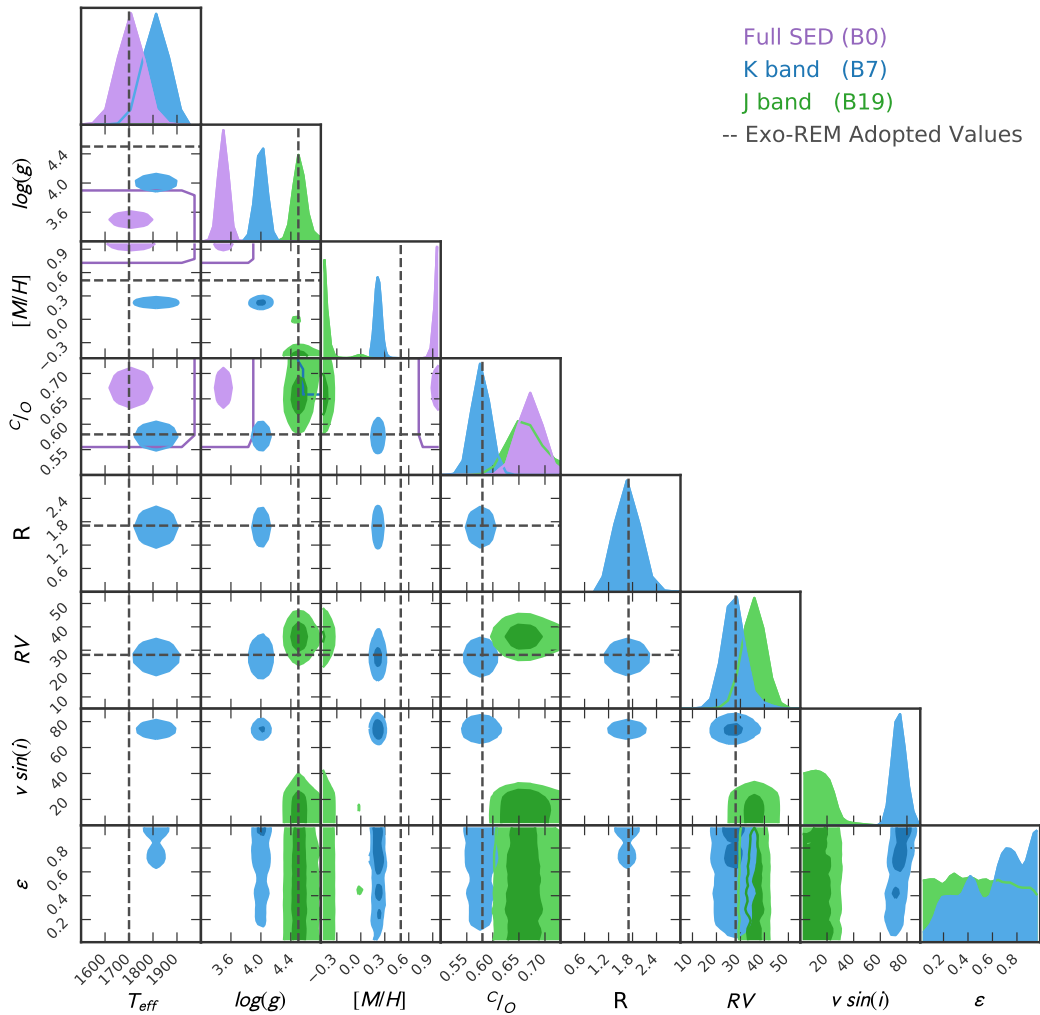
47

Figure 3.7: Same as Figure 3.6 but for Exo-REM with the models reported on Table 3.5.

black lines, selected in the same way as for BT-SETTL13 and listed in the last row of Table 3.5.

3.4.2 Evolutionary Models

As a first estimation of the physical properties of AB Pic b, we decided to compare it to evolutionary models of substellar objects. We show in Figure 3.8 the evolutionary tracks of the BEX-Hottest-cond03 models (Marleau et al., 2019). From the age of $13.3^{+1.1}_{-0.6}$ Myr provided by Booth et al. (2021) and the NaCo J, H and K magnitudes we estimated the predicted surface gravity and radius of AB Pic b and reported the values in Table 3.3. The derived values are consistent with the previously reported properties from Bonnefoy et al. (2014). An inconvenience of deriving physical attributes from evolutionary models is that these objects are known to be in-homogeneous in observable properties and, for example, clouds can impact the luminosity and, therefore, other estimated parameters. The evolutionary tracks as a function of R, $log(g)$, age, and T_{eff} together with the NaCo

prediction points and the ForMoSA adopted values from this work for each atmospheric grid are graphically observable in Figure 3.8. Special environment conditions can directly impact an object's observable features; therefore, to derive robust properties, atmospheric modeling is a reliable approach to follow. Therefore, we report on the evolutionary models Figure 3.8 the ForMoSA adopted values for the physical properties of AB Pic b from both families.

Table 3.3: AB Pic b predictions from BEX-Hottest-cond03 models for the calibrated absolute magnitudes on the J, H and K bands.

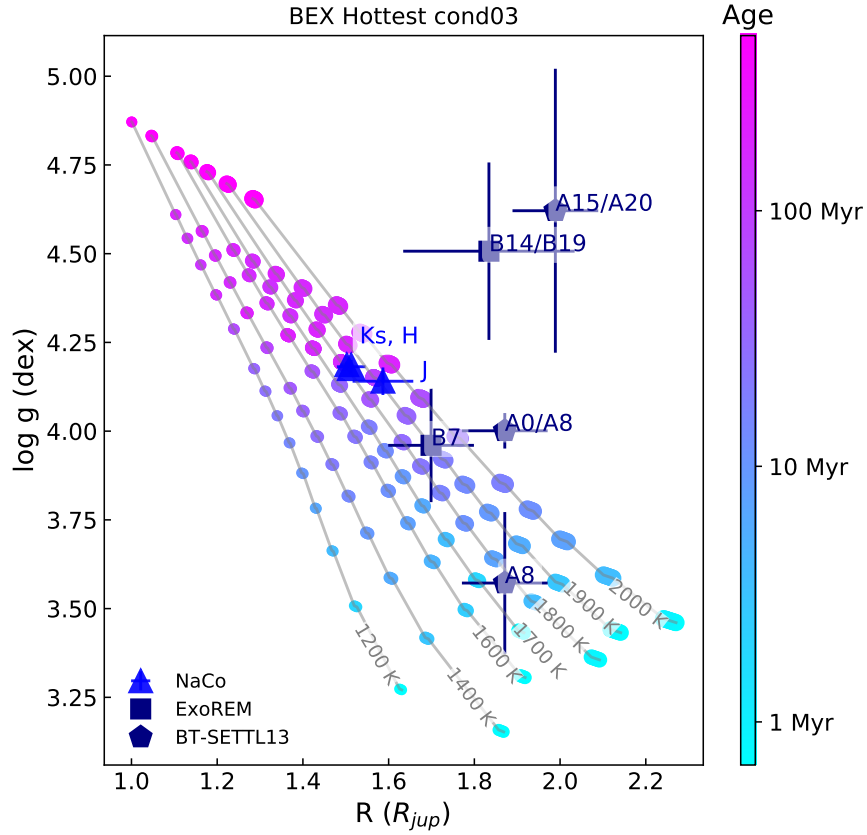| Band	Magnitude	R (R_{jup})	$log(g)$ (dex)	T_{eff} (K)
J	12.27 ± 0.36	1.57 ± 0.07	4.14 ± 0.04	1914 ± 75
H	11.38 ± 0.18	1.51 ± 0.03	4.18 ± 0.02	1833 ± 45
K	10.59 ± 0.07	1.50 ± 0.02	4.19 ± 0.01	1820 ± 21

Figure 3.8: In this Figure, the radius vs. gravity as a function of age and effective temperature from the BEX cond03 Hottest evolutionary models is presented. The color scale traces the ages on a logarithmic scale, and the iso-temperature curves are labeled. The estimated position in the diagram for AB Pic b is observed for i/ evolutionary models prediction using the absolute magnitudes from NaCo in the J, H, and K band reported by Chauvin et al. (2005) (blue colors) and ii/ The ForMoSA predictions from the adopted values of this work for both families of models.

49

3.4.3 Final Atmospheric Properties

Regarding the derivation of the reported physical and chemical properties of AB Pic b, in general, both atmospheric grids performed well, but a careful look into each parameter is essential given the multi-modeling approach we followed. For the T_{eff}, the full SED models are expected to derive the most consistent values. In this line, from BT-SETTL13 we adopted a $T_{eff} = 1800 \pm 20$ K while from Exo-REM a $T_{eff} = 1700 \pm 50$ K. Those T_{eff} where selected from the full SED models A0 and B0. BT-SETTL13 prediction is closer to the evolutionary models, but both values are consistent with the reported T_{eff} by Bonnefoy et al. (2014).

When we zoom-in into the CO bandheads region in the K band (see Figure 3.9), we observe that the model B7, with a $^C/_O = 0.58 \pm 0.08$, matches the data exquisitely while a model where a higher $^C/_O$ ratio was derived is over-fitting the CO lines. When we applied the nested sampling over the grid intrinsic parameters only (T_{eff}, $log(g)$, $^C/_O$, and $[M/H]$), the derived $^C/_O$ ratio is higher than when we include the R, RV, $vsin(i)$ and limb darkening (see Table 3.5), expected since we allowed corrections due to Doppler shift and rotational line broadening. In general, the spectrum from the models with a stellar $^C/_O$ ratio are in better agreement with the data, but the Exo-REM K band model derives a more precise prediction of the continuum shape (see model B7 on the middle panel in Figure 3.5 compared to model A8). Thus, we report a $^C/_O$ ratio of 0.58 ± 0.08.
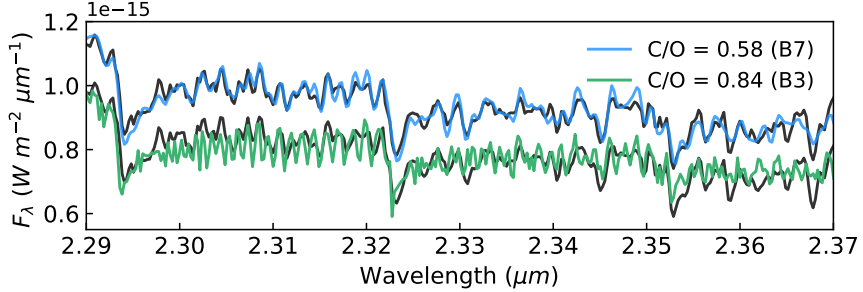

Figure 3.9: Comparison of the CO bandheads models performance by Exo-REM for two different set of free parameters, labeled accordingly to Table 3.5 and their $^C/_O$ ratio value.

As mentioned, it has been proven that the KI lines in the J band are good tracers of the $log(g)$. However, we observe that both models presented difficulties in performing a good fit of the J band continuum, probably due to H_2O in the atmosphere. For BT-SETTL13, the models in the J band without the continuum derive $log(g) = 4.6^{+0.1}_{-0.5}$, which is slightly higher than the evolutionary models' predictions and the reported value from Bonnefoy et al. (2014). However, the K band models derive a lower value of $3.5^{+0.3}_{-0.1}$. Concerning the J band and specifically the KI lines, this overestimated $log(g)$ is a global problem encountered by Petrus et al. (in prep). A possible explanation is that the BT-SETTL13 model incorrectly reproduces the profile of the KI lines. The Exo-REM models exhibit the same continuum J band issues. However, since this family of models allows for a $[M/H]$ exploration, the posteriors are slightly harder to interpret. Actually, from the J band without continuum we derive $[M/H] \sim -0.36$ for high $log(g) \sim 4.5$ dex. These outcomes appear to be highly doubtful physically. When analyzing these parameters on the K band models we observe an anti-correlation between $log(g)$ and $[M/H]$ with possible solutions being $[M/H] \sim 0.36$ and

$log(g) \sim 4.0 \, dex$ or $[M/H] \sim 0.8$ and $log(g) \sim 3.3 \, dex$. By comparing with the evolutionary models, we observe that the most consistent results are the ones with lower $[M/H]$ and higher $log(g)$ therefore our adopted values are, for BT-SETTL13 $log(g) = 4.6^{+0.1}_{-0.5} \, dex$, and for Exo-REM $[M/H] = 0.36 \pm 0.2$ and $log(g) = 4.5 \pm 0.3 \, dex$. The $[M/H]$ is not a parameter we can rely on because it is probably biased by the other parameters, for example, the overall shape and flux calibration of the SED.

For both atmospheric grids, the K band with continuum derived the most confident radius posterior, being 1.8 ± 0.2 for BT-SETTL13 and $1.7^{+0.8}_{-0.1}$ for Exo-REM. We rely on the estimation of this setup since here, the modeled spectrum better fits all the spectral features, as observable in Figure 3.5. This value is slightly higher than the reported by Bonnefoy et al. (2014) of $1.4 \pm 0.3 \, R_{jup}$, and the evolutionary models' predictions but within the error bars. The reason behind our bigger radius could be a degeneracy with another parameter, like the T_{eff}, or an incorrect prediction of the emergent flux by the models.

For the RV, we report a value of 32.9 ± 10 with BT-SETTL13 and of 32.3 ± 5 with Exo-REM, obtained by averaging the K band without continuum posteriors and considering the confidence intervals. This value is derived from the K band models since this band was re-calibrated in wavelength, necessary for a reliable outcome, and the others have a lower spectral resolution. Uncertainties up to $15 \, km/s$ are expected, coming from the recalibration in wavelength. With high-resolution data, we could constrain the RV precisely, allowing us to confirm that AB Pic b is physically bound to AB Pic A. The $vsin(i)$ and limb darkening parameters have erratic behavior, and we do not report any values since the other parameters' uncertainties probably bias them. Finally, for the A_v, we see very different behaviors, but it was reported to be relatively low ($A_v \sim 0.2$) by Bonnefoy et al. (2014). This parameter is expected to redshift the observations due to interstellar dust. However, given the systematics on narrow wavelength windows, it is expected to be physically consistent for a broad wavelength range exploration, and since AB Pic b is close to the solar system ($d = 50.1 \, pc$), we did not explore it widely.

Given all the arguments exposed above where we visit all the models' outcomes, our finally reported values for the physical and chemical properties of AB Pic b are reported on the final columns of Tables 3.4 and 3.5.

3.5 Discussion

3.5.1 Performances & Limitations

As presented, we followed a multi-modeling approach varying the number of free parameters and the wavelength range to derive the physical and chemical properties of AB Pic b. In general, we observe that the derived posteriors are consistent with previously reported properties by Bonnefoy et al. (2014), but we recognized different behaviors for different setups. Therefore, here we will analyze the performances for the different wavelength ranges.

For the full SED, a good general agreement with the continuum shape of the observations

was derived for both atmospheric models, except for the H band range (see top panel of Figure 3.5). This overestimation of the H band flux, mainly from BT-SETTL13, is a known issue reported by Bonnefoy et al. (2014). The L band fitting in this setup agrees more or less with the continuum, but we do not observe any line fitting due to the low resolution on this spectrum. We observe that the inclusion of the photometry points was a significant improvement to recognizing the overall behavior of the SED, but for the models, they do not have a substantial impact on the derived physical properties.

We observe an excellent agreement between models and observations for the K band, especially with the Exo-REM grid, when including the R, RV, $vsin(i)$, and limb darkening into the fit (see model B7 in Figure 3.9). The reduced χ^2 value for model B7 is 0.00146, which is half the value of model B3 ($\chi^2 = 0.00235$) and BT-SETTL13's A8 model ($\chi^2 = 0.00231$). From the residuals on the middle panel of Figure 3.5 we recognize that the models have difficulties fitting the data where H_2O absorptions are present (up to 2.05 μm for both grids and beyond 2.4 μm for BT-SETTL13) and at 2.149 μm but this line is probably a remaining artifact caused by the dark spot on the instrument detector. We generally observe an overall good performance of the models for this band, and the reported issues are minor.

When modeling the J band only, we discovered that the quality of the spectra did not allow us to retrieve a good fit, which was reported by Bonnefoy et al. (2014) too. The problem of the continuum fitting probably arises due to the presence of the H_2O bands' that are difficult to model, or there may be some physical processes not considered by the models. We overcame it by subtracting the continuum to the observations and restricting the nested sampling exploration to 1.3 μm. On the lower panel of Figure 3.5 we observe how the $K\,I$ and $Na\,I$ lines are successfully fitted. However, in general, the models on the J band performed worse than on the K band.

Given the previous discussions and arguments, we do not better constrain the T_{eff}, $log(g)$, and R than previous works. We do have estimated the $^C/_O$ ratio and the $[M/H]$ which are new reported physical properties for AB Pic b, and are fundamental for unveiling the origins. Regarding the RV, high-resolution data is crucial for precisely estimating it, although we get consistent solutions compared to the host star. The $vsin(i)$, limb darkening, and A_v are poorly constrained from our multi-modeling approach. Finally, in general, we observe that the BT-SETTL13 models are less accurate in fitting the continuum and the individual lines than the Exo-REM ones. Testing other families of atmospheric models could be crucial for a broader comparison and better understanding of the scopes and limitations of the models.

From the orbital modeling, we derived the system's inclination, but we lack information to estimate the eccentricity of the system, which is crucial for the semi-mayor axis and period derivation. High-resolution data are needed to further constraint the orbital properties. In this line, the system face-on configuration is favorable for future high-precision radial velocity measurements as previously done with CRIRES for β Pic b and GQ Lupi b. The planet spin axis orientation and the rotational period could be reported from future CRIRES+, JWST, or ELT observations. The spin result could also be compared to the values measured for BD, exoplanets, and Solar System planets, providing knowledge on the initial angular momentum gained at formation.

All together, AB Pic b is a prime target for observations with the next generation of telescopes.

Therefore we show in Figure 3.10 how its spectrum would look like if observed with the different cameras of JWST. The incredible wide wavelength range, covering many molecular and atomic lines, is ideally suited for atmospheric modeling follow-up, eccentricity, and spin calculations and testing the future generation of models with this classical young, wide-orbit companion.

As complementary comments connecting the orbital modeling with the atmospheric modeling, a precise measurement of the RV of AB Pic b could allow confirming that the planet is physically bound to AB Pic A by a direct comparison of the projected velocity of the companion with the system escape velocity (2.80.2 km/s using a separation of 272 au and a mass of $1.3 \, \mathrm{M_\odot}$). High-resolution observations would allow an accurate derivation of the planet's orbital parameters and particularly its eccentricity. Moreover, we could directly measure the object's projected rotational velocity from the line width to explore the planet's spin axis orientation (favorable orientation if edge-on) and the rotational period of AB Pic b. The spin result also provides knowledge on the initial angular momentum gained at formation (Bryan et al., 2021). Currently, we are limited by the quality of the observations to follow up on these constraints.

3.5.2 Formation Pathways of AB Pic b

AB Pic b is orbiting at a wide separation from the host star, making the link to a formation process slightly tricky. First, its location is too far away to be explained directly by a CA scenario (Chabrier et al., 2014; Testi et al., 2014), where migration mechanisms would be essential (Marleau et al., 2019). Second, a formation through the GI scenario (Paardekooper and Johansen, 2018) explains the current location better, but it would require that the protoplanetary disk surrounding the host star was very massive at early stages. Last, a BD formation through Gravoturbulent Fragmentation in the molecular cloud could be feasible as well (Luhman, 2012; Chabrier et al., 2014; Nayakshin, 2017).

We recognized that from the BEX-Hottest-cond03 evolutionary models, the $log(g)$ and T_{eff} are slightly overestimated compared to atmospheric models, probably indicating that the formation process of AB Pic b was less like a star and more like a planet (Petrus et al., 2021). From the metallicity, we cannot drive any conclusions given the considerable uncertainties and potential biased, but it would be exciting in the future to compare the measurement with the host star value ($[M/H] = 0.04 \pm 0.02$, Swastik et al. (2021)). However, the [M/H] we derived is slightly higher than the host star value, favoring a formation scenario where AB Pic b formed after AB Pic at large separations, but more precise information is needed to confirm or reject these ideas.

In the same line, even though there is no available measurement for the $^C/_O$ ratio of AB Pic, the $^C/_O$ ratio for AB Pic b is compatible with the solar value ($^C/_O = 0.55$, Brewer and Fischer (2016)), considering that it is a younger object (Chiappini et al., 2003). Apart, this value is higher than the measurements for β Pictoris b and $HIP\,65426\,b$. β Pictoris b has a $^C/_O = 0.43 \pm 0.05$ and given its location and likely-hood of accreted solids mass, CA between the H_2O and CO_2 is the most likely formation scenario, as described by Nowak et al. (2020). $HIP\,65426\,b$ has a reported upper limit of $^C/_O \leq 0.55$ and it is proposed to be formed through
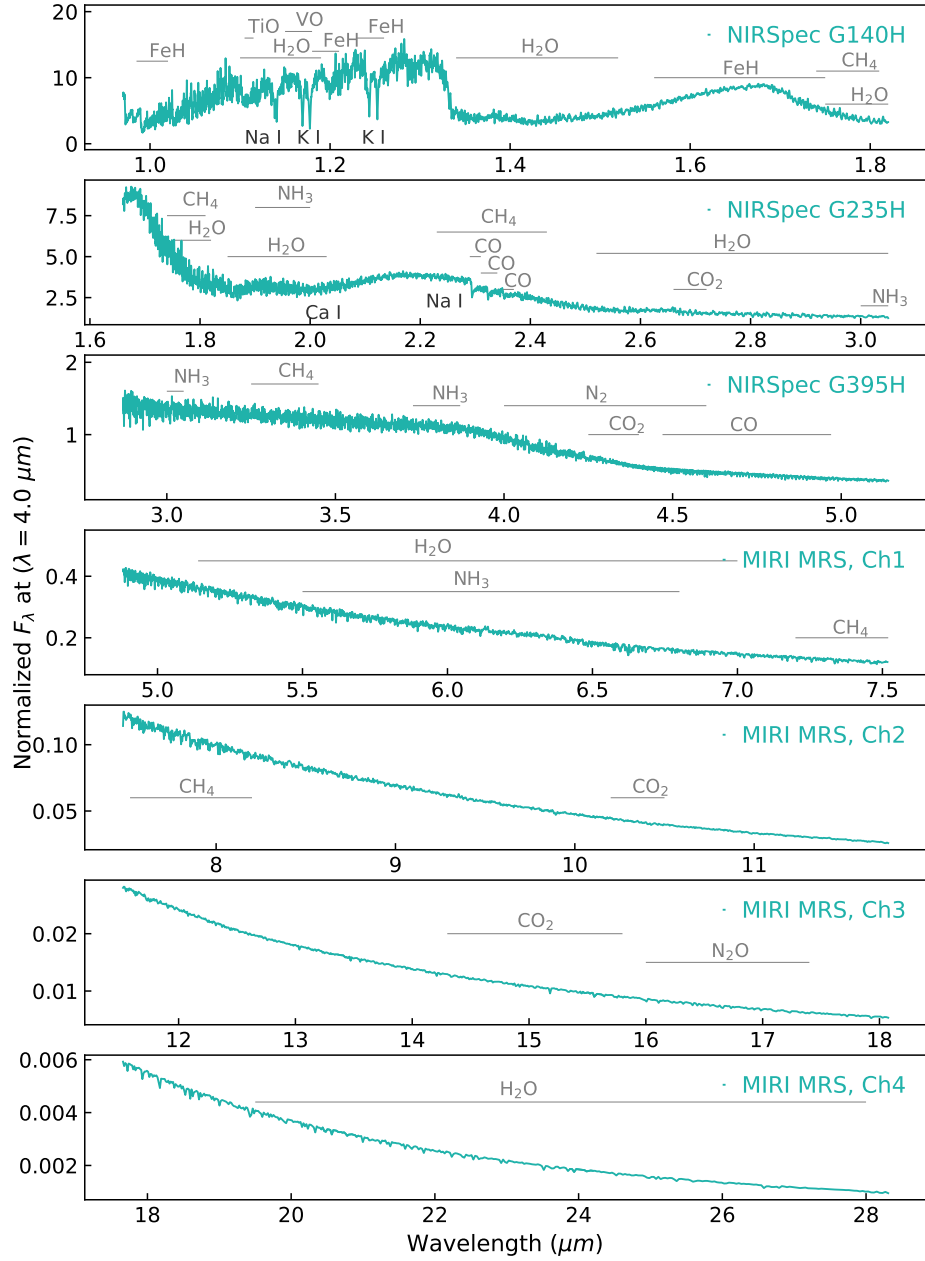
Figure 3.10: JWST NIRSpec and MIRI predictions from Exo-REM with $T_{eff} = 1800$, $log(g) = 4.5$, $[M/H] = 0.22$ and $^C/_O = 0.6$.

CA as well by Petrus et al. (2021) given its similarity to β Pictoris b. We can interpret the $^C/_O = 0.6$ for AB Pic b as an ISM $^C/_O$ value. AB Pic b could have been formed: i/ beyond the CO snowline since there is no clear enrichment in abundance on any of these two atoms on the atmosphere, compared to the ISM, in this case, it could have formed by GI, CA or even by Gravoturbulent Fragmentation ii/ inside the H_2O snowline and been ejected to wider orbits which are in better agreement with the timescales in the CA scenario, iii/ somewhere in between and have lowered its $^C/_O$ ratio by the accretion of solids at final formation stages but this is hard to test, following the ideas of Madhusudhan (2012).

We cannot rule out a formation scenario through CA, but there are two main difficulties

to overcome. A migration case where the planet got ejected to wider orbits is challenging to test, but a high eccentricity could be an observable tracer of such an event. However, as observable form Figure 3.4, our current information does not allow us to constraint its eccentricity, In any case, for just in a small number of configurations, AB Pic b would end up at a wide and eccentric orbit and not ejected from the system as studied for a similar system in Marleau et al. (2019) which make this scenario unlikely. High-resolution data is needed to test this scenario further. Therefore we consider that a GI formation better explains the current characteristics of AB Pic b. It allows a straightforward explanation of its current location, metallicity, and $^C/_O$ ratio without too many extra ingredients. A formation following the Tidal Downsizing Hypothesis proposed by Nayakshin (2017) could successfully explain the physical and chemical characteristics of AB Pic b as well.

Finally, AB Pic b is, in fact, very similar in physical and chemical characteristics to TYC 8998; therefore, measuring the $^{12}CO/^{13}CO$ ratio as done by Zhang et al. (2021) is a direct next step we are planning to follow, being able to deeper understand the location of formation of AB Pic b favoring with precise arguments a closer in or an in-situ formation.

3.6   Summary & Conclusions

In this project, we deeply characterized the giant planet/ BD boundary companion, AB Pic b. For it, we reduced and corrected archival K band SINFONI data and a SPHERE H-band imaged and collected available literature spectra and photometric points on other wavelengths. Altogether, this gives a unique set of observations covering a broad range of the SED. The definitive conclusions are the following:

  i. We compiled a rich set of literature data of AB Pic b from which the broad features of the SED are observable together with key molecular signatures (see Figure 3.2). From the photometric points, we have a time interval enough to partially resolve the orbital properties (see Figure 3.3).

 ii. In general, the multi-modeling performance allowed an excellent derivation of the physical properties compatible with literature and evolutionary models, when available, and we report first estimations for the $^C/_O$ ratio of the system and the $[M/H]$.

iii. We emphasize that the Exo-REM model B7 fits extremely nicely the K band continuum shape, lines, and especially the CO bandheads, making our estimation of $^C/_O = 0.58 \pm 0.08$ highly reliable.

 iv. From the orbital modeling, we report new values for the semi-major axis ($a = 190 \pm 200$ au), the inclination ($i = 90 \pm 12$ deg) talking in favor of an edge-on configuration of the system, and a potentially moderate to high-eccentricity, although poorly constrained.

  v. We suggest that AB Pic b was likely formed through gravitational instabilities or core/ pebble accretion beyond the CO snow line, given its current location, $^C/_O$ ratio, and the $[M/H]$. However, the scenario is highly complex, and our uncertainties on some properties are considerable. Therefore, we cannot rule out other mechanisms like gravoturbulent fragmentation or scattering.

We are looking to test further the formation history of this target, for which high-resolution data would be ideally, together with the comparison of the $^C/_O$ ratio to similar objects and the implementation of other atmospheric grids such as Drift-PHOENIX (Witte et al., 2009, 2011). Finally, a derivation of the $^{12}CO/^{13}CO$ isotopologues ratio on the atmosphere of AB Pic b and the measurement of the eccentricity could provide a key puzzle piece to unveil its formation history.

3.7 Final Comments & Future Perspectives

Finally, to recapitulate, AB Pic b is a classical substellar companion at a wide orbit, which has waken the curiosity of many astronomers; therefore, today, a rich set of observations are available from which the black-body behavior of its SED is visible. A deep understanding of this target opens the doors for a systematic analysis of similar sources and prepares the tools and theories for the upcoming generation of telescopes.

We are looking forward to the next steps of this project which are, first, publishing the current work, and second, we aim to have high-resolution ($R \sim 10.000$) AB Pic b observations, ideally suited for understanding the K band features further and allowing a measurement of the eccentricity of its orbit. Apart, to test the formation history further, we aim to constrain the $^{12}CO/^{13}CO$ isotopologues ratio, which should be possible with the current resolution, but we are still lacking the inclusion of this parameter in the models we implemented. Apart, a spectrum of the host star would be ideal, from which we would be able to measure its $^C/_O$ ratio and directly compare AB Pic b to its host star.

BT-SETTL 13		T_{eff}	$log(g)$	$^C/_O$	R	A_v	RV	$vsin(i)$
		(K)	(dex)		(R_{jup})	mag	(kms^{-1})	(kms^{-1})
Priors		$(1400-2200)$	$(3.5-5)$	$(0.28-1.09)$	$(0.5-10)$	$(0-5)$	$(-10-100)$	$(0-100)$
Full SED	A0	$1804.787^{+19.77}_{-4.388}$	$4.001^{+0.139}_{-0.02}$	$0.606^{+0.031}_{-0.034}$				
	A1	$1805.714^{+187.925}_{-3.164}$	$4.0^{+0.051}_{-0.055}$	$0.606^{+0.042}_{-0.023}$		$0.014^{+2.688}_{-0.014}$		
$JHKL_p$	A2	$1821.446^{+13.721}_{-13.18}$	$4.7^{+0.061}_{-0.382}$	$0.502^{+0.093}_{-0.021}$				
K band	A3	$1657.225^{+18.755}_{-63.579}$	$3.538^{+0.318}_{-0.079}$	$0.739^{+0.028}_{-0.152}$				
w/ cont	A4	$1658.289^{+79.733}_{-44.889}$	$3.612^{+0.59}_{-0.096}$	$0.74^{+0.03}_{-0.159}$	$1.926^{+0.122}_{-0.216}$			
	A5	$1664.624^{+16.482}_{-40.804}$	$3.549^{+0.243}_{-0.082}$	$0.73^{+0.026}_{-0.121}$			$22.319^{+23.09}_{-3.754}$	
	A6	$1670.387^{+17.975}_{-25.529}$	$3.571^{+0.214}_{-0.081}$	$0.72^{+0.026}_{-0.093}$			$34.342^{+17.35}_{-11.072}$	$71.975^{+127.808}_{-13.155}$
	A7	$1670.375^{+14.068}_{-20.239}$	$3.58^{+0.271}_{-0.064}$	$0.723^{+0.026}_{-0.065}$		$0.135^{+1.668}_{-0.126}$	$34.235^{+13.39}_{-10.242}$	$71.695^{+95.248}_{-13.077}$
	A8	$1669.219^{+17.466}_{-104.36}$	$3.572^{+0.285}_{-0.116}$	$0.715^{+0.029}_{-0.148}$	$1.871^{+0.16}_{-0.073}$		$34.425^{+22.003}_{-13.74}$	$74.595^{+195.92}_{-16.106}$
	A9	$1668.42^{+11.423}_{-58.438}$	$3.592^{+0.348}_{-0.066}$	$0.712^{+0.022}_{-0.117}$	$1.877^{+0.235}_{-0.029}$	$0.218^{+2.282}_{-0.207}$	$34.457^{+19.522}_{-11.553}$	$72.951^{+163.949}_{-13.906}$
w/o/ cont	A10	$1547.213^{+290.759}_{-16.517}$	$2.762^{+0.62}_{-0.227}$	$0.778^{+0.029}_{-0.086}$				
	A11	$1734.403^{+216.96}_{-188.836}$	$3.365^{+0.616}_{-0.664}$	$0.679^{+0.13}_{-0.147}$			$31.001^{+10.621}_{-3.419}$	
	A12	$1914.159^{+62.746}_{-265.945}$	$3.724^{+0.349}_{-0.586}$	$0.57^{+0.173}_{-0.078}$			$33.735^{+25.456}_{-6.135}$	$46.45^{+134.002}_{-18.502}$
	A13	$1854.536^{+113.231}_{-345.667}$	$3.693^{+0.39}_{-0.582}$	$0.584^{+0.215}_{-0.089}$	$1.141^{+1.401}_{-0.141}$		$34.211^{+82.226}_{-7.385}$	$55.309^{+205.908}_{-23.175}$
J band	A14	$1634.494^{+63.535}_{-8.919}$	$4.658^{+0.098}_{-0.315}$	$0.329^{+0.218}_{-0.043}$				
w/ cont	A15	$1633.677^{+70.487}_{-25.772}$	$4.642^{+0.109}_{-0.511}$	$0.364^{+0.323}_{-0.077}$	$1.989^{+0.566}_{-0.104}$			
	A16	$1635.691^{+45.38}_{-8.413}$	$4.656^{+0.094}_{-0.183}$	$0.322^{+0.175}_{-0.036}$			$38.572^{+17.209}_{-7.514}$	$19.923^{+34.725}_{-13.227}$
	A17	$1634.751^{+48.514}_{-11.448}$	$4.647^{+0.1}_{-0.374}$	$0.341^{+0.298}_{-0.055}$	$1.98^{+0.38}_{-0.076}$		$38.598^{+21.657}_{-10.762}$	$21.957^{+41.895}_{-14.758}$
w/o/ cont	A18	$1574.598^{+29.652}_{-46.295}$	$4.602^{+0.126}_{-0.547}$	$0.361^{+0.223}_{-0.066}$				
	A19	$1570.457^{+26.531}_{-54.872}$	$4.571^{+0.148}_{-0.634}$	$0.383^{+0.247}_{-0.085}$	$4.25^{+1.946}_{-0.271}$			
	A20	$1581.443^{+17.467}_{-42.373}$	$4.621^{+0.107}_{-0.491}$	$0.34^{+0.191}_{-0.047}$			$38.571^{+12.959}_{-7.026}$	$25.574^{+40.077}_{-17.063}$
	A21	$1578.189^{+20.296}_{-51.294}$	$4.599^{+0.125}_{-0.578}$	$0.358^{+0.223}_{-0.062}$	$4.24^{+1.549}_{-0.228}$		$38.655^{+14.9}_{-8.09}$	$28.599^{+41.433}_{-19.562}$
H band	A22	$1895.624^{+16.422}_{-171.627}$	$4.014^{+0.847}_{-0.223}$	$0.971^{+0.017}_{-0.275}$				
	A23	$1878.841^{+32.16}_{-273.962}$	$4.06^{+0.776}_{-0.271}$	$0.929^{+0.058}_{-0.349}$	$1.339^{+0.811}_{-0.065}$			
L_p band	A24	$1950.32^{+21.064}_{-355.0}$	$3.573^{+0.323}_{-0.068}$	$0.918^{+0.029}_{-0.167}$				
	A25	$1872.449^{+100.324}_{-281.65}$	$3.632^{+0.618}_{-0.124}$	$0.867^{+0.08}_{-0.214}$	$1.286^{+0.275}_{-0.032}$			
Adopted Values		1800 ± 20	$4.6^{+0.1}_{-0.5}$	0.71 ± 0.15	1.8 ± 0.2	-	32.9 ± 10	-

Table 3.4: Table presenting the multi-modelels with BT-SETTL13. The priors are listed on the first row. We explored the outcomes varying wavelength ranges and number of free parameters. The models are labeled with a A from 0 to 25 and the adopted values from this work and this atmospheric grid are listed in the last row. A0, A8 and A20 are the models presented on the text and we colored them to match the colors on Figure 3.5 and 3.6.

Exo-REM		T_{eff} (K)	$log(g)$ (dex)	$[M/H]$	$^C/_O$	R (R_{jup})	A_v mag	RV (kms^{-1})	$vsin(i)$ (kms^{-1})
Priors		$(400-2000)$	$(3-5)$	$(-0.5-1)$	$(0.1-0.8)$	$(0.5-10)$	$(0-5)$	$(-10-100)$	$(0-100)$
Full SED	B0	$1699.999^{+1.747}_{-55.771}$	$3.5^{+0.014}_{-0.078}$	$0.996^{+0.004}_{-0.264}$	$0.674^{+0.001}_{-0.322}$				
	B1	$1989.661^{+5.703}_{-133.599}$	$3.501^{+0.069}_{-0.094}$	$0.184^{+0.54}_{-0.009}$	$0.698^{+0.002}_{-0.334}$		$3.249^{+0.07}_{-1.057}$		
$JHKL_p$	B2	$1698.912^{+15.517}_{-69.254}$	$3.526^{+0.11}_{-0.225}$	$0.985^{+0.015}_{-0.402}$	$0.775^{+0.018}_{-0.219}$				
K band	B3	$1776.139^{+9.715}_{-313.165}$	$3.313^{+0.867}_{-0.029}$	$0.769^{+0.918}_{-0.036}$	$0.842^{+0.021}_{-0.22}$				
w/ cont	B4	$1774.463^{+7.026}_{-226.354}$	$3.268^{+0.761}_{-0.038}$	$0.766^{+0.306}_{-0.116}$	$0.805^{+0.027}_{-0.251}$			$19.043^{+4.423}_{-4.04}$	
	B5	$1798.655^{+84.921}_{-168.318}$	$4.026^{+0.227}_{-0.409}$	$0.516^{+0.57}_{-0.179}$	$0.581^{+0.085}_{-0.058}$			$26.989^{+11.932}_{-10.88}$	$74.476^{+10.44}_{-16.511}$
	B6	$1891.983^{+96.408}_{-254.176}$	$3.82^{+0.468}_{-0.206}$	$0.529^{+0.54}_{-0.178}$	$0.641^{+0.03}_{-0.12}$		$1.171^{+0.686}_{-2.69}$	$26.852^{+11.586}_{-9.446}$	$74.269^{+9.952}_{-15.969}$
	B7	$1758.014^{+47.605}_{-320.941}$	$3.964^{+0.161}_{-0.49}$	$0.36^{+0.21}_{-0.156}$	$0.582^{+0.082}_{-0.08}$	$1.699^{+0.756}_{-0.062}$		$28.476^{+21.878}_{-8.764}$	$73.106^{+11.13}_{-26.878}$
	B8	$1805.908^{+180.25}_{-285.445}$	$3.762^{+0.369}_{-0.369}$	$0.331^{+0.225}_{-0.141}$	$0.631^{+0.039}_{-0.129}$	$1.64^{+0.642}_{-0.163}$	$1.061^{+1.257}_{-2.427}$	$28.25^{+18.477}_{-7.34}$	$73.688^{+10.82}_{-23.9}$
w/o/ cont	B9	$1859.516^{+35.847}_{-80.114}$	$4.779^{+0.066}_{-0.641}$	$1.894^{+5.151}_{-0.702}$	$0.894^{+0.104}_{-0.13}$				
	B10	$1848.007^{+51.5}_{-122.091}$	$4.768^{+0.105}_{-0.979}$	$2.124^{+5.242}_{-0.932}$	$0.873^{+0.108}_{-0.264}$			$30.11^{+3.05}_{-3.44}$	
	B11	$1927.75^{+24.62}_{-190.296}$	$4.822^{+0.156}_{-1.053}$	$6.395^{+2.468}_{-3.4}$	$0.627^{+0.207}_{-0.12}$			$33.366^{+5.059}_{-5.097}$	$47.516^{+21.874}_{-11.568}$
	B12	$1856.145^{+90.151}_{-685.057}$	$4.765^{+0.203}_{-1.177}$	$2.482^{+2.103}_{-1.885}$	$0.625^{+0.069}_{-0.132}$	$0.957^{+0.808}_{-0.401}$		$33.457^{+7.636}_{-11.118}$	$48.282^{+25.212}_{-13.564}$
J band	B13	$1606.899^{+124.331}_{-33.254}$	$4.709^{+0.14}_{-0.938}$	$0.5^{+0.216}_{-0.244}$	$0.201^{+0.261}_{-0.013}$				
w/ cont	B14	$1601.977^{+74.474}_{-296.717}$	$4.675^{+0.164}_{-0.951}$	$0.483^{+0.232}_{-0.397}$	$0.216^{+0.313}_{-0.027}$	$1.834^{+1.73}_{-0.272}$			
	B15	$1608.324^{+141.421}_{-27.001}$	$4.732^{+0.142}_{-0.86}$	$0.509^{+0.222}_{-0.24}$	$0.2^{+0.214}_{-0.016}$			$37.22^{+11.713}_{-8.853}$	$21.398^{+33.0}_{-14.094}$
	B16	$1508.373^{+92.818}_{-249.583}$	$4.709^{+0.147}_{-0.657}$	$0.436^{+0.236}_{-0.448}$	$0.262^{+0.308}_{-0.071}$	$2.189^{+1.924}_{-0.349}$		$37.634^{+17.752}_{-11.403}$	$27.508^{+32.442}_{-16.317}$
w/o/ cont	B17	$1179.249^{+79.177}_{-28.229}$	$4.746^{+0.219}_{-0.581}$	$-0.383^{+0.639}_{-0.106}$	$0.741^{+0.031}_{-0.215}$				
	B18	$1193.88^{+85.057}_{-39.39}$	$4.79^{+0.173}_{-0.658}$	$-0.276^{+0.677}_{-0.091}$	$0.744^{+0.027}_{-0.277}$	$9.272^{+0.584}_{-2.976}$			
	B19	$1217.12^{+47.443}_{-52.935}$	$4.507^{+0.228}_{-0.292}$	$-0.36^{+0.62}_{-0.127}$	$0.672^{+0.075}_{-0.111}$			$35.577^{+9.118}_{-8.186}$	$22.762^{+38.701}_{-14.962}$
	B20	$1197.777^{+103.489}_{-36.059}$	$4.756^{+0.172}_{-0.613}$	$-0.266^{+0.746}_{-0.094}$	$0.74^{+0.022}_{-0.255}$	$9.344^{+0.54}_{-2.832}$		$35.457^{+10.569}_{-9.555}$	$22.117^{+41.38}_{-14.455}$
H band	B21	$1919.165^{+65.957}_{-411.519}$	$3.827^{+0.571}_{-0.412}$	$0.313^{+0.526}_{-0.392}$	$0.479^{+0.231}_{-0.21}$				
	B22	$1857.722^{+122.851}_{-598.844}$	$3.865^{+0.654}_{-0.45}$	$0.243^{+0.55}_{-0.406}$	$0.512^{+0.198}_{-0.235}$	$1.379^{+2.021}_{-0.144}$			
L_p band	B23	$1692.135^{+119.861}_{-60.382}$	$3.543^{+0.371}_{-0.314}$	$0.784^{+0.154}_{-0.62}$	$0.769^{+0.016}_{-0.462}$				
	B24	$1686.411^{+111.356}_{-256.474}$	$3.562^{+0.627}_{-0.306}$	$0.724^{+0.198}_{-0.686}$	$0.703^{+0.08}_{-0.421}$	$1.635^{+0.363}_{-0.136}$			
Adopted Values		1700 ± 50	4.5 ± 0.3	0.36 ± 0.2	0.58 ± 0.08	$1.7^{+0.8}_{-0.1}$	-	32.3 ± 5	-

Table 3.5: This Table is analogous as Table 3.4 but for Exo-REM wich has a non constant $[M/H]$ and models are labeled with a B from 0 to 24. B0, B7 and, B19 are the ones represented in Figure 3.5 and 3.7.

Chapter 4

Conclusions

In the introduction we give a broad review of this research topic's state of the art. Massive exoplanets and brown dwarfs share many observable properties, which motivates the understanding of their origins. We know that these are two different populations of objects, and by studying the imprints left on their atmospheres, when they are still young, it is expected that we are able to trace the mechanism and location of formation and even a further evolution history.

We started this project by selecting a sample of substellar young companions and isolated objects. The main idea was to systematically study their atmospheres related to their architectures to identify common tendencies. This part of the project is currently under development, but the initial stage was completed. In chapter 2, the reduced and corrected spectra for the 24 targets and the methods can be found, together with evolutionary models predictions for the physical and chemical characteristics of the sample. In the near future, we will model the atmospheres and precisely constraint the $^C/_O$ ratio for the sample. If those targets follow a similar trend as showed in Brewer and Fischer (2016) for stars, then we proposed that they were formed through GtF or GI, centered at a slightly higher $^C/_O$ ratio since these are young targets (Chiappini et al., 2003). If the $^C/_O$ ratios of the sample are lower or higher, we propose that those targets probably formed through CA or accreted material at final formation stages. These are general ideas at the moment, but we are looking forward to test them.

Given the short time of a master project, we decided to focus on characterizing one of the targets. We selected for this scope AB Pic b, a companion with a rich set of previous observations ideal for a profound characterization of its atmospheric physical and chemical characteristics. We explore its atmosphere using a tool called ForMoSA based on a Bayesian approach. From the results of the atmospheric modeling together with the outcomes from evolutionary models and the study of the orbital properties, we propose that AB Pic b was most likely formed by gravitational instabilities or core/ pebble accretion at large separation (beyond the CO snowline) at early stages in a massive protoplanetary disk, given its stellar $^C/_O$ ratio together with the slightly super-stellar metallicity. However, other scenarios cannot be ruled out with our current system understanding, mostly due to the incapacity for estimating the eccentricity from the current available observations together with the missing

exploration of the carbon isotopologues ratio. A high-resolution spectrum would be ideal to further prove this story by allowing a constraint on the eccentricity and a detailed revision on other physical properties.

In the future, by comparing AB Pic b to other similar objects, we could make further constraints. This topic is highly active and promises to be revolutionized with the future generation of telescopes. In this line, when data from the ELT or JWST is available, AB Pic b will be a prime target to test further the ideas of relating atmospheric characteristics to formation processes, given their high resolutions and broad wavelength coverage (see Figure 3.10). Hopefully we will even be able to split the population of brown dwarfs from the population of massive gaseous exoplanets, one of the big questions that prompted this master project.

Finally, regarding the continuity of this project, we will work on this sample to test these ideas further during the following years as part of my upcoming Ph.D. project at the Laboratoire Lagrange and the Observatoire de la Côte d'Azur in Nice, France. I am highly enthusiastic about the coming years and looking forward to the road that this project will be taking and where the future observations will guide us.

Acknowledgements

Bibliography

Rachel L. Akeson, Eric L. N. Jensen, John Carpenter, Luca Ricci, Stefan Laos, Natasha F. Nogueira, and Emma M. Suen-Lewis. Resolved Young Binary Systems and Their Disks. *The Astrophysical Journal*, 872(2):158, 2019. ISSN 1538-4357. doi: 10.3847/1538-4357/aaff6a.

F. Allard, D. Homeier, B. Freytag, W. Schaffenberger, and A. S. Rajpurohit. Progress in modeling very low mass stars, brown dwarfs, and planetary mass objects. *Memorie della Societa Astronomica Italiana - Journal of the Italian Astronomical Society*, 24(2002):128–137, 2013. ISSN 1824016X.

France Allard, Peter H Hauschildt, David R Alexander, Akemi Tamanai, and Andreas Schweitzer. The Limiting Effects of Dust in Brown Dwarf Model Atmospheres. 556(1): 357–372, 7 2001. doi: 10.1086/321547. URL https://doi.org/10.1086/321547.

K. N. Allers and Michael C. Liu. A near-infrared spectroscopic study of young field ultracool dwarfs. *Astrophysical Journal*, 772(2), 2013. ISSN 15384357. doi: 10.1088/0004-637X/772/2/79.

Dániel Apai, Jacqueline Radigan, Esther Buenzli, Adam Burrows, Iain Neill Reid, and Ray Jayawardhana. {HSTSPECTRAL} {MAPPING} {OF} L/T {TRANSITION} {BROWN} {DWARFS} {REVEALS} {CLOUD} {THICKNESS} {VARIATIONS}. *The Astrophysical Journal*, 768(2):121, 4 2013. doi: 10.1088/0004-637x/768/2/121. URL https://doi.org/10.1088/0004-637x/768/2/121.

Philip J Armitage. Planet Formation lecture by Roy van Boekel (MPIA) suggested reading: "LECTURE NOTES ON THE FORMATION AND EARLY EVOLUTION OF PLANETARY SYSTEMS" with material from Kees Dullemond, Christoph Mordasini, Til Birnstiel.

Isabelle Baraffe, Derek Homeier, France Allard, and Gilles Chabrier. New evolutionary models for pre-main sequence and main sequence low-mass stars down to the hydrogen-burning limit. *Astronomy and Astrophysics*, 577(1997):1–7, 2015. ISSN 14320746. doi: 10.1051/0004-6361/201425481.

J. L. Beuzit, A. Vigan, D. Mouillet, K. Dohlen, R. Gratton, A. Boccaletti, J. F. Sauvage, H. M. Schmid, M. Langlois, C. Petit, A. Baruffolo, M. Feldt, J. Milli, Z. Wahhaj, L. Abe, U. Anselmi, J. Antichi, R. Barette, J. Baudrand, P. Baudoz, A. Bazzon, P. Bernardi, P. Blanchard, R. Brast, P. Bruno, T. Buey, M. Carbillet, M. Carle, E. Cascone, F. Chapron, J. Charton, G. Chauvin, R. Claudi, A. Costille, V. De Caprio, J. De Boer, A. Delboulbé,

S. Desidera, C. Dominik, M. Downing, O. Dupuis, C. Fabron, D. Fantinel, G. Farisato, P. Feautrier, E. Fedrigo, T. Fusco, P. Gigan, C. Ginski, J. Girard, E. Giro, D. Gisler, L. Gluck, C. Gry, T. Henning, N. Hubin, E. Hugot, S. Incorvaia, M. Jaquet, M. Kasper, E. Lagadec, A. M. Lagrange, H. Le Coroller, D. Le Mignant, B. Le Ruyet, G. Lessio, J. L. Lizon, M. Llored, L. Lundin, F. Madec, Y. Magnard, M. Marteaud, P. Martinez, D. Maurel, F. Ménard, D. Mesa, O. Möller-Nilsson, T. Moulin, C. Moutou, A. Origné, J. Parisot, A. Pavlov, D. Perret, J. Pragt, P. Puget, P. Rabou, J. Ramos, J. M. Reess, F. Rigal, S. Rochat, R. Roelfsema, G. Rousset, A. Roux, M. Saisse, B. Salasnich, E. Santambrogio, S. Scuderi, D. Segransan, A. Sevin, R. Siebenmorgen, C. Soenke, E. Stadler, M. Suarez, D. Tiphène, M. Turatto, S. Udry, F. Vakili, L. B.F.M. Waters, L. Weber, F. Wildi, G. Zins, and A. Zurlo. SPHERE: The exoplanet imager for the Very Large Telescope. *Astronomy and Astrophysics*, 631, 2019. ISSN 14320746. doi: 10.1051/0004-6361/201935251.

Blain, D., Charnay, B., and Bézard, B. 1D atmospheric study of the temperate sub-Neptune K2-18b. *A\&A*, 646:A15, 2021. doi: 10.1051/0004-6361/202039072. URL https://doi.org/10.1051/0004-6361/202039072.

Sarah Blunt, Eric L Nielsen, Robert J De Rosa, Quinn M Konopacky, Dominic Ryan, Jason J Wang, Laurent Pueyo, Julien Rameau, Christian Marois, Franck Marchis, Bruce Macintosh, James R Graham, Gaspard Duchêne, and Adam C Schneider. Orbits for the Impatient: A Bayesian Rejection-sampling Method for Quickly Fitting the Orbits of Long-period Exoplanets. *\aj*, 153(5):229, 5 2017. doi: 10.3847/1538-3881/aa6930.

Sarah Blunt, Jason J Wang, Isabel Angelo, Henry Ngo, Devin Cody, Robert J De Rosa, James R Graham, Lea Hirsch, Vighnesh Nagpal, Eric L Nielsen, Logan Pearce, Malena Rice, and Roberto Tejada. orbitize!: A Comprehensive Orbit-fitting Software Package for the High-contrast Imaging Community. *\aj*, 159(3):89, 3 2020. doi: 10.3847/1538-3881/ab6663.

M. Bonnefoy, G. Chauvin, P. Rojo, F. Allard, A. M. Lagrange, D. Homeier, C. Dumas, and J. L. Beuzit. Near-infrared integral-field spectra of the planet/brown dwarf companion AB Pictoris b. *Astronomy and Astrophysics*, 512(8), 2010. ISSN 14320746. doi: 10.1051/0004-6361/200912688.

M. Bonnefoy, G. Chauvin, A. M. Lagrange, P. Rojo, F. Allard, C. Pinte, C. Dumas, and D. Homeier. A library of near-infrared integral field spectra of young M-L dwarfs. *Astronomy and Astrophysics*, 562:1–26, 2014. ISSN 00046361. doi: 10.1051/0004-6361/201118270.

Henri Bonnet, Ralf Conzelmann, Bernhard Delabre, Rachael Donaldson, Enrico Fedrigo, N Hubin, Markus Kissler-Patig, J.-L Lizon, J Paufique, Silvio Rossi, S Ströbele, and Sebastien Tordo. Astronomical Telescopes and Instrumentation. pages 130–138, 10 2004.

Mark Booth, Carlos Del Burgo, and Valeri V. Hambaryan. The age of the carina young association and potential membership of HD 95086. *Monthly Notices of the Royal Astronomical Society*, 500(4):5552–5560, 2021. ISSN 13652966. doi: 10.1093/mnras/staa3631.

A. P. Boss. Giant planet formation by gravitational instability. *Science*, 276:1836–1839, 1 1997. doi: 10.1126/science.276.5320.1836.

Brendan P. Bowler, Michael C. Liu, Adam L. Kraus, Andrew W. Mann, and Michael J. Ireland. A disk around the planetary-mass companion GSC06214-00210b: Clues about the formation of gas giants on wide orbits. *Astrophysical Journal*, 743(2), 2011. ISSN 15384357. doi: 10.1088/0004-637X/743/2/148.

John M. Brewer and Debra A. Fischer. C/O AND Mg/Si RATIOS OF STARS IN THE SOLAR NEIGHBORHOOD. *The Astrophysical Journal*, 831(1):20, 2016. ISSN 0004-637X. doi: 10.3847/0004-637x/831/1/20. URL http://dx.doi.org/10.3847/0004-637X/831/1/20.

Cesar Briceno, K. L. Luhman, Lee Hartmann, John R. Stauffer, and J. Davy Kirkpatrick. The Initial Mass Function in the Taurus Star-forming Region. *The Astrophysical Journal*, 580(1):317–335, 2002. ISSN 0004-637X. doi: 10.1086/343127.

Marta L Bryan, Eugene Chiang, Caroline V Morley, Gregory N Mace, and Brendan P Bowler. Obliquity Constraints on the Planetary-mass Companion HD 106906 b. 2021.

Gilles Chabrier, Anders Johansen, Markus Janson, S R Jan, and Roman Rafikov. Giant planet and brown dwarf formation. 2014.

David Charbonneau. HD 209458 and the Power of the Dark Side. *Arxiv preprint astro-ph/0209517*, pages 1–8, 2002.

B. Charnay, D. Blain, B. Bézard, J. Leconte, M. Turbet, and A. Falco. Formation and dynamics of water clouds on temperate sub-Neptunes: The example of K2-18b. *Astronomy and Astrophysics*, 646:1–15, 2021. ISSN 14320746. doi: 10.1051/0004-6361/202039525.

G. Chauvin, A. M. Lagrange, B. Zuckerman, C. Dumas, D. Mouillet, I. Song, J. L. Beuzit, P. Lowrance, and M. S. Bessell. A companion to AB Pic at the planet/brown dwarf boundary. *Astronomy and Astrophysics*, 438(3):1–5, 2005. ISSN 00046361. doi: 10.1051/0004-6361:200500111.

G. Chauvin, A. M. Lagrange, H. Beust, M. Bonnefoy, A. Boccaletti, D. Apai, F. Allard, D. Ehrenreich, J. H.V. Girard, D. Mouillet, and D. Rouan. Orbital characterization of the β Pictoris b giant planet. *Astronomy and Astrophysics*, 542(18346), 2012. ISSN 00046361. doi: 10.1051/0004-6361/201118346.

G. Chauvin, S. Desidera, A. M. Lagrange, A. Vigan, R. Gratton, M. Langlois, M. Bonnefoy, J. L. Beuzit, M. Feldt, D. Mouillet, M. Meyer, A. Cheetham, B. Biller, A. Boccaletti, V. D'Orazi, R. Galicher, J. Hagelberg, A. L. Maire, D. Mesa, J. Olofsson, M. Samland, T. O.B. Schmidt, E. Sissa, M. Bonavita, B. Charnay, M. Cudel, S. Daemgen, P. Delorme, P. Janin-Potiron, M. Janson, M. Keppler, H. Le Coroller, R. Ligi, G. D. Marleau, S. Messina, P. Mollière, C. Mordasini, A. Müller, S. Peretti, C. Perrot, L. Rodet, D. Rouan, A. Zurlo, C. Dominik, T. Henning, F. Menard, H. M. Schmid, M. Turatto, S. Udry, F. Vakili, L. Abe, J. Antichi, A. Baruffolo, P. Baudoz, J. Baudrand, P. Blanchard, A. Bazzon, T. Buey, M. Carbillet, M. Carle, J. Charton, E. Cascone, R. Claudi, A. Costille, A. Deboulbe, V. De Caprio, K. Dohlen, D. Fantinel, P. Feautrier, T. Fusco, P. Gigan, E. Giro, D. Gisler, L. Gluck, N. Hubin, E. Hugot, M. Jaquet, M. Kasper, F. Madec, Y. Magnard, P. Martinez, D. Maurel, D. Le Mignant, O. Möller-Nilsson, M. Llored, T. Moulin, A. Origné, A. Pavlov, D. Perret, C. Petit, J. Pragt, P. Puget, P. Rabou,

J. Ramos, R. Rigal, S. Rochat, R. Roelfsema, G. Rousset, A. Roux, B. Salasnich, J. F. Sauvage, A. Sevin, C. Soenke, E. Stadler, M. Suarez, L. Weber, F. Wildi, S. Antoniucci, J. C. Augereau, J. L. Baudino, W. Brandner, N. Engler, J. Girard, C. Gry, Q. Kral, T. Kopytova, E. Lagadec, J. Milli, C. Moutou, J. Schlieder, J. Szulágyi, C. Thalmann, and Z. Wahhaj. Discovery of a warm, dusty giant planet around HIP 65426. *Astronomy and Astrophysics*, 605:1–9, 2017. ISSN 14320746. doi: 10.1051/0004-6361/201731152.

Anthony C. Cheetham, Adam L. Kraus, Michael J. Ireland, Lucas Cieza, Aaron C. Rizzuto, and Peter G. Tuthill. MAPPING the SHORES of the BROWN DWARF DESERT. IV. OPHIUCHUS. *Astrophysical Journal*, 813(2):762–782, 2015. ISSN 15384357. doi: 10.1088/0004-637X/813/2/83.

Cristina Chiappini, Donatella Romano, and Francesca Matteucci. Oxygen, carbon and nitrogen evolution in galaxies. *Monthly Notices of the Royal Astronomical Society*, 339 (1):63–81, 2003. ISSN 00358711. doi: 10.1046/j.1365-8711.2003.06154.x.

R U Claudi, M Turatto, R G Gratton, J Antichi, M Bonavita, P Bruno, E Cascone, V De Caprio, S Desidera, E Giro, D Mesa, S Scuderi, K Dohlen, J L Beuzit, and P Puget. SPHERE IFS: the spectro differential imager of the VLT for exoplanets search. In Ian S McLean and Mark M Casali, editors, *Ground-based and Airborne Instrumentation for Astronomy II*, volume 7014, pages 1188–1198. International Society for Optics and Photonics, SPIE, 2008. doi: 10.1117/12.788366. URL `https://doi.org/10.1117/12.788366`.

Kjetil Dohlen, Maud Langlois, Michel Saisse, L Hill, A Origne, M Jacquet, C Fabron, J C Blanc, M Llored, M Carle, and others. Ground-based and Airborne Instrumentation for Astronomy II. In *Proc. SPIE*, volume 7014, page 70143L, 2008.

Frank Eisenhauer, Roberto Abuter, Klaus Bickert, Fabio Biancat-Marchet, Henri Bonnet, Joar Brynnel, Ralf D. Conzelmann, Bernard Delabre, Robert Donaldson, Jacopo Farinato, Enrico Fedrigo, Reinhard Genzel, Norbert N. Hubin, Christof Iserlohe, Markus E. Kasper, Markus Kissler-Patig, Guy J. Monnet, Claudia Roehrle, Juergen Schreiber, Stefan Stroebele, Matthias Tecza, Niranjan A. Thatte, and Harald Weisz. SINFONI - Integral field spectroscopy at 50 milli-arcsecond resolution with the ESO VLT. *Instrument Design and Performance for Optical/Infrared Ground-based Telescopes*, 4841:1548, 2003. ISSN 0277786X. doi: 10.1117/12.459468.

D H Forgan, C Hall, F Meru, and W K M Rice. Towards a population synthesis model of self-gravitating disc fragmentation and tidal downsizing {II}: the effect of fragment{\textendash}fragment interactions. *Monthly Notices of the Royal Astronomical Society*, 474(4):5036–5048, 11 2017. doi: 10.1093/mnras/stx2870. URL `https://doi.org/10.1093%2Fmnras%2Fstx2870`.

Jonathan J. Fortney. Modeling Exoplanetary Atmospheres: An Overview. *arXiv*, pages 1–40, 2018. ISSN 23318422. doi: 10.1007/978-3-319-89701-1{_}2.

Jonathan J Fortney, Joanna K Barstow, and Nikku Madhusudhan. Atmospheric Modeling and Retrieval. In *ExoFrontiers*, 2514-3433, pages 10–17. IOP Publishing, 2021. ISBN 978-0-7503-1472-5. doi: 10.1088/2514-3433/abfa8fch17. URL `http://dx.doi.org/10.1088/2514-3433/abfa8fch17`.

Gaia Collaboration, A. G. A. Brown, A Vallenari, T Prusti, J. H. J. de Bruijne, C Babusiaux, M Biermann, O. L. Creevey, D. W. Evans, L Eyer, A Hutton, F Jansen, C Jordi, S. A. Klioner, U Lammers, L Lindegren, X Luri, F Mignard, C Panem, D Pourbaix, S Randich, P Sartoretti, C Soubiran, N. A. Walton, F Arenou, C. A. L. Bailer-Jones, U Bastian, M Cropper, R Drimmel, D Katz, M. G. Lattanzi, F van Leeuwen, J Bakker, C Cacciari, J Castañeda, F De Angeli, C Ducourant, C Fabricius, M Fouesneau, Y Frémat, R Guerra, A Guerrier, J Guiraud, A Jean-Antoine Piccolo, E Masana, R Messineo, N Mowlavi, C Nicolas, K Nienartowicz, F Pailler, P Panuzzo, F Riclet, W Roux, G. M. Seabroke, R Sordo, P Tanga, F Thévenin, G Gracia-Abril, J Portell, D Teyssier, M Altmann, R Andrae, I Bellas-Velidis, K Benson, J Berthier, R Blomme, E Brugaletta, P. W. Burgess, G Busso, B Carry, A Cellino, N Cheek, G Clementini, Y Damerdji, M Davidson, L Delchambre, A Dell'Oro, J Fernández-Hernández, L Galluccio, P Garc\'\ia-Lario, M Garcia-Reinaldos, J González-Núñez, E Gosset, R Haigron, J L. Halbwachs, N. C. Hambly, D. L. Harrison, D Hatzidimitriou, U Heiter, J Hernández, D Hestroffer, S. T. Hodgkin, B Holl, K Janßen, G Jevardat de Fombelle, S Jordan, A Krone-Martins, A. C. Lanzafame, W Löffler, A Lorca, M Manteiga, O Marchal, P. M. Marrese, A Moitinho, A Mora, K Muinonen, P Osborne, E Pancino, T Pauwels, J M. Petit, A Recio-Blanco, P. J. Richards, M Riello, L Rimoldini, A. C. Robin, T Roegiers, J Rybizki, L. M. Sarro, C Siopis, M Smith, A Sozzetti, A Ulla, E Utrilla, M van Leeuwen, W van Reeven, U Abbas, A Abreu Aramburu, S Accart, C Aerts, J. J. Aguado, M Ajaj, G Altavilla, M. A. Álvarez, J Álvarez Cid-Fuentes, J Alves, R. I. Anderson, E Anglada Varela, T Antoja, M Audard, D Baines, S. G. Baker, L Balaguer-Núñez, E Balbinot, Z Balog, C Barache, D Barbato, M Barros, M. A. Barstow, S Bartolomé, J L. Bassilana, N Bauchet, A Baudesson-Stella, U Becciani, M Bellazzini, M Bernet, S Bertone, L Bianchi, S Blanco-Cuaresma, T Boch, A Bombrun, D Bossini, S Bouquillon, A Bragaglia, L Bramante, E Breedt, A Bressan, N Brouillet, B Bucciarelli, A Burlacu, D Busonero, A. G. Butkevich, R Buzzi, E Caffau, R Cancelliere, H Cánovas, T Cantat-Gaudin, R Carballo, T Carlucci, M. I. Carnerero, J. M. Carrasco, L Casamiquela, M Castellani, A Castro-Ginard, P Castro Sampol, L Chaoul, P Charlot, L Chemin, A Chiavassa, M R. L. Cioni, G Comoretto, W. J. Cooper, T Cornez, S Cowell, F Crifo, M Crosta, C Crowley, C Dafonte, A Dapergolas, M David, P David, P de Laverny, F De Luise, R De March, J De Ridder, R de Souza, P de Teodoro, A de Torres, E. F. del Peloso, E del Pozo, M Delbo, A Delgado, H. E. Delgado, J B. Delisle, P Di Matteo, S Diakite, C Diener, E Distefano, C Dolding, D Eappachen, B Edvardsson, H Enke, P Esquej, C Fabre, M Fabrizio, S Faigler, G Fedorets, P Fernique, A Fienga, F Figueras, C Fouron, F Fragkoudi, E Fraile, F Franke, M Gai, D Garabato, A Garcia-Gutierrez, M Garc\'\ia-Torres, A Garofalo, P Gavras, E Gerlach, R Geyer, P Giacobbe, G Gilmore, S Girona, G Giuffrida, R Gomel, A Gomez, I Gonzalez-Santamaria, J. J. González-Vidal, M Granvik, R Gutiérrez-Sánchez, L. P. Guy, M Hauser, M Haywood, A Helmi, S. L. Hidalgo, T Hilger, N Hładczuk, D Hobbs, G Holland, H. E. Huckle, G Jasniewicz, P. G. Jonker, J Juaristi Campillo, F Julbe, L Karbevska, P Kervella, S Khanna, A Kochoska, M Kontizas, G Kordopatis, A. J. Korn, Z Kostrzewa-Rutkowska, K Kruszyńska, S Lambert, A. F. Lanza, Y Lasne, J F. Le Campion, Y Le Fustec, Y Lebreton, T Lebzelter, S Leccia, N Leclerc, I Lecoeur-Taibi, S Liao, E Licata, E. P. Lindstrøm, T. A. Lister, E Livanou, A Lobel, P Madrero Pardo, S Managau, R. G. Mann, J. M. Marchant, M Marconi, M. M. S. Marcos Santos, S Marinoni, F Marocco, D. J. Marshall, L Martin Polo, J. M. Mart\'\in-Fleitas, A Masip, D Massari, A Mastrobuono-Battisti, T Mazeh, P. J. McMillan, S Messina, D Michalik, N. R. Millar, A Mints,

D Molina, R Molinaro, L Molnár, P Montegriffo, R Mor, R Morbidelli, T Morel, D Morris, A. F. Mulone, D Munoz, T Muraveva, C. P. Murphy, I Musella, L Noval, C Ordénovic, G Orrù, J Osinde, C Pagani, I Pagano, L Palaversa, P. A. Palicio, A Panahi, M Pawlak, X Peñalosa Esteller, A Penttilä, A. M. Piersimoni, F X. Pineau, E Plachy, G Plum, E Poggio, E Poretti, E Poujoulet, A Prša, L Pulone, E Racero, S Ragaini, M Rainer, C. M. Raiteri, N Rambaux, P Ramos, M Ramos-Lerate, P Re Fiorentin, S Regibo, C Reylé, V Ripepi, A Riva, G Rixon, N Robichon, C Robin, M Roelens, L Rohrbasser, M Romero-Gómez, N Rowell, F Royer, K. A. Rybicki, G Sadowski, A Sagristà Sellés, J Sahlmann, J Salgado, E Salguero, N Samaras, V Sanchez Gimenez, N Sanna, R Santoveña, M Sarasso, M Schultheis, E Sciacca, M Segol, J. C. Segovia, D Ségransan, D Semeux, S Shahaf, H. I. Siddiqui, A Siebert, L Siltala, E Slezak, R. L. Smart, E Solano, F Solitro, D Souami, J Souchay, A Spagna, F Spoto, I. A. Steele, H Steidelmüller, C. A. Stephenson, M Süveges, L Szabados, E Szegedi-Elek, F Taris, G Tauran, M. B. Taylor, R Teixeira, W Thuillot, N Tonello, F Torra, J Torra, C Turon, N Unger, M Vaillant, E van Dillen, O Vanel, A Vecchiato, Y Viala, D Vicente, S Voutsinas, M Weiler, T Wevers, L Wyrzykowski, A Yoldas, P Yvard, H Zhao, J Zorec, S Zucker, C Zurbach, and T Zwitter. Gaia Early Data Release 3. Summary of the contents and survey properties. \aap, 649:A1, 5 2021. doi: 10.1051/0004-6361/202039657.

R Galicher, A Boccaletti, D Mesa, P Delorme, R Gratton, M Langlois, A M. Lagrange, A L. Maire, H Le Coroller, G Chauvin, B Biller, F Cantalloube, M Janson, E Lagadec, N Meunier, A Vigan, J Hagelberg, M Bonnefoy, A Zurlo, S Rocha, D Maurel, M Jaquet, T Buey, and L Weber. Astrometric and photometric accuracies in high contrast imaging: The SPHERE speckle calibration tool (SpeCal). \aap, 615:A92, 7 2018. doi: 10.1051/0004-6361/201832973.

Tyler D Groff, N Jeremy Kasdin, Mary Anne Limbach, Michael Galvin, Michael A Carr, Gillian Knapp, Timothy Brandt, Craig Loomis, Norman Jarosik, Kyle Mede, Michael W McElwain, Douglas B Leviton, Kevin H Miller, Manuel A Quijada, Olivier Guyon, Nemanja Jovanovic, Naruhisa Takato, and Masahiko Hayashi. The CHARIS IFS for high contrast imaging at Subaru. In Stuart Shaklan, editor, *Techniques and Instrumentation for Detection of Exoplanets VII*, volume 9605 of *Society of Photo-Optical Instrumentation Engineers (SPIE) Conference Series*, page 96051C, 9 2015. doi: 10.1117/12.2188465.

S. Y. Haffert, A. J. Bohn, J. de Boer, I. A. G. Snellen, J. Brinchmann, J. H. Girard, C. U. Keller, and R. Bacon. Two accreting protoplanets around the young star PDS 70. *Nature Astronomy*, 3(8):749–754, 8 2019. ISSN 2397-3366. doi: 10.1038/s41550-019-0780-5. URL http://www.nature.com/articles/s41550-019-0780-5.

Peter H Hauschildt, E Baron, and France Allard. Parallel Implementation of the {PHOENIX} Generalized Stellar Atmosphere Program. 483(1):390–398, 7 1997. doi: 10.1086/304233. URL https://doi.org/10.1086/304233.

H. J. Hoeijmakers, H. Schwarz, I. A.G. Snellen, R. J. De Kok, M. Bonnefoy, G. Chauvin, A. M. Lagrange, and J. H. Girard. Medium-resolution integral-field spectroscopy for high-contrast exoplanet imaging: Molecule maps of the β Pictoris system with SINFONI. *Astronomy and Astrophysics*, 617:1–11, 2018. ISSN 14320746. doi: 10.1051/0004-6361/201832902.

M. J. Ireland, A. Kraus, F. Martinache, N. Law, and L. A. Hillenbrand. Two wide planetary-mass companions to solar-type stars in upper scorpius. *Astrophysical Journal*, 726(2), 2011. ISSN 15384357. doi: 10.1088/0004-637X/726/2/113.

R. F. Jameson, N. Lodieu, S. L. Casewell, N. P. Bannister, and P. D. Dobbie. The ages of L dwarfs. *Monthly Notices of the Royal Astronomical Society*, 385(4), 2008. ISSN 00358711. doi: 10.1111/j.1365-2966.2008.12973.x.

N. Jovanovic, F. Martinache, O. Guyon, C. Clergeon, G. Singh, T. Kudo, V. Garrel, K. Newman, D. Doughty, J. Lozi, J. Males, Y. Minowa, Y. Hayano, N. Takato, J. Morino, J. Kuhn, E. Serabyn, B. Norris, P. Tuthill, G. Schworer, P. Stewart, L. Close, E. Huby, G. Perrin, S. Lacour, L. Gauchet, S. Vievard, N. Murakami, F. Oshiyama, N. Baba, T. Matsuo, J. Nishikawa, M. Tamura, O. Lai, F. Marchis, G. Duchene, T. Kotani, and J. Woillez. The Subaru Coronagraphic Extreme Adaptive Optics System: Enabling High-Contrast Imaging on Solar-System Scales. *Publications of the Astronomical Society of the Pacific*, 127(955):890–910, 2015. ISSN 00046280. doi: 10.1086/682989.

M. Keppler, M. Benisty, A. Müller, Th Henning, R. Van Boekel, F. Cantalloube, C. Ginski, R. G. Van Holstein, A. L. Maire, A. Pohl, M. Samland, H. Avenhaus, J. L. Baudino, A. Boccaletti, J. De Boer, M. Bonnefoy, G. Chauvin, S. Desidera, M. Langlois, C. Lazzoni, G. D. Marleau, C. Mordasini, N. Pawellek, T. Stolker, A. Vigan, A. Zurlo, T. Birnstiel, W. Brandner, M. Feldt, M. Flock, J. Girard, R. Gratton, J. Hagelberg, A. Isella, M. Janson, A. Juhasz, J. Kemmer, Q. Kral, A. M. Lagrange, R. Launhardt, A. Matter, F. Ménard, J. Milli, P. Mollière, J. Olofsson, L. Pérez, P. Pinilla, C. Pinte, S. P. Quanz, T. Schmidt, S. Udry, Z. Wahhaj, J. P. Williams, E. Buenzli, M. Cudel, C. Dominik, R. Galicher, M. Kasper, J. Lannier, D. Mesa, D. Mouillet, S. Peretti, C. Perrot, G. Salter, E. Sissa, F. Wildi, L. Abe, J. Antichi, J. C. Augereau, A. Baruffolo, P. Baudoz, A. Bazzon, J. L. Beuzit, P. Blanchard, S. S. Brems, T. Buey, V. De Caprio, M. Carbillet, M. Carle, E. Cascone, A. Cheetham, R. Claudi, A. Costille, A. Delboulbé, K. Dohlen, D. Fantinel, P. Feautrier, T. Fusco, E. Giro, L. Gluck, C. Gry, N. Hubin, E. Hugot, M. Jaquet, D. Le Mignant, M. Llored, F. Madec, Y. Magnard, P. Martinez, D. Maurel, M. Meyer, O. Möller-Nilsson, T. Moulin, L. Mugnier, A. Origné, A. Pavlov, D. Perret, C. Petit, J. Pragt, P. Puget, P. Rabou, J. Ramos, F. Rigal, S. Rochat, R. Roelfsema, G. Rousset, A. Roux, B. Salasnich, J. F. Sauvage, A. Sevin, C. Soenke, E. Stadler, M. Suarez, M. Turatto, and L. Weber. Discovery of a planetary-mass companion within the gap of the transition disk around PDS 70. *Astronomy and Astrophysics*, 617:1–23, 2018. ISSN 14320746. doi: 10.1051/0004-6361/201832957.

Adam L. Kraus, Evgenya L. Shkolnik, Katelyn N. Allers, and Michael C. Liu. A stellar census of the tucana-horologium moving group. *Astronomical Journal*, 147(6), 2014. ISSN 00046256. doi: 10.1088/0004-6256/147/6/146.

Fraŋois René Lachapelle, David Lafrenière, Jonathan Gagné, Ray Jayawardhana, Markus Janson, Christiane Helling, and Soeren Witte. Characterization of low-mass, wide-separation substellar companions to stars in upper Scorpius: Near-infrared photometry and spectroscopy. *Astrophysical Journal*, 802(1), 2015. ISSN 15384357. doi: 10.1088/0004-637X/802/1/61.

David Lafrenière, Ray Jayawardhana, and Marten H. van Kerkwijk. Direct Imaging and Spectroscopy of a Planetary-Mass Candidate Companion to a Young Solar Analog. *The Astrophysical Journal*, 689(2):L153–L156, 2008. ISSN 0004-637X. doi: 10.1086/595870.

A. M. Lagrange, A. Boccaletti, M. Langlois, G. Chauvin, R. Gratton, H. Beust, S. Desidera, J. Milli, M. Bonnefoy, A. Cheetham, M. Feldt, M. Meyer, A. Vigan, B. Biller, M. Bonavita, J. L. Baudino, F. Cantalloube, M. Cudel, S. Daemgen, P. Delorme, V. D'Orazi, J. Girard, C. Fontanive, J. Hagelberg, M. Janson, M. Keppler, T. Koypitova, R. Galicher, J. Lannier, H. Le Coroller, R. Ligi, A. L. Maire, D. Mesa, S. Messina, A. Müeller, S. Peretti, C. Perrot, D. Rouan, G. Salter, M. Samland, T. Schmidt, E. Sissa, A. Zurlo, J. L. Beuzit, D. Mouillet, C. Dominik, T. Henning, E. Lagadec, F. Ménard, H. M. Schmid, M. Turatto, S. Udry, A. J. Bohn, B. Charnay, C. A. Gomez Gonzales, C. Gry, M. Kenworthy, Q. Kral, C. Mordasini, C. Moutou, G. Van Der Plas, J. E. Schlieder, L. Abe, J. Antichi, A. Baruffolo, P. Baudoz, J. Baudrand, P. Blanchard, A. Bazzon, T. Buey, M. Carbillet, M. Carle, J. Charton, E. Cascone, R. Claudi, A. Costille, A. Deboulbe, V. De Caprio, K. Dohlen, D. Fantinel, P. Feautrier, T. Fusco, P. Gigan, E. Giro, D. Gisler, L. Gluck, N. Hubin, E. Hugot, M. Jaquet, M. Kasper, F. Madec, Y. Magnard, P. Martinez, D. Maurel, D. Le Mignant, O. Möller-Nilsson, M. Llored, T. Moulin, A. Origné, A. Pavlov, D. Perret, C. Petit, J. Pragt, J. Szulagyi, and F. Wildi. Post-conjunction detection of β Pictoris b with VLT/SPHERE. *Astronomy and Astrophysics*, 621(34302):1–8, 2019. ISSN 14320746. doi: 10.1051/0004-6361/201834302.

Baptiste Lavie, João M Mendonça, Christoph Mordasini, Matej Malik, and Mickaël Bonnefoy. HELIOS – RETRIEVAL : An Open-source , Nested Sampling Atmospheric Retrieval Code ; Application to the HR 8799 Exoplanets and Inferred Constraints for Planet Formation. *The Astronomical Journal*, 154(3):91, 2017. ISSN 1538-3881. doi: 10.3847/1538-3881/aa7ed8. URL http://dx.doi.org/10.3847/1538-3881/aa7ed8.

Michael C. Liu, Eugene A. Magnier, Niall R. Deacon, Katelyn N. Allers, Trent J. Dupuy, Michael C. Kotson, Kimberly M. Aller, W. S. Burgett, K. C. Chambers, P. W. Draper, K. W. Hodapp, R. Jedicke, N. Kaiser, R. P. Kudritzki, N. Metcalfe, J. S. Morgan, P. A. Price, J. L. Tonry, and R. J. Wainscoat. The extremely red, young L dwarf PSO J318.5338-22.8603: A free-floating planetary-mass analog to directly imaged young gas-giant planets. *Astrophysical Journal Letters*, 777(2), 2013. ISSN 20418205. doi: 10.1088/2041-8205/777/2/L20.

K . Lodders. Solar system abundances of the elements . In : Principles and Perspectives in Cosmochemistry . Lecture Notes of the Kodai School on ' Synthesis of Elements in Stars ' held at Kodaikanal Observatory , India , April 29 - May 13 , 2008 (Aruna Go. *Astrophysics and Space Science*, 2008:379–417, 2010.

N. Lodieu, P. D. Dobbie, and N. C. Hambly. Multi-fibre optical spectroscopy of low-mass stars and brown dwarfs in Upper Scorpius. *Astronomy and Astrophysics*, 527(3):1–19, 2011. ISSN 00046361. doi: 10.1051/0004-6361/201014992.

Patrick J. Lowrance, Glenn Schneider, J. Davy Kirkpatrick, E. E. Becklin, Alycia J. Weinberger, B. Zuckerman, Phil Plait, Eliot M. Malmuth, Sara R. Heap, A. Schultz, Bradford A. Smith, Richard J. Terrile, and Dean C. Hines. A Candidate Substellar

Companion to HR 7329. *The Astrophysical Journal*, 541(1):390–395, 2000. ISSN 0004-637X. doi: 10.1086/309437.

K. L. Luhman and E. E. Mamajek. Spectroscopy of putative brown dwarfs in Taurus. *Astrophysical Journal Letters*, 716(2 PART 2), 2010. ISSN 20418213. doi: 10.1088/2041-8205/716/2/L120.

Kevin L. Luhman. The formation and early evolution of low-mass stars and brown dwarfs. *Annual Review of Astronomy and Astrophysics*, 50:65–106, 2012. ISSN 00664146. doi: 10.1146/annurev-astro-081811-125528.

Bruce Macintosh, James Graham, David Palmer, Rene Doyon, Don Gavel, James Larkin, Ben Oppenheimer, Leslie Saddlemyer, James Wallace, Brian Bauman, Julia Evans, Darren Erikson, Katie Morzinski, Donald Phillion, Lisa Poyneer, Anand Sivaramakrishnan, Rémi Soummer, Simon Thibault, and Jean-Pierre Veran. *The Gemini Planet Imager*, volume 6272. 7 2006. doi: 10.1117/12.672430.

Nikku Madhusudhan. C/O ratio as a dimension for characterizing exoplanetary atmospheres. *Astrophysical Journal*, 758(1), 2012. ISSN 15384357. doi: 10.1088/0004-637X/758/1/36.

Nikku Madhusudhan. Atmospheric Retrieval of Exoplanets. In Hans J Deeg and Juan Antonio Belmonte, editors, *Handbook of Exoplanets*, page 104. 2018. doi: 10.1007/978-3-319-55333-7{\textbackslash}{_}104.

Nikku Madhusudhan. Exoplanetary Atmospheres: Key Insights, Challenges, and Prospects. *Annual Review of Astronomy and Astrophysics*, 57:617–663, 2019. ISSN 00664146. doi: 10.1146/annurev-astro-081817-051846.

Nikku Madhusudhan, Olivier Mousis, Torrence V. Johnson, and Jonathan I. Lunine. Carbon-rich giant planets: Atmospheric chemistry, thermal inversions, spectra, and formation conditions. *Astrophysical Journal*, 743(2), 2011. ISSN 15384357. doi: 10.1088/0004-637X/743/2/191.

Nikku Madhusudhan, Dániel Apai, and Siddharth Gandhi. Atmospheric Compositions of Three Brown Dwarfs and Implications for their Formation Conditions. 2016. URL http://arxiv.org/abs/1612.03174.

A. L. Maire, M. Bonnefoy, C. Ginski, A. Vigan, S. Messina, D. Mesa, R. Galicher, R. Gratton, S. Desidera, T. G. Kopytova, M. Millward, C. Thalmann, R. U. Claudi, D. Ehrenreich, A. Zurlo, G. Chauvin, J. Antichi, A. Baruffolo, A. Bazzon, J. L. Beuzit, P. Blanchard, A. Boccaletti, J. De Boer, M. Carle, E. Cascone, A. Costille, V. De Caprio, A. Delboulbe, K. Dohlen, C. Dominik, M. Feldt, T. Fusco, J. H. Girard, E. Giro, D. Gisler, L. Gluck, C. Gry, T. Henning, N. Hubin, E. Hugot, M. Jaquet, M. Kasper, A. M. Lagrange, M. Langlois, D. Le Mignant, M. Llored, F. Madec, P. Martinez, D. Mawet, J. Milli, O. Moller-Nilsson, D. Mouillet, T. Moulin, C. Moutou, A. Origne, A. Pavlov, C. Petit, J. Pragt, P. Puget, J. Ramos, S. Rochat, R. Roelfsema, B. Salasnich, J. F. Sauvage, H. M. Schmid, M. Turatto, S. Udry, F. Vakili, Z. Wahhaj, L. Weber, and F. Wildi. First light of the VLT planet finder SPHERE: II. the physical properties and the architecture of the young systems PZ Telescopii and HD 1160 revisited. *Astronomy and Astrophysics*, 587: 1–25, 2016. ISSN 14320746. doi: 10.1051/0004-6361/201526594.

A L. Maire, L Rodet, C Lazzoni, A Boccaletti, W Brandner, R Galicher, F Cantalloube, D Mesa, H Klahr, H Beust, G Chauvin, S Desidera, M Janson, M Keppler, J Olofsson, J C. Augereau, S Daemgen, T Henning, P Thébault, M Bonnefoy, M Feldt, R Gratton, A M. Lagrange, M Langlois, M. R. Meyer, A Vigan, V D'Orazi, J Hagelberg, H Le Coroller, R Ligi, D Rouan, M Samland, T Schmidt, S Udry, A Zurlo, L Abe, M Carle, A Delboulbé, P Feautrier, Y Magnard, D Maurel, T Moulin, A Pavlov, D Perret, C Petit, J. R. Ramos, F Rigal, A Roux, and L Weber. VLT/SPHERE astrometric confirmation and orbital analysis of the brown dwarf companion HR 2562 B. \aap, 615:A177, 7 2018. doi: 10.1051/0004-6361/201732476.

Gabriel Dominique Marleau, Gavin A.L. Coleman, Adrien Leleu, and Christoph Mordasini. Exploring the formation by core accretion and the luminosity evolution of directly imaged planets: The case of HIP 65426 b. *Astronomy and Astrophysics*, 624:1–17, 2019. ISSN 14320746. doi: 10.1051/0004-6361/201833597.

Mark S Marley, Jonathan J Fortney, Olenka Hubickyj, Peter Bodenheimer, and Jack J Lissauer. On the Luminosity of Young Jupiters. *The Astrophysical Journal*, 655(1):541–549, 1 2007. doi: 10.1086/509759. URL https://doi.org/10.1086/509759.

Christian Marois, B. Zuckerman, Quinn M. Konopacky, Bruce Macintosh, and Travis Barman. Images of a fourth planet orbiting HR 8799. *Nature*, 468(7327):1080–1083, 2010. ISSN 00280836. doi: 10.1038/nature09684.

Raquel A. Martinez and Adam L. Kraus. A Mid-Infrared Study of Directly-Imaged Planetary-Mass Companions using Archival Spitzer/IRAC Images. 2021. URL http://arxiv.org/abs/2111.03087.

James M. Miley, Olja Panić, Richard A. Booth, John D. Ilee, Shigeru Ida, and Masanobu Kunitomo. The impact of pre-main sequence stellar evolution on mid-plane snowline locations and C/O in planet forming discs. *Monthly Notices of the Royal Astronomical Society*, 500(4):4658–4670, 2021. ISSN 13652966. doi: 10.1093/mnras/staa3517.

P. Molliere and I. A.G. Snellen. Detecting isotopologues in exoplanet atmospheres using ground-based high-dispersion spectroscopy. *Astronomy and Astrophysics*, 622, 2019. ISSN 14320746. doi: 10.1051/0004-6361/201834169.

C. Mordasini, R. van Boekel, P. Mollière, Th. Henning, and Björn Benneke. the Imprint of Exoplanet Formation History on Observable Present-Day Spectra of Hot Jupiters. *The Astrophysical Journal*, 832(1):41, 2016. ISSN 1538-4357. doi: 10.3847/0004-637x/832/1/41.

Sergei Nayakshin. Formation of planets by tidal downsizing of giant planet embryos. *Monthly Notices of the Royal Astronomical Society: Letters*, 408(1):L36–L40, 2010. ISSN 1745-3925. doi: 10.1111/j.1745-3933.2010.00923.x. URL https://doi.org/10.1111/j.1745-3933.2010.00923.x.

Sergei Nayakshin. Dawes Review 7: The Tidal Downsizing Hypothesis of Planet Formation. *Publications of the Astronomical Society of Australia*, 34, 2017. ISSN 14486083. doi: 10.1017/pasa.2016.55.

Gravity Collaboration M Nowak, S Lacour, P Mollière, J Wang, B Charnay, A Buron, F Cantalloube, C Collin, F Chapron, Y Clénet, V Coudé Foresto, P T De Zeeuw, R Dembet, F Gao, E Gendron, R Genzel, S Gillessen, F Haußmann, T Henning, S Hippler, Z Hubert, and L Jocou. Astrophysics Peering into the formation history of β Pictoris b with VLTI / GRAVITY long-baseline interferometry. 110:1–19, 2020.

Karin I. Öberg and Robin Wordsworth. Jupiter's composition suggests its core assembled exterior to the n2 snowline. *arXiv*, 2019. ISSN 23318422. doi: 10.3847/1538-3881/ab46a8.

Karin I. Öberg, Ruth Murray-Clay, and Edwin A. Bergin. The effects of snowlines on C/O in planetary atmospheres. *Astrophysical Journal Letters*, 743(1), 2011. ISSN 20418205. doi: 10.1088/2041-8205/743/1/L16.

Sijme Jan Paardekooper and Anders Johansen. Giant Planet Formation and Migration. *Space Science Reviews*, 214(1), 2018. ISSN 15729672. doi: 10.1007/s11214-018-0472-y. URL http://dx.doi.org/10.1007/s11214-018-0472-y.

Paolo Padoan and AAke Nordlund. The mysterious origin of brown dwarfs. *Astrophys. J.*, 617:559–564, 2004. doi: 10.1086/345413.

J. Patience, R. R. King, R. J. De Rosa, A. Vigan, S. Witte, E. Rice, Ch Helling, and P. Hauschildt. Spectroscopy across the brown dwarf/planetary mass boundary: I. Near-infrared JHK spectra. *Astronomy and Astrophysics*, 540(2011):1–15, 2012. ISSN 00046361. doi: 10.1051/0004-6361/201118058.

Alexey Pavlov, Ole Möller-Nilsson, Markus Feldt, Thomas Henning, Jean-Luc Beuzit, and David Mouillet. SPHERE data reduction and handling system: overview, project status, and development. *Advanced Software and Control for Astronomy II*, 7019(May 2014): 701939, 2008. ISSN 0277786X. doi: 10.1117/12.789110.

S. Petrus, M. Bonnefoy, G. Chauvin, C. Babusiaux, P. Delorme, A. M. Lagrange, N. Florent, A. Bayo, M. Janson, B. Biller, E. Manjavacas, G. D. Marleau, and T. Kopytova. A new take on the low-mass brown dwarf companions on wide-orbits in Upper-Scorpius? *arXiv*, 2019. ISSN 23318422. doi: 10.1051/0004-6361/201935732.

S. Petrus, M. Bonnefoy, G. Chauvin, B. Charnay, G. D. Marleau, R. Gratton, A. M. Lagrange, J. Rameau, C. Mordasini, M. Nowak, P. Delorme, A. Boccaletti, A. Carlotti, M. Houllé, A. Vigan, F. Allard, S. Desidera, V. D'Orazi, H. J. Hoeijmakers, A. Wyttenbach, and B. Lavie. Medium-resolution spectrum of the exoplanet HIP 65426 b. *Astronomy and Astrophysics*, 648:1–21, 2021. ISSN 14320746. doi: 10.1051/0004-6361/202038914.

James B Pollack, Olenka Hubickyj, Peter Bodenheimer, Jack J Lissauer, Morris Podolak, and Yuval Greenzweig. Formation of the Giant Planets by Concurrent Accretion of Solids and Gas. \icarus, 124(1):62–85, 11 1996. doi: 10.1006/icar.1996.0190.

Sascha P. Quanz, Bertrand Goldman, Thomas Henning, Wolfgang Brandner, Adam Burrows, and Lorne W. Hofstetter. Search for very low-mass brown dwarfs and free-floating planetary-mass objects in taurus. *Astrophysical Journal*, 708(1):770–784, 2010. ISSN 15384357. doi: 10.1088/0004-637X/708/1/770.

Roman R Rafikov. Atmospheres of Protoplanetary Cores: Critical Mass for Nucleated Instability. \apj, 648(1):666–682, 9 2006. doi: 10.1086/505695.

A. S. Rajpurohit, F. Allard, S. Rajpurohit, R. Sharma, G. D.C. Teixeira, O. Mousis, and R. Kamlesh. Exploring the stellar properties of M dwarfs with high-resolution spectroscopy from the optical to the near-infrared. *Astronomy and Astrophysics*, 620(1996):1–9, 2018. ISSN 14320746. doi: 10.1051/0004-6361/201833500.

J. Rameau, G. Chauvin, A. M. Lagrange, T. Meshkat, A. Boccaletti, S. P. Quanz, T. Currie, D. Mawet, J. H. Girard, M. Bonnefoy, and M. Kenworthy. Confirmation of the planet around HD 95086 by direct imaging. 2013. doi: 10.1088/2041-8205/779/2/L26. URL `http://arxiv.org/abs/1310.7483%0Ahttp://dx.doi.org/10.1088/2041-8205/779/2/L26`.

Aaron David Schneider and Bertram Bitsch. How drifting and evaporating pebbles shape giant planets I: Heavy element content and atmospheric C/O. (2016), 2021. URL `http://arxiv.org/abs/2105.13267`.

Henriette Schwarz, Christian Ginski, Remco J. de Kok, Ignas A. G. Snellen, Matteo Brogi, and Jayne L. Birkby. The slow spin of the young substellar companion GQ Lupi b and its orbital configuration. *A\&A*, 593:A74, 2016a. doi: 10.1051/0004-6361/201628908. URL `https://doi.org/10.1051/0004-6361/201628908`.

Henriette Schwarz, Christian Ginski, Remco J. De Kok, Ignas A.G. Snellen, Matteo Brogi, and Jayne L. Birkby. The slow spin of the young substellar companion GQ Lupi b and its orbital configuration. *Astronomy and Astrophysics*, 593:1–11, 2016b. ISSN 14320746. doi: 10.1051/0004-6361/201628908.

John Skilling. Skilling, J.: Nested sampling for general Bayesian computation. Bayesian Anal. 1(4), 833-860. *Bayesian Analysis*, 1:833–860, 12 2006. doi: 10.1214/06-BA127.

Ignas Snellen, Bernhard Brandl, Remco de Kok, Matteo Brogi, Jayne Birkby, and Henriette Schwarz. The fast spin-rotation of a young extrasolar planet. *Nature*, 509(7498):63–65, 2014. ISSN 0028-0836, 1476-4687. doi: 10.1038/nature13253. URL `http://arxiv.org/abs/1404.7506%5Cnhttp://www.arxiv.org/pdf/1404.7506.pdf`.

C Soubiran, T Cantat-Gaudin, M Romero-Gómez, L Casamiquela, C Jordi, A Vallenari, T Antoja, L Balaguer-Núñez, D Bossini, A Bragaglia, R Carrera, A Castro-Ginard, F Figueras, U Heiter, D Katz, A Krone-Martins, J F. Le Campion, A Moitinho, and R Sordo. Open cluster kinematics with Gaia DR2. \aap, 619:A155, 11 2018. doi: 10.1051/0004-6361/201834020.

T. Stolker, S. P. Quanz, K. O. Todorov, J. Kühn, P. Mollière, M. R. Meyer, T. Currie, S. Daemgen, and B. Lavie. MIRACLES: Atmospheric characterization of directly imaged planets and substellar companions at 4-5 μ m: I. Photometric analysis of β Pic b, HIP 65426 b, PZ Tel B, and HD 206893 B. *Astronomy and Astrophysics*, 635:1–25, 2020. ISSN 14320746. doi: 10.1051/0004-6361/201937159.

Jordan M. Stone, Josh Eisner, Andy Skemer, Katie M. Morzinski, Laird Close, Jared Males, Timothy J. Rodigas, Phil Hinz, and Alfio Puglisi. L-BAND SPECTROSCOPY WITH MAGELLAN-AO/Clio2: FIRST RESULTS ON YOUNG LOW-MASS COMPANIONS.

The Astrophysical Journal, 829(1):39, 2016. ISSN 1538-4357. doi: 10.3847/0004-637x/829/1/39.

C. Swastik, Ravinder K. Banyal, Mayank Narang, P. Manoj, T. Sivarani, Bacham E. Reddy, and S. P. Rajaguru. Host Star Metallicity of Directly Imaged Wide-orbit Planets: Implications for Planet Formation. *The Astronomical Journal*, 161(3):114, 2021. ISSN 0004-6256. doi: 10.3847/1538-3881/abd802.

L. Testi, T. Birnstiel, L. Ricci, S. Andrews, J. Blum, J. Carpenter, C. Dominik, A. Isella, A. Natta, J. P. Williams, and D. J. Wilner. Dust Evolution in Protoplanetary Disks. *Protostars and Planets VI*, 2014. doi: 10.2458/azu{_}uapress{_}9780816531240-ch015.

A Toomre. On the gravitational stability of a disk of stars. \apj, 139:1217–1238, 5 1964. doi: 10.1086/147861.

Roberto Trotta. Bayes in the sky: Bayesian inference and model selection in cosmology. *Contemporary Physics*, 49(2):71–104, 3 2008. doi: 10.1080/00107510802066753.

A Vigan, C Moutou, M Langlois, F Allard, A Boccaletti, M Carbillet, D Mouillet, and I Smith. Photometric characterization of exoplanets using angular and spectral differential imaging. *Monthly Notices of the Royal Astronomical Society*, 407(1):71–82, 2010. ISSN 0035-8711. doi: 10.1111/j.1365-2966.2010.16916.x. URL https://doi.org/10.1111/j.1365-2966.2010.16916.x.

Zahed Wahhaj, Michael C. Liu, Beth A. Biller, Fraser Clarke, Eric L. Nielsen, Laird M. Close, Thomasl Hayward, Eric E. Mamajek, Michael Cushing, Trent Dupuy, Matthias Tecza, Niranjan Thatte, Mark Chun, Christ Ftaclas, Markus Hartung, I. Neill Reid, Evgenya L. Shkolnik, Silvia H.P. Alencar, Pawel Artymowicz, Alan Boss, Elisabethe De Gouveia Dal Pino, Jane Gregorio-Hetem, Shigeru Ida, Marc Kuchner, Douglas N.C. Lin, and Douglas W. Toomey. The gemini nici planet-finding campaign: Discovery of a substellar L dwarf companion to the nearby young M dwarf CD-35 2722. *Astrophysical Journal*, 729(2), 2011. ISSN 15384357. doi: 10.1088/0004-637X/729/2/139.

J. J. Wang, A. Vigan, S. Lacour, M. Nowak, T. Stolker, R. J. De Rosa, S. Ginzburg, P. Gao, R. Abuter, A. Amorim, R. Asensio-Torres, M. Bauböck, M. Benisty, J. P. Berger, H. Beust, J.-L. Beuzit, S. Blunt, A. Boccaletti, A. Bohn, M. Bonnefoy, H. Bonnet, W. Brandner, F. Cantalloube, P. Caselli, B. Charnay, G. Chauvin, E. Choquet, V. Christiaens, Y. Clénet, V. Coudé du Foresto, A. Cridland, P. T. de Zeeuw, R. Dembet, J. Dexter, A. Drescher, G. Duvert, A. Eckart, F. Eisenhauer, S. Facchini, F. Gao, P. Garcia, R. Garcia Lopez, T. Gardner, E. Gendron, R. Genzel, S. Gillessen, J. Girard, X. Haubois, G. Heißel, T. Henning, S. Hinkley, S. Hippler, M. Horrobin, M. Houllé, Z. Hubert, A. Jiménez-Rosales, L. Jocou, J. Kammerer, M. Keppler, P. Kervella, M. Meyer, L. Kreidberg, A.-M. Lagrange, V. Lapeyrère, J.-B. Le Bouquin, P. Léna, D. Lutz, A.-L. Maire, F. Ménard, A. Mérand, P. Mollière, J. D. Monnier, D. Mouillet, A. Müller, E. Nasedkin, T. Ott, G. P. P. L. Otten, C. Paladini, T. Paumard, K. Perraut, G. Perrin, O. Pfuhl, L. Pueyo, J. Rameau, L. Rodet, G. Rodríguez-Coira, G. Rousset, S. Scheithauer, J. Shangguan, T. Shimizu, J. Stadler, O. Straub, C. Straubmeier, E. Sturm, L. J. Tacconi, E. F. van Dishoeck, F. Vincent, S. D. von Fellenberg, K. Ward-Duong, F. Widmann, E. Wieprecht, E. Wiezorrek, and J. Woillez. Constraining the Nature of the PDS 70 Protoplanets with

VLTI/GRAVITY - . *The Astronomical Journal*, 161(3):148, 2021. ISSN 0004-6256. doi: 10.3847/1538-3881/abdb2d.

M. Wenger, F. Ochsenbein, D. Egret, P. Dubois, F. Bonnarel, S. Borde, F. Genova, G. Jasniewicz, S. Laloë, S. Lesteven, and R. Monier. The SIMBAD astronomical database. *Astronomy and Astrophysics Supplement Series*, 143(1):9–22, 2000. ISSN 0365-0138. doi: 10.1051/aas:2000332.

Kielan K. Wilcomb, Quinn M. Konopacky, Travis S. Barman, Christopher A. Theissen, Jean Baptiste Ruffio, Laci Brock, Bruce Macintosh, and Christian Marois. Moderate-resolution K-band spectroscopy of substellar companion κ andromedae b. *arXiv*, pages 1–23, 2020. ISSN 23318422. doi: 10.3847/1538-3881/abb9b1.

S Witte, Ch. Helling, and P. H. Hauschildt. Dust in brown dwarfs and extra-solar planets. II. Cloud formation for cosmologically evolving abundances. *aap*, 506(3):1367–1380, 11 2009. doi: 10.1051/0004-6361/200811501.

S Witte, Ch. Helling, T Barman, N Heidrich, and P. H. Hauschildt. Dust in brown dwarfs and extra-solar planets. III. Testing synthetic spectra on observations. *aap*, 529:A44, 5 2011. doi: 10.1051/0004-6361/201014105.

Ya-Lin Wu, Brendan P. Bowler, Patrick D. Sheehan, Sean M. Andrews, Gregory J. Herczeg, Adam L. Kraus, Luca Ricci, David J. Wilner, and Zhaohuan Zhu. ALMA 0.88 mm Survey of Disks around Planetary-mass Companions. *The Astronomical Journal*, 159(5):229, 2020. ISSN 1538-3881. doi: 10.3847/1538-3881/ab818c.

Yapeng Zhang and Ignas A G Snellen. Possibly distinct formation pathways of super-Jupiters and brown dwarfs. (Drake 2005), 2021.

Yapeng Zhang, Ignas A. G. Snellen, Alexander J. Bohn, Paul Mollière, Christian Ginski, H. Jens Hoeijmakers, Matthew A. Kenworthy, Eric E. Mamajek, Tiffany Meshkat, Maddalena Reggiani, and Frans Snik. The 13CO-rich atmosphere of a young accreting super-Jupiter. *Nature*, 595(7867):370–372, 2021. ISSN 0028-0836. doi: 10.1038/s41586-021-03616-x.

Appendix A

SINFONI K band Library Spectra

The final extracted spectra for each target can be found in this section. These are the median combined spectra of the good quality observations, corrected for different effects, as described in Chapter 2, and calibrated in flux. All the references for the cited values can be found in the Tables 2.1, 2.2 and specific parameters of the observations on the observation log in Table 2.3.

A.1   2M 0103 AB B
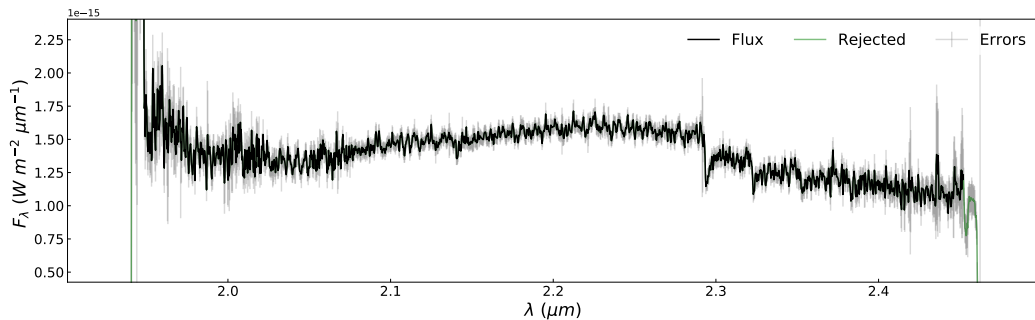
Figure A.1: Spectrum of 2M 0103 AB B

2M 0103 AB B is a companion to a double low-mass stars system, located at $47.2\,pc$ from the sun, member of the Tucana-Horologium association with an estimated age of $30\,Myr$. The binary system is known as SCR J01033563-5515561 too. 2M 0103 AB B is orbiting the system at $84\,au$ in projected separation. This target was observed four nights, eight exposures each time, but only in two nights is the companion observable on the field of view (hereafter FoV). The standard stars observed for the atmospheric transmission spectrum are Hip 008445 (B9V) and Hip 108421 (B9.5V). The source is well defined but close to its host binary for all individuals' observations. Not all the extracted spectra have excellent quality, but we decided to median combine them all, and the outcome is observable in Figure A.1.

A.2   AB Pic b
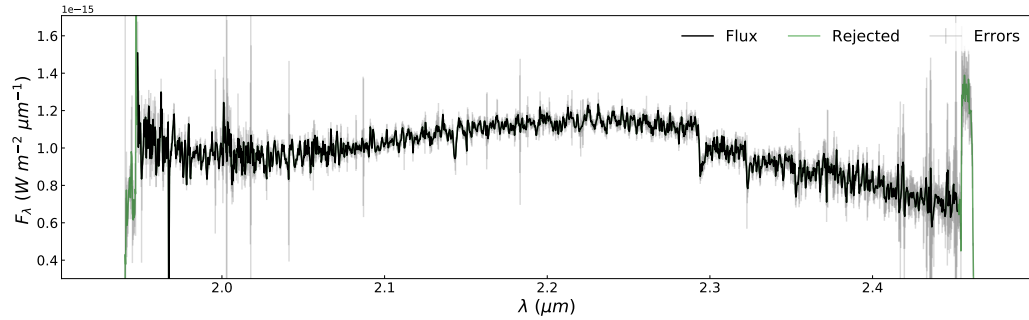
Figure A.2: Spectrum of AB Pic b

AB Pic b is a companion located at $50.14\,pc$, classified as part of the young $(13Myr)$ Carina association. This target is orbiting the host star at a projected separation of $273\,au$, and probably the configuration is edge on to our point of view. AB Pic b has a spectral type around L0 and an effective temperature probably close to $1800\,K$. The target was observed two nights, on 12/01/2014 and 15/12/2013, each with five exposures. The standard stars used to get the atmospheric transmission spectra are Hip 038904 (B8V) and Hip 034397 (B8V). The source is well defined and centered inside the image for all individuals' observations. We used all individual observations to median combine them finally, and this spectrum is observable in Figure A.2 and was used for the atmospheric modeling presented in Chapter 3.

A.3   CAHA TAU 1
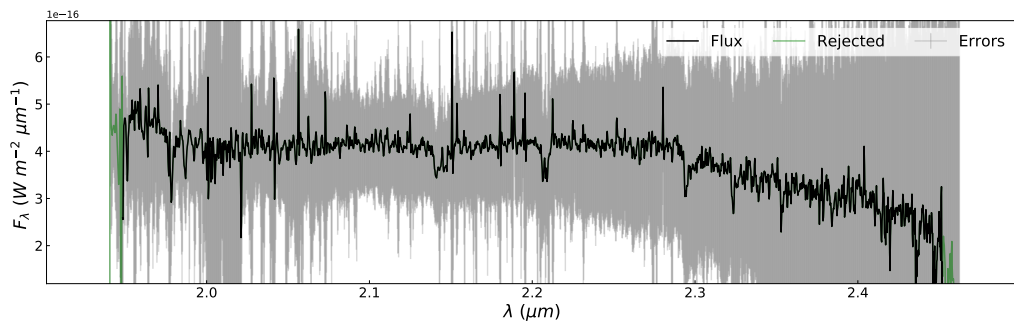
Figure A.3: Spectrum of CAHA TAU 1

CAHA TAU 1 is an isolated target at 140 pc from the sun of spectral type around M6 and effective temperature around 2000. It was observed two times, with three exposures on the first epoch, where the companion is outside the field of view in two of them, and four exposures on the second epoch. The spectra, in general, look very noisy for all the cubes. We ended up with five cubes to extract the spectrum of CAHA TAU 1. The standard stars used are Hip 038280 (B9IV) and Hip 029832 (B9V). We used these five extracted spectra to

median combine them finally, but, as observable in Figure A.3, the resulted spectrum is very noisy.

A.4   CD-35 2722 B
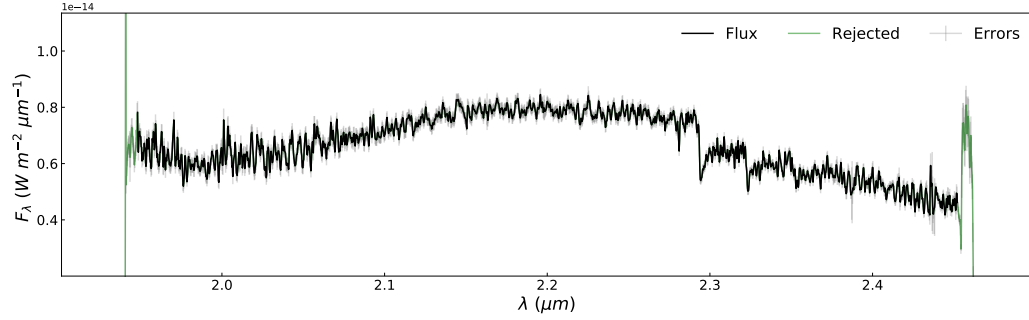
Figure A.4: Spectrum of CD-35 2722 B

CD-35 2722B is a companion member of the AB Doradus association at $21\,pc$ from the sun and an estimated age of $5\,Myr$. Its spectral type is around L0, with an effective temperature around $1800\,K$ and orbiting its host star at a projected separation of $67\,au$. CD-35 2722B was observed one night with four exposures. The standard star observed is Hip 036228, a B9 V spectral type star. For all individuals' observations, the source is very well defined and centered inside the limits of the image. A ray of light seems to be crossing the image, which may contaminate the spectrum, but the intensity is much lower than the companion's light. We used all extracted spectra to median combine them finally, and the final result is observable in Figure A.4.

A.5   DH TAU B
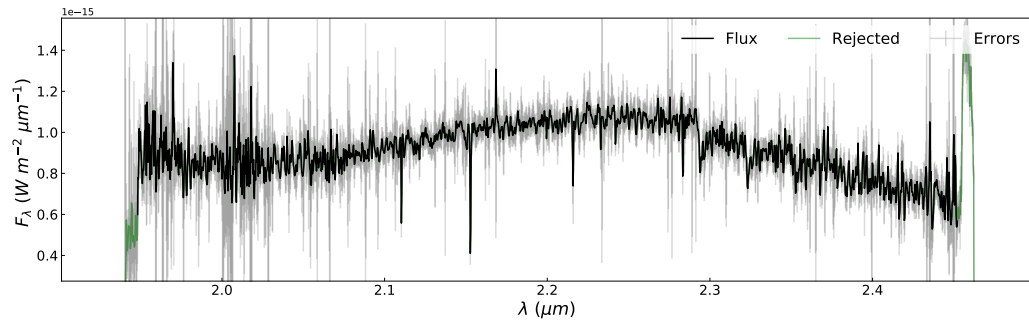
Figure A.5: Spectrum of DH TAU B

DH TAU B is a young $(1\,Myr)$ companion, member of the Taurus association, located at $142\,pc$ from the sun. It has an estimated M9 spectral type and a T_{eff} of $2400\,K$. The

companion is orbiting its M0 host star at a projected distance of $330\,au$ This target was observed three nights, each time with two exposures. The extraction radius used is 5 pixels, but the spectra have a high quality for some cubes, and for others, considerable emission and absorption lines cross the spectra. The standard stars used to get the atmospheric transmission spectrum are Hip 034395 (B2V), Hip 040105 (B5V), and Hip 018296 (B9E). The final medium combined spectrum is noisy. Some contamination light is crossing the image on the horizontal just through the middle of the source, which could be a reason for the noisiness we observe in Figure A.5, but it seems to be an effect of the object itself and not the contamination of another nearby source. We used all extracted spectra to median combine them finally. For correcting the sky emission lines, we fitted a 0-degree polynomial to a masked cube and extracted the sky behavior over the wavelengths.

A.6 FU TAU B
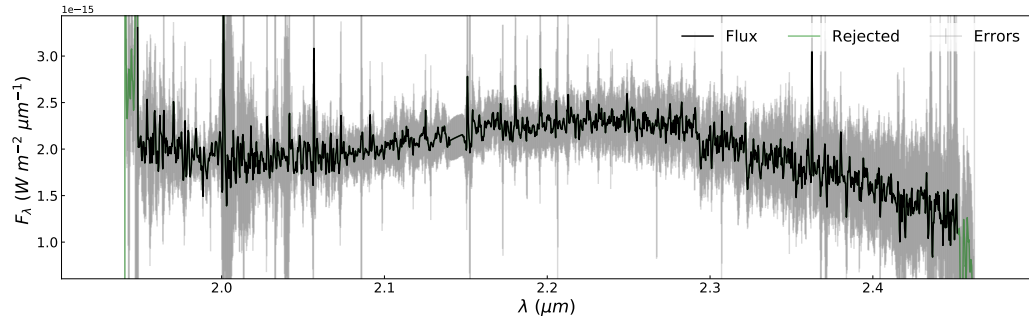
Figure A.6: Spectrum of FU TAU B

FU TAU B is a companion at $140\,pc$ from the sun, a young Taurus association member $(1\,Myr)$. It is orbiting its host star at a projected distance of $800\,au$, and its spectral type is around L0. It was observed during one night with six exposures. The companion is not well centered on each cube. In some of them, the target is half outside the FoV. The standard star used to get the atmospheric transmission spectrum is Hip 029446 (B2V). The presented spectrum in Figure A.6 is the result when median combining the spectra of the cubes where the companion is entirely inside the FoV.

A.7 GSC 06214 B

GSC 06214 B is a companion located at $145\,pc$, and member of the young $(\sim 5\,Myr)$ Upper Scorpios OB association. It has a reported spectral type of L0, and it is orbiting its host star at a projected separation of $320\,au$. For this program, it was observed during one night with four exposures. In all four exposures, the host star is half outside the FoV, and the companion is close to the host. Therefore its light is highly contaminated with deep lines and high peaks. The projected separation between companion and host is $2.2"\,or\,320\,au$ with a $PA = 180\,deg$.
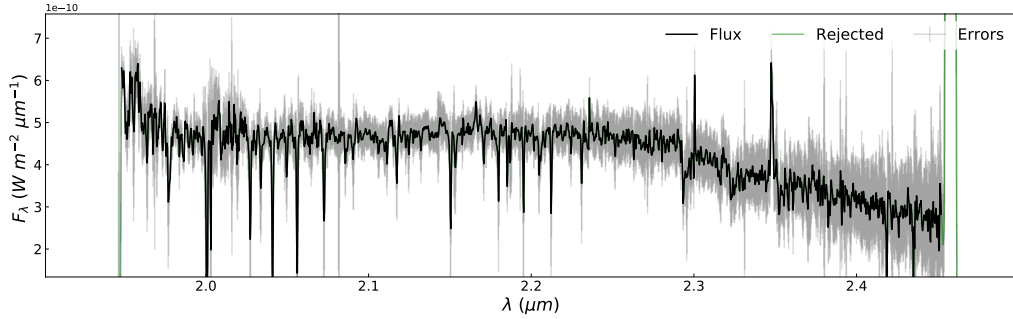
Figure A.7: Spectrum of GSC 06214 B

The standard star used to get the atmospheric transmission spectrum is Hip 082652 (B3III), a problematic spectral type since the program did not recognize it. For this specific target, observable in Figure A.7 the spectrum looks highly contaminated, and even the shape may be affected. We are testing a spectral deconvolution routine to clean the spectrum from the host starlight, but this routine is not ready at the moment and is one of the first things we are planning to finish in the upcoming Ph.D. program.

A.8 HIP 78530 B
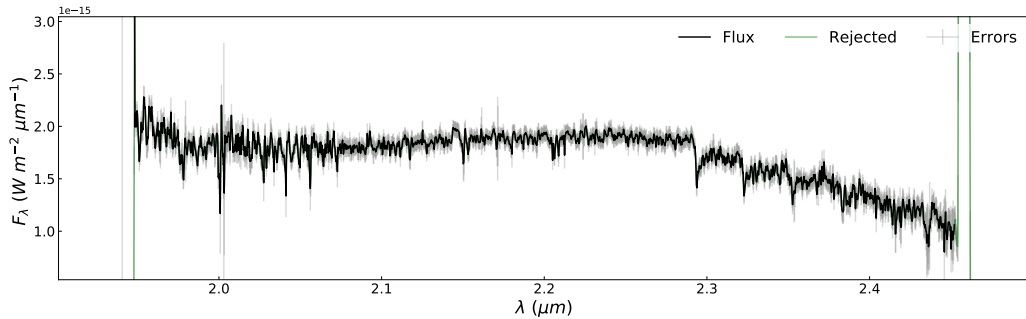
Figure A.8: Spectrum of HIP 78530 B

HIP 78530 B is a companion, member of the Upper Scorpius association at a distance of $137\,pc$ and with an estimated age of $10\,Myr$. The companion is of spectral type M7, and it is orbiting its host star (B9V) at a projected separation of $623\,au$ It was observed during two nights, each time with four exposures. The target is well centered for each observation. The standard star for the first night, used to get the atmospheric transmission spectrum, is Hip 068876 (B9V), and for the second-night Hip 079473 (B9.5V). The second-night observations are much noisier than the first ones. Some lines are crossing the datacubes but not close to the companion's light, which may still affect it. For the sky emission lines subtraction, we used a big inner radius for the mask (30 pixels) to eliminate bright speckles and rays. The best solution would be to get rid of them first and then correct for sky emission lines, but finally, we just ignored the spikes because the final result is good enough. We applied no sky emission lines correction for this final median combined spectrum.

A.9   HR 7329 B
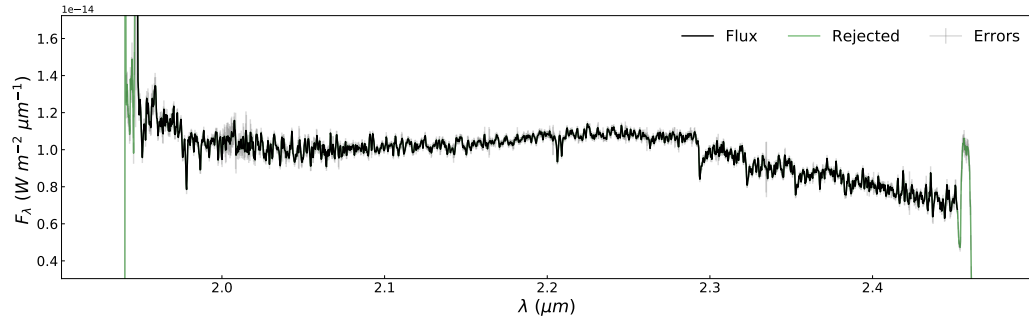
Figure A.9: Spectrum of HR 7329 B

HR 7329 B is a companion at $47.6\,pc$ from the sun, member of the $\beta\,$Pic association with an age of $20\,Myr$. It has an estimated spectral type of M8, and it is orbiting its host star (A0V) at a projected distance of $136\,au$ and 4.2". This companion is identified with the name Eta Tel b too. It was observed during three nights, the first with eight exposures, the second with nine, and the third with two. On the first night observations for some datacubes, the companion does not appear inside the FoV. Apart, some of the exposures are high quality while others are noisy. The standard stars used to get the atmospheric transmission spectra are Hip 090348 (B8.5V) for the first night and Hip 095404 (B8V) for the second and third nights. The non-well centered observations of night one were rejected from the final medium combined spectrum observable in Figure A.9. The quality of the final spectrum is excellent.

A.10   KPNO TAU 1
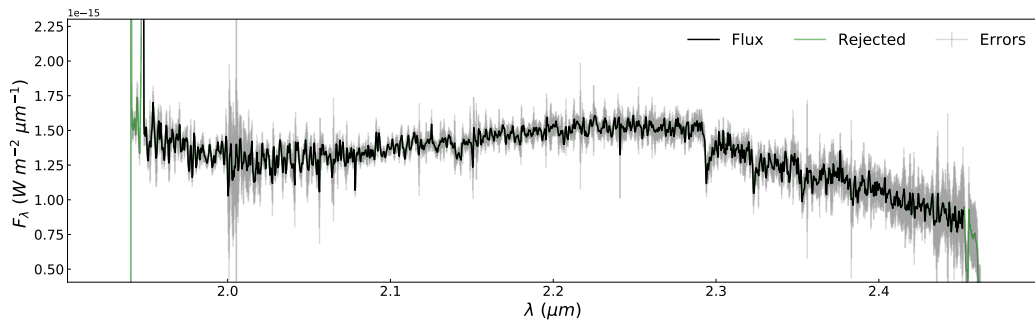
Figure A.10: Spectrum of KPNO TAU 1

KPNO TAU 1 is an isolated BD member of the Taurus association of $\sim 5\,Myr$ at $140\,pc$ from the solar system. It has a reported spectral type of M8.5V. This object was observed during one night with six exposures. The standard star used to get the atmospheric transmission spectrum is Hip 028220 (B5E). On the last exposure, the target is half outside the FoV; therefore, we rejected this datacube. Finally, due to the background noise, we selected the

first three datacubes and median combined their spectra to end up with the final spectrum observable in Figure A.10.

A.11 KPNO TAU 4
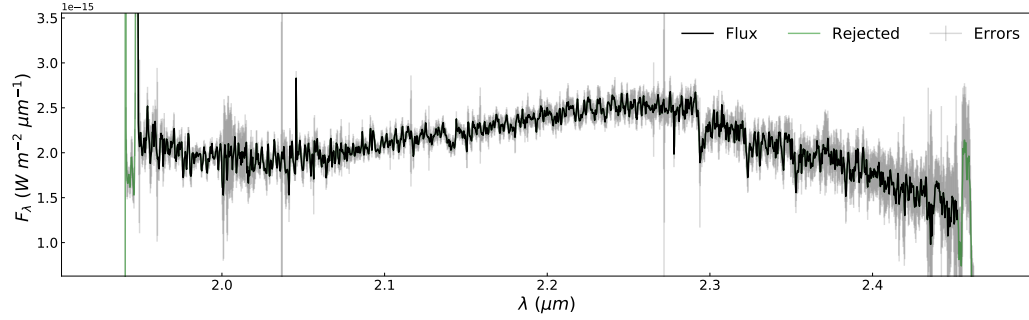
Figure A.11: Spectrum of KPNO TAU 4

KPNO TAU 4 is an isolated BD similar to KPNO TAU 1, member of the same association and at $140\,pc$. It has a spectral type of M9.5. It was observed one night with six exposures. Each spectrum has a relatively good quality, but some minor high and low emission peaks are observable. The standard star used to get the atmospheric transmission spectrum is Hip 027456 (B8E). For all individuals' observations, the source is well defined and centered inside the FoV except for the last one. The sky emission lines correction makes a remarkable improvement for this target. Three of the datacubes were rejected from the final median combined spectrum, observable in Figure ?? for different reasons.

A.12 KPNO TAU 6
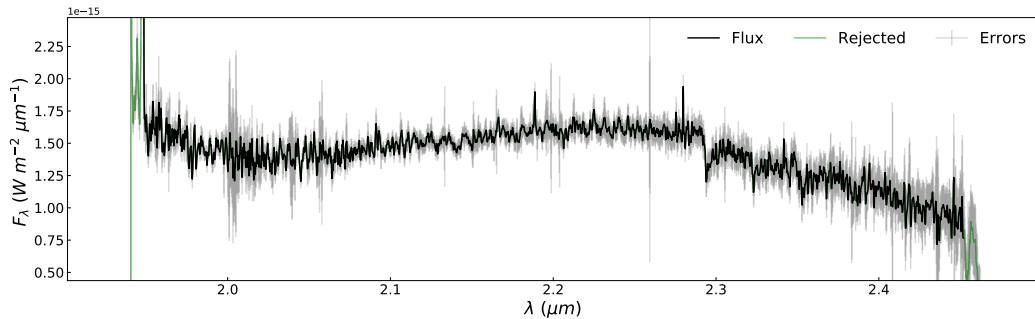
Figure A.12: Spectrum of KPNO TAU 6

KPNO TAU 6 is again very similar to KPNO TAU 1 and 4. It is located a little closer at $116\,pc$, and its spectral type is M8.5V. Again, in the last six exposures, taken during one night, the target is outside the FoV. The standard star used to get the atmospheric

transmission spectrum is Hip 029832 (B9V). We do not have bad spectra but many with random high and low peaks. We used the five first exposures to extract the spectra and finally median combine them, observable in Figure A.12.
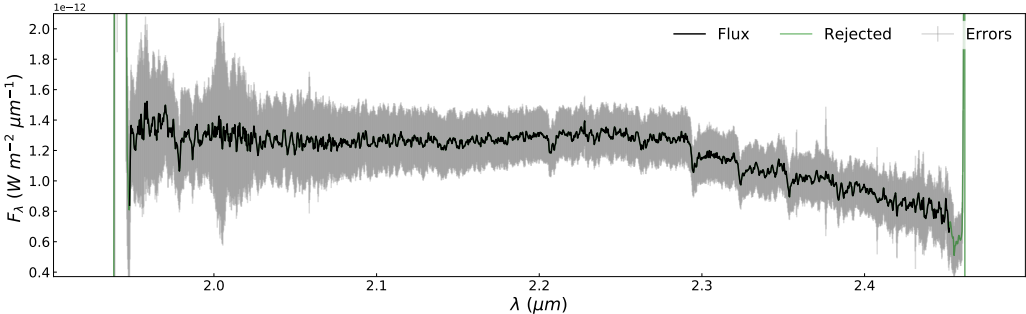
A.13 PZ TEL B

Figure A.13: Spectrum of PZ TEL B

PZ TEL B is a companion, member of the β Pic association, located at $51.5\,pc$ from the solar system and with an estimated age around $12\,Myr$. It has an estimated M7V spectral type, orbiting its host star (G6.5) at $20\,au$. This companion is also known under HD 174429 B and HIP 92680 B. This target was observed two nights, but on the first night, the companion was outside the FoV. On the second night, eight exposures were taken, where the companion is again outside the FoV for the first exposure. The standard star used to get the atmospheric transmission spectrum is HIP094849 (B8V). The host star is very close to the target, and its light contaminates the companion spectra in the form of a halo. We still have to figure out the possible side effects of this contamination. For now, the final median combined spectrum for PZ TEL B is observable in Figure A.13.

A.14 RXS 1609 B
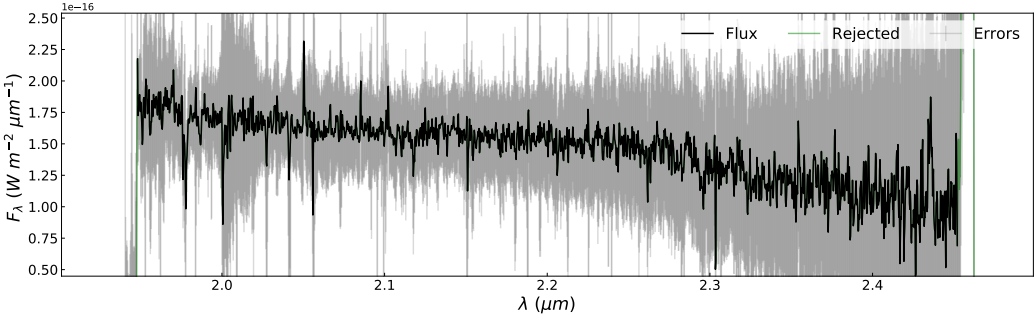
Figure A.14: Spectrum of RXS 1609 B

RXS 1609 B is a companion member of the Upper Scorpios association, located at $139\,pc$ from the solar system. It has an estimated age of $11\,Myr$ and an L0 spectral type. This target is orbiting its M0 host star at a projected separation of $2.22\,"$ or $330\,au$. The current extracted spectrum for this target is observable in Figure A.14, but this cannot be trusted. As for GSC 06214 B, the companion is close to its host star, and therefore its light is contaminated. We are also testing the SD routine, but we still have not successfully extracted the spectrum.

A.15   USCO 1606-2219
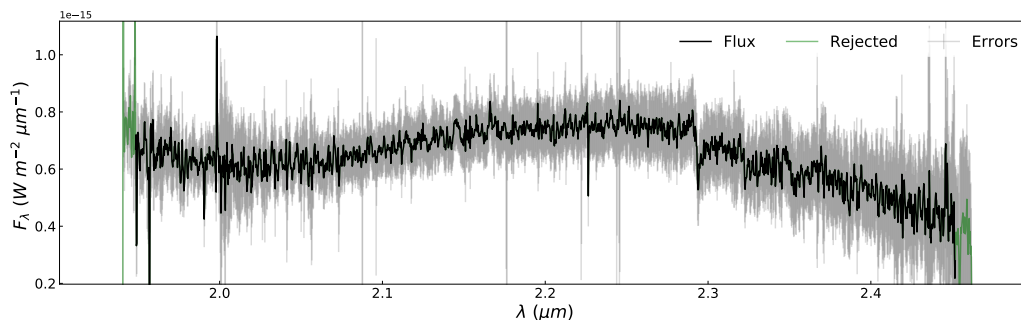
Figure A.15: Spectrum of USCO 1606-2219

The following nine targets, all identified under the USCO nomenclature, are very similar. They all isolated field BD, members of the young $(5-10\,Myr)$ Upper Scorpius association at approximately $145 \pm 15\,pc$ from the sun.

USCO 1606-2219 has an estimated L2 spectral type. It was observed one night with four exposures. The spectra look noisy for all tested extraction radius; therefore, we set the extraction radius to 5 pixels. The standard star used to get the atmospheric transmission spectrum is Hip 086507 (B9V). For all individuals' observations, the source is very well defined and centered inside the limits of the image except for the second, where two objects can be identified on the FoV. It seems that the one on the left upper corner is USCO 1606-2219; however, this datacube was ignored before finally median combine the spectra and end up with the spectrum presented in Figure A.15. The result is highly noisy but does not look too bad.

A.16   USCO 1606-2230

USCO 1606-2230 has an estimated M8 spectral type. It was observed one night with four exposures. The spectra look noisy, but, as argued for USCO 1606-2219, the extraction radius used is 5 pixels. The standard star used to get the atmospheric transmission spectrum is Hip 079042 (B9V). For all individuals' observations, the source is very well defined. The target is on a different corner of the datacube for each exposure but inside the FoV. There are some black spots on the datacubes, but not over the target; therefore, we ignored this detail. We
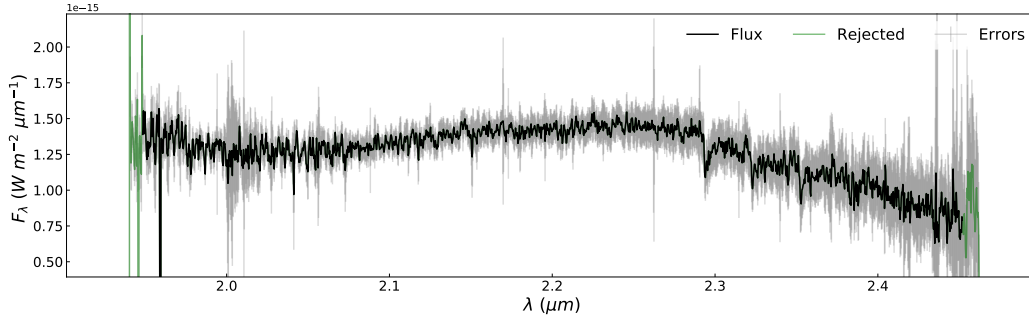
Figure A.16: Spectrum of USCO 1606-2230

used all extracted spectra to median combine them finally, and the final spectrum can be observed in Figure A.16. The result is noisy because of deep absorption lines, but it does not seem too bad, and the sky emission lines correction significantly improves the result.
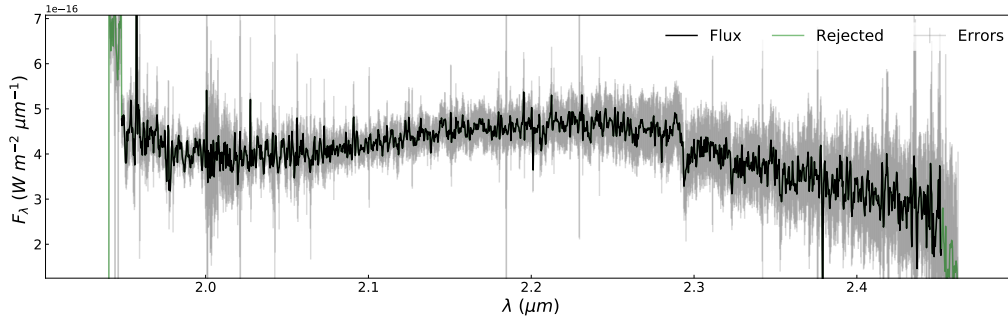
A.17 USCO 1606-2335

Figure A.17: Spectrum of USCO 1606-2335

USCO 1606-2230 has an estimated M9 spectral type. It was observed one night with three exposures. The spectra look noisy, but, as argued for USCO 1606-2219, the extraction radius used is 5 pixels. The standard star used to get the atmospheric transmission spectrum is Hip 084190 (B9V). For all individuals' observations, the source is very well defined. The target is on a different corner of the datacube for each exposure but inside the FoV. We used all extracted spectra to median combine them finally, and the final spectrum can be observed in Figure A.17. The result is noisy because of deep absorption lines, but it does not seem too bad, and the sky emission lines correction significantly improves the outcome.

A.18 USCO 1607-2239

USCO 1607-2239 has an estimated L1 spectral type. It was observed two nights with four exposures on the first one and two on the second one. There may be more profound problems
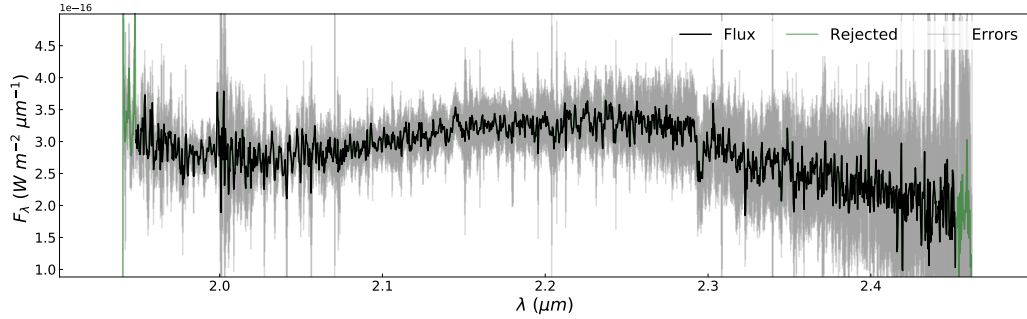
Figure A.18: Spectrum of USCO 1607-2239

for this target than just observational noise since, for different observations on the same night, the slope of the extracted spectrum for each datacube and its main features change. We set the aperture radius to five pixels again. The standard stars used to get the atmospheric transmission spectra are Hip 094122 (B8V) and Hip 079473 (B9.5V). For all individuals' observations, the source is very well defined. The target is on a different corner of the datacube for each exposure but inside the FoV. The slopes of the individual spectra are not consistent, as previously mentioned; therefore, we do not entirely trust the spectrum observable in Figure A.18; however, we will analyze this target in detail during the upcoming Ph.D. program.
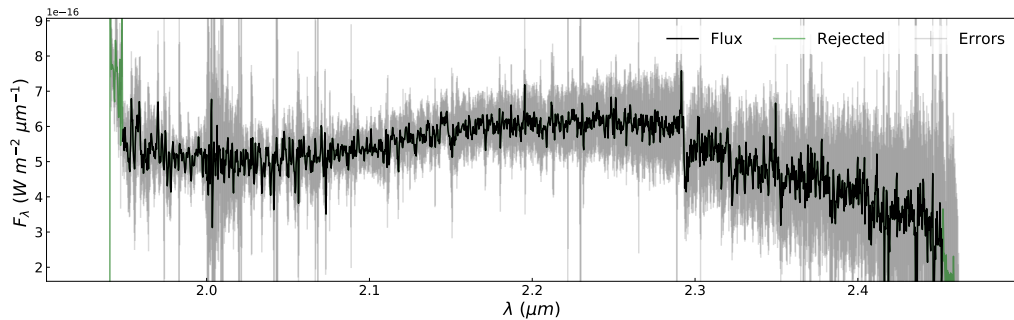
A.19   USCO 1608-2232

Figure A.19: Spectrum of USCO 1608-2232

USCO 1608-2232 has an estimated M9 spectral type. It was observed one night with four exposures. The spectra look noisy, but, as argued for USCO 1606-2219, the extraction radius used is 5 pixels. The standard star used to get the atmospheric transmission spectrum is Hip 079897 (B9V). For all individuals' observations, the source is very well defined. The target is on a different corner of the datacube for each exposure but inside the FoV. We used all extracted spectra to median combine them finally, and the final spectrum can be observed in Figure A.19. The result is noisy because of deep absorption lines. The sky emission lines correction does not significantly improve the result for this particular target. To improve the final extracted spectrum, we decided to ignore the third datacube due to its higher noise.
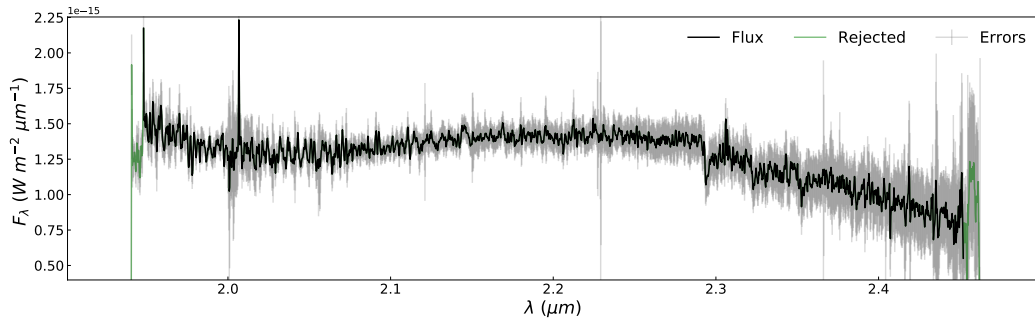
A.20 USCO 1608-2335

Figure A.20: Spectrum of USCO 1608-2335

USCO 1608-2335 has an estimated M8.5 spectral type. It was observed one night with four exposures. The spectra look noisy, but, as argued for USCO 1606-2219, the extraction radius used is 5 pixels. The standard star used to get the atmospheric transmission spectrum is Hip 079739 (B8V). For all individuals' observations, the source is very well defined. The target is on a different corner of the datacube for each exposure but inside the FoV. We used all extracted spectra to median combine them finally, and the final spectrum can be observed in Figure A.20. The result is noisy because of deep absorption lines, but it does not seem too bad, and the sky emission lines correction significantly improves the result.
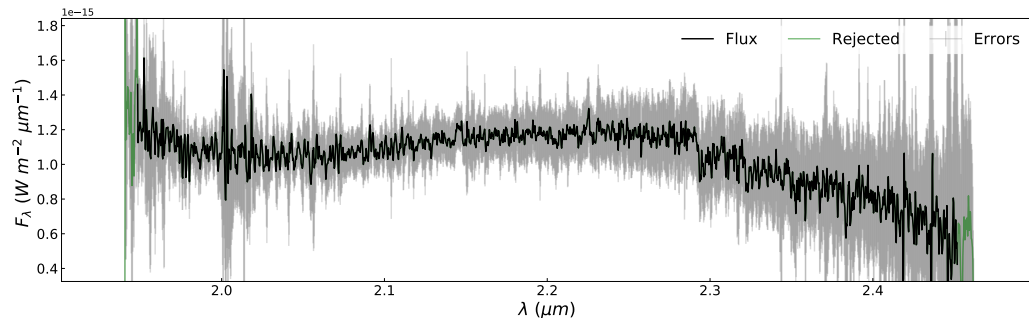
A.21 USCO 1610-2239

Figure A.21: Spectrum of USCO 1610-2239

USCO 1610-2239 has an estimated M8.5 spectral type. It was observed one night with four exposures. The spectra look noisy, but, as argued for USCO 1606-2219, the extraction radius used is 5 pixels. The standard star used to get the atmospheric transmission spectrum is Hip 080804 (B9V). The source is very well defined for all individuals' observations, except on the final exposure, where the target appears very faint. The target is on a different corner of the datacube for each exposure but inside the FoV. We used all extracted spectra to median combine them finally, and the final spectrum can be observed in Figure A.21. The result is noisy because of deep absorption lines, but it does not seem bad. The sky emission lines

correction does not significantly improve the result since it is not higher than the noise level, but we still believe it is essential to perform. By eye, this target has a more precise spectrum than the previously presented USCO members.
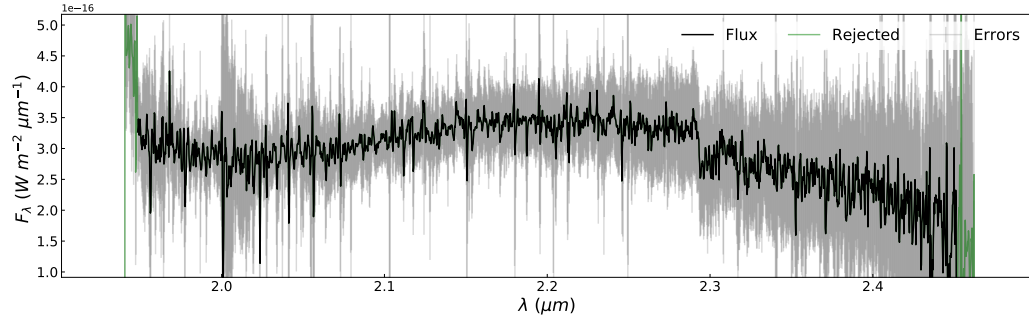
A.22   USCO 1612-2156

Figure A.22: Spectrum of USCO 1612-2156

USCO 1612-2156 has an estimated L0 spectral type. It was observed two nights, with four exposures the first and three exposures the second. The spectra look noisy, but, as argued for USCO 1606-2219, the extraction radius used is 5 pixels. The standard star used to get the atmospheric transmission spectrum is Hip 082154 (B9IV/V). For all individuals' observations, the source is very well defined; however, the second exposure of the second night has a higher noise level. The target is on a different corner of the datacube for each exposure but inside the FoV. We used all extracted spectra to median combine them finally, and the extracted spectrum can be observed in Figure A.22. The result is noisy, but it does not seem too bad, and the sky emission lines correction significantly improved the outcome.
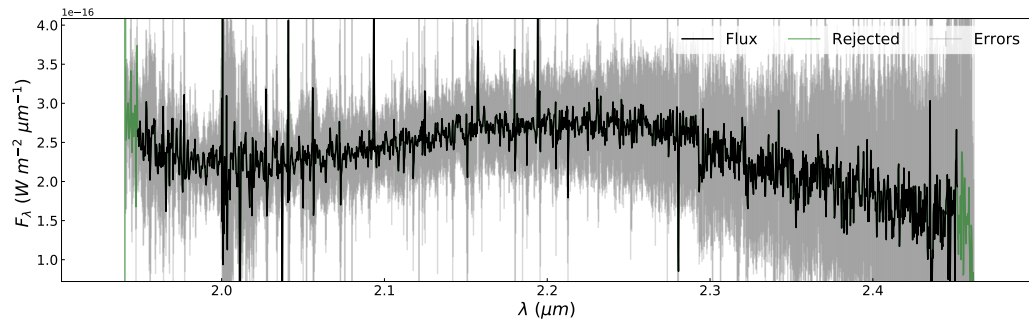
A.23   USCO 1613-2124

Figure A.23: Spectrum of USCO 1613-2124

USCO 1613-2124 has an estimated L0 spectral type. It was observed two nights, with four exposures the first and three exposures the second. In general, this target is very similar

to USco 1613-2124. The spectra look noisy, and the extraction radius used is 5 pixels. The standard star used to get the atmospheric transmission spectrum is Hip 078968 (B8V). For all individuals' observations, the source is very well defined; however, the third exposure of the second night has a higher noise level. The target is on a different corner of the datacube for each exposure but inside the FoV. We used the mentioned spectra to median combine them finally, and the extracted spectrum can be observed in Figure A.23. The result is noisy, but the sky emission lines correction significantly improved the outcome.
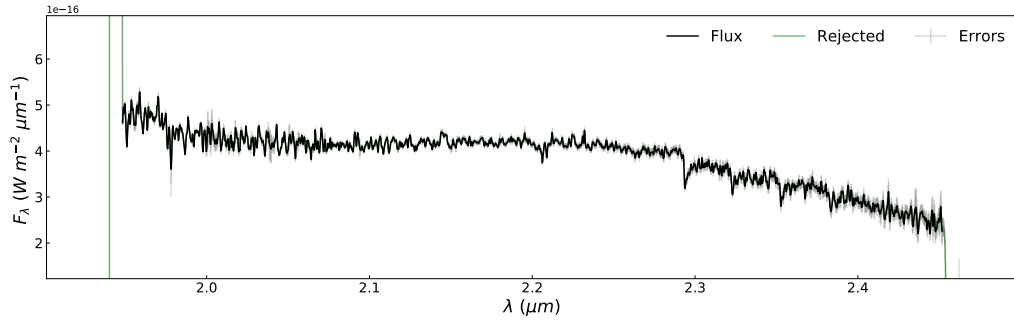
A.24   USCO CTIO 108 AB

Figure A.24: Spectrum of USCO CTIO 108 AB

USCO CTIO 108 AB is the low-mass BD member of a binary system on the Upper Scorpius association at $145 \pm 15\,pc$ from the sun. This binary member is orbiting the higher mass member at a projected distance of 4.6" or $667 \pm 10\,au$. As for the other USCO members, this is a young target ($\sim 5\,Myr$) and has an estimated M7 spectral type. This target was observed during one night with five exposures. On the datacubes, we identified two objects, and after a visual inspection of their coordinates, we recognized that the faintest one was our target. The extraction radius was set to five pixels. The standard star used to get the atmospheric transmission spectrum is Hip 079739 (B8V). Even though the target is faint, the extracted spectrum for each datacube is high quality. We used finally all exposures and median combined them to extract the final spectrum, presented in Figure A.24. The quality of this companion is significantly better, compared to the isolated members of this same association.